RICE UNIVERSITY

Advanced Characterization and Optical Properties of Single-Walled Carbon Nanotubes and Graphene Oxide.

by

Anton Viatcheslavovich Naumov

A THESIS SUBMITTED
IN PARTIAL FULFILLMENT OF THE
REQUIREMENTS FOR THE DEGREE

Doctor of Philosophy

APPROVED, THESIS COMMITTEE:

R. Bruce Weisman

R. Bruce Weisman, Chair, Professor, Department of Chemistry

Pulickel M. Ajayan, Benjamin M. and Mary Greenwood Anderson Professor of Engineering, Department of Mechanical Engineering and Materials Science

Douglas Natelson, Professor, Departments of Physics and Astronomy, and Electrical and Computer Engineering

HOUSTON, TEXAS

MARCH 2011

ABSTRACT

Photophysical, electronic, and compositional properties of single-walled carbon nanotubes (SWCNTs) and bulk nanotube samples were investigated together with graphene oxide photoluminescence. First, we studied the effect of external electric fields on SWCNT photoluminescence. Fields of up to 10^7 V/m caused dramatic, reversible decreases in emission intensity. Quenching efficiency was proportional to the projection of the field on the SWCNT axis, and showed inverse correlation with optical band gap. The magnitude of the effect was experimentally related to exciton binding energy, as consistent with a proposed field-induced exciton dissociation model.

Further, the electronic composition of various SWCNT samples was studied. A new method was developed to measure the fraction of semiconducting nanotubes in as-grown or processed samples. SWCNT number densities were compared in images from near-IR photoluminescence (semiconducting species) and AFM (all species) to compute the semiconducting fraction. The results provide important information about SWCNT sample compositions that can guide controlled growth methods and help calibrate bulk characterization techniques.

The nature of absorption backgrounds in SWCNT samples was also studied. A number of extrinsic perturbations such as extensive ultrasonication, sidewall functionalization, amorphous carbon impurities, and SWCNT aggregation were applied and their background contributions quantified. Spectral congestion backgrounds from overlapping absorption bands were assessed with spectral modeling. Unlike semiconducting nanotubes, metallic SWCNTs gave broad intrinsic absorption

backgrounds. The shape of the metallic background component and its absorptivity coefficient were determined. These results can be used to minimize and evaluate SWCNT absorption backgrounds.

Length dependence of SWCNT optical properties was investigated. Samples were dispersed by ultrasonication or shear processing, and then length-fractionated by gel electrophoresis or controlled ultrasonication shortening. Fractions from both methods showed no significant absorbance variations with SWCNT length. The photoluminescence intensity increased linearly with length, and the relative quantum yield gradually increased, approaching a limiting value.

Finally, a strong pH dependence of graphene oxide photoluminescence was observed. Sharp and structured excitation/emission features resembling the spectra of molecular fluorophores were obtained in basic conditions. Based on the observed pH-dependence and quantum calculations, these spectral features were assigned to quasi-molecular fluorophores formed by the electronic coupling of oxygen-containing addends with nearby graphene carbon atoms.

ACKNOWLEDGEMENTS

My appreciation and acknowledgements go to the following people, whose invaluable contributions and support have led to present work.

Prof. R. Bruce Weisman,

for his supervision, interest, advice and guidance, help regarding many aspects of my professional development, and for serving as a chair of my thesis committee.

Members of the committee, Prof. Douglas Natelson and Prof. Pulickel M. Ajayan

for their candid feedback, for their time and patience spent to read the thesis, and for serving as members of the thesis committee.

Dr. Sergei M. Bachilo and Dr. Dmitri A. Tsyboulski

for being great colleagues and mentors, for offering many ideas, answering numerous questions and helping in a number of experiments in the studies of electric field-induced SWCNT photoluminescence quenching , absorption backgrounds in SWCNT samples and length dependence of SWCNT optical properties

Dr. Avetik Harutyunyan and Dr. Phaedon Avouris

for mentoring my research during the internships at Honda Research Institute and IBM T.J. Watson Research Center.

Groups at Northwestern University, SouthWest Nanotechnologies Inc., Honda Research Institute, IBM T.J. Watson Research Center and NASA Johnson Space Center

for providing SWCNT samples for the analyses of semiconducting fraction.

Prof. Pulickel M. Ajayan, Dr. Aditya Mohite and Charudatta Galande

for incisive mentoring, numerous ideas and discussions, preparing samples for optical measurements, for infrared analysis, data processing and interpretation in the collaborative project on graphene oxide photoluminescence.

Saunab Ghosh

for preparing DGU-sorted SWCNT samples for absorption spectroscopy analysis

Former and current members of the Weisman group: John-David Rocha, John Casey, Tonya Leeuw, Paul Cherukuri, Saunab Ghosh, Griffin Canning and Jason Streit

for their help, criticism, and for being great colleagues to work with

My parents Viatcheslav I. Naumov and Irina Y. Naumova and my friends

for advice, support and encouragement

TABLE OF CONTENTS

LIST OF FIGURES

LIST OF TABLES

CHAPTER 1

Introduction

1.1 General Introduction

Currently a significant part of leading scientific research is conducted in the areas of Bio- and Nanotechnology. A number of recent publications have reported technological and scientific advances in these areas. For example, it has been shown that single-electron transistors can serve as efficient biological sensors[1] for determining the presence of many possible diseases at once, and ZnO nanowires and carbon nanotubes can be used as field emitters for new technology flat panel displays.[2-4] Single and multi-walled carbon nanotubes are often added to epoxy composites to increase their thermal conductivity[5] and mechanical strength.[6-9] At present numerous publications concern the study of novel nanomaterials such as fullerenes,[10] nanowires,[11,12] nanorods,[13] nanoshells,[14] carbon nanotubes[15] and graphene.[16]

1.2 Introduction to Carbon Nanotubes

Fullerenes and carbon nanotubes can be considered as related allotropes of carbon. Their unique properties are determined by molecular structure. A single carbon nanotube can be represented as a graphene sheet rolled up in a cylinder (Fig 1). Since graphene sheet wrapping can happen along various directions, there may be several resulting structures of single-walled carbon nanotubes. Each is defined by the coordinates of its chiral (wrapping) vector. These coordinates, represented by indices n and m, indicate how many lattice vectors a_1 and a_2 of the graphene lattice are needed to construct

a particular chiral vector. For example, as seen from Fig 1.a, to construct the chiral vector of (9,4) carbon nanotube, one would need to add up nine a_1 and four a_2 vectors.

The nanotube's diameter is the length of chiral vector divided by π. The other structural parameter is the chiral angle, measured between the chiral vector and basis vector a_1. It varies between 0 and 30 degrees. SWCNTs with chiral angle of 0° are called zigzag structures whereas those with chiral angle of 30° are armchair structures.

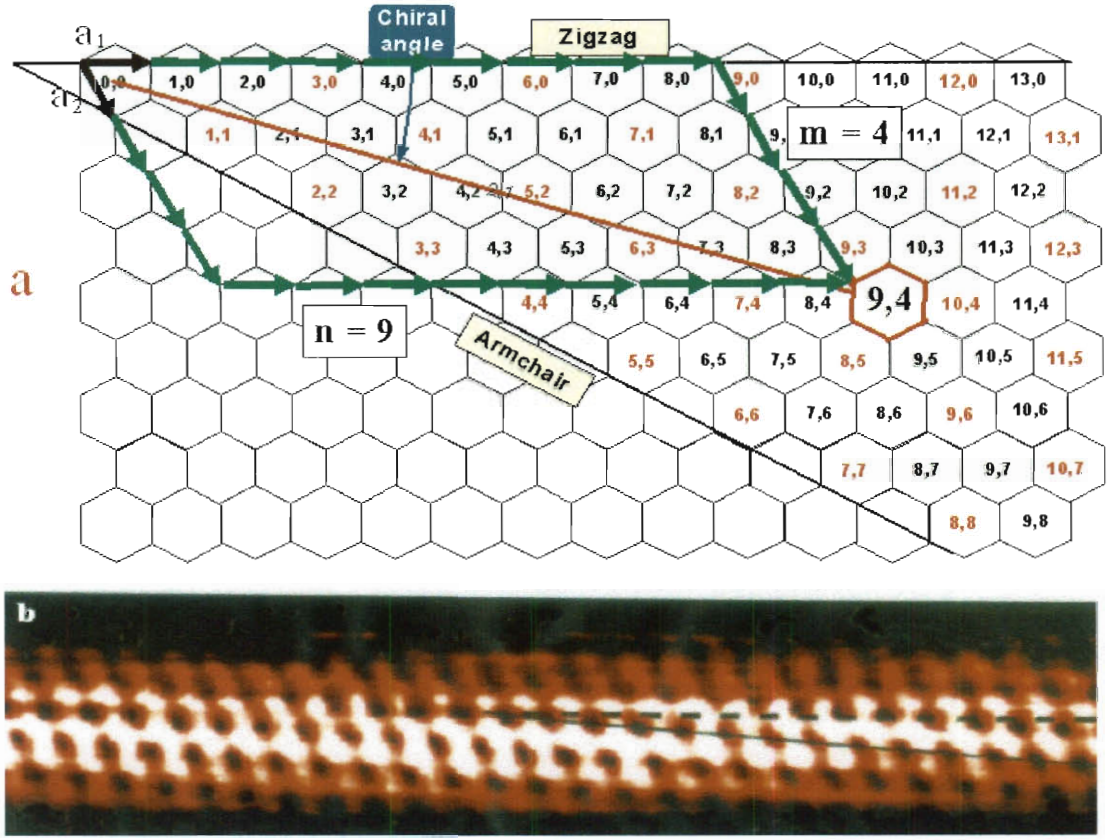

Figure 1. a – carbon nanotube roll up diagram; b – the STM image of chiral SWCNT[17].

1.3 Carbon Nanotube Band Structure

Depending on their structure, carbon nanotubes behave as metallic or semiconducting. Tight Binding calculations[18] show that the nanotubes for which n-m is evenly divisible by 3 have no bandgap (their valence and conduction bands intersect at one point), so they are considered metallic. Other carbon nanotubes have a 1 – 2 eV gap between their valence and conduction bands and therefore are semiconducting (Figure 2). Statistically it is predicted that 1/3 of the total number of carbon nanotubes are metallic[19]. For example, all armchair single-walled carbon nanotubes are metallic due to the fact that their n-m value is equal to zero.

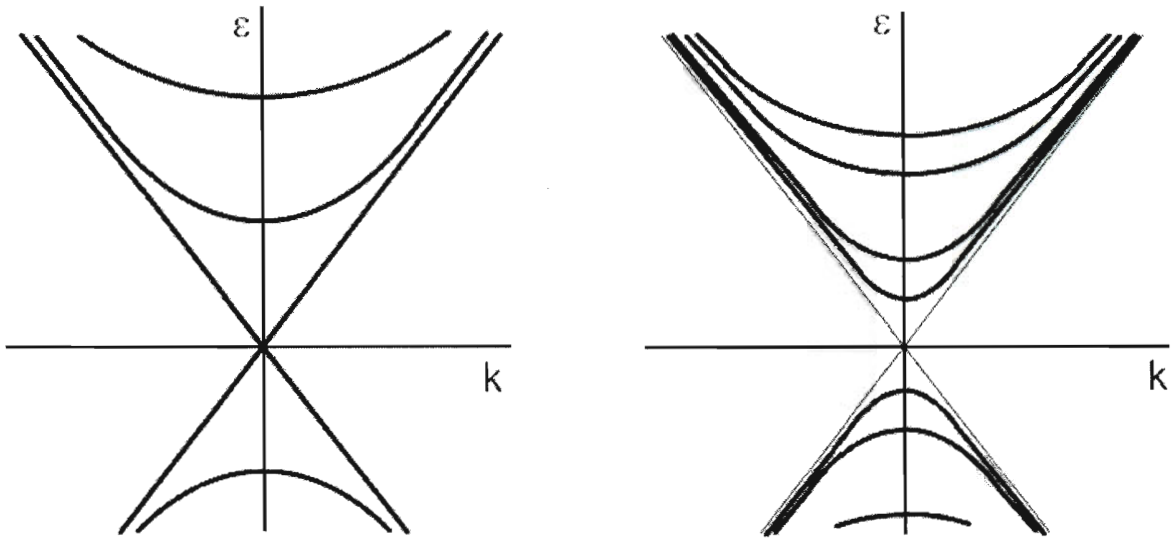

Figure 2. Band structures of metallic (left) and semiconducting (right) single-walled carbon nanotubes.

Due to their 1-dimensional structure, both metallic and semiconducting carbon nanotubes exhibit sharp peaks in their density of electronic states called van Hove singularities (Figure 3). The density of states between c_1 and v_1 subbands for metallic

carbon nanotubes is nonzero (Fig 3. b), which also indicates that they have no band gap. As for semiconducting nanotubes, the band gap is represented by the separation between the first valence (v_1) and first conduction (c_1) subbands (Fig 3. a). Band gap energies E_{11} scale approximately inversely with carbon nanotube diameter.

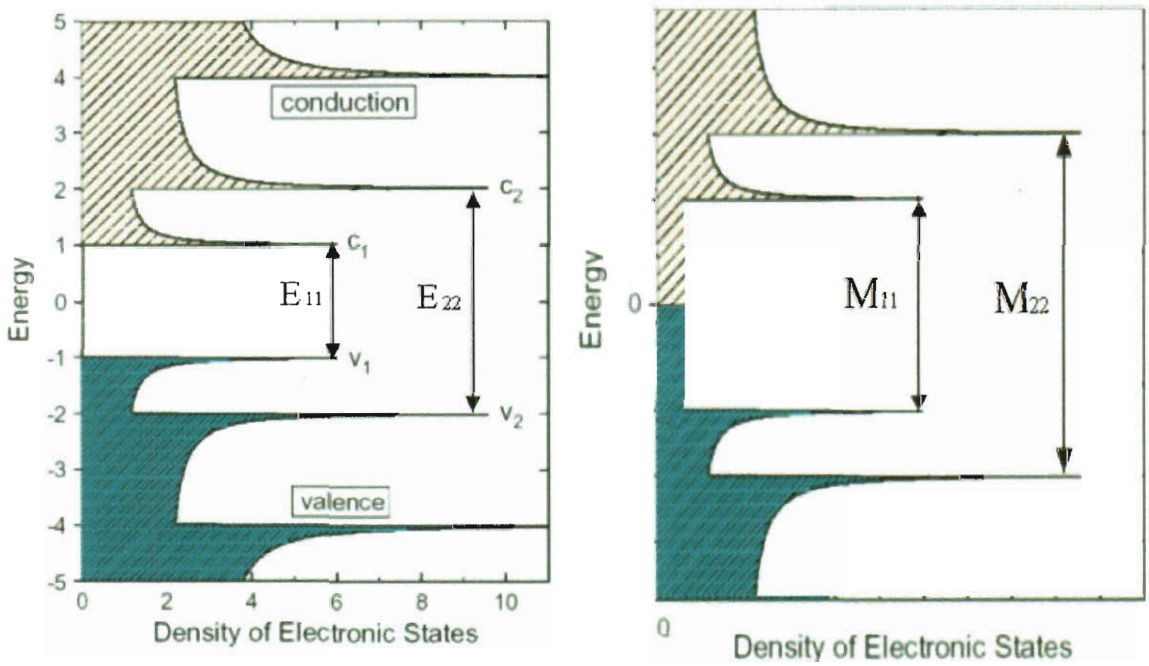

a. b.

Figure 3. a –density of states schematic of a semiconducting carbon nanotube;[20] b - density of states schematic of a metallic carbon nanotube.

1.4 SWCNT Production and Sorting

Carbon nanotubes were discovered in 1991 in Japan.[15] At first, multi-walled nanotubes were found in arc discharges and later on, in 1993, single-walled carbon nanotubes were reported.[21] Since then, a number of nanotube growth procedures have been further developed. One of them involves laser ablation of graphite targets at high

temperatures. At present, the most widespread method is chemical vapor deposition (CVD), in which decomposition of carbon-rich gases on a catalytic substrate yields carbon nanostructures. The first production of SWCNTs by CVD was reported by Dai et al.[22] Further developments of this technique evolved into the HiPco (high pressure carbon monoxide) and CoMoCAT growth processes.[23,24] In the HiPco method, carbon nanotubes are produced by catalytic disproportionation of carbon monoxide gas at high temperatures and pressures. In the CoMoCAT process, disproportionation of carbon monoxide occurs on a SiO_2-supported Co- Mo catalyst at lower pressures and temperatures as compared to HiPco.[24,25] Lower temperature syntheses and stabilization of small cobalt metal clusters by interaction with molybdenum yield CoMoCAT nanotube product with smaller average diameter and a narrower distribution of structures compared to those synthesized at higher temperatures.[26] Although the most refined current growth methods are somewhat selective for nanotube structure and electronic type, many applications require samples that are more highly sorted. For this purpose, several post-growth processing methods have been developed.[27-32] One of the most widely used is density gradient ultracentrifugation (DGU), which can physically sort carbon nanotubes by chirality or electronic type through ultracentrifugation of SWCNT suspensions in a density gradient.[33-35] Another effective method of SWCNT chirality sorting is DNA-assisted separation of SWCNTs in ion exchange (IEX) chromatographic columns. In this approach SWCNTs of certain chiralities wrapped by different ssDNA oligomers exhibit preferential elution in the column depending on the structure of SWCNT/ssDNA hybrids.[28,36,37] The length and the composition of ssDNA sequences are altered to achieve maximum yield for particular SWCNT types.

In addition to chirality, as-produced SWCNTs can be separated by length. Length separation of SWCNTs have been achieved using several methods including extraction into organic phase,[38] density gradient ultracentrifugation,[39] size exclusion chromatography[40-42] and gel electrophoresis.[43-45]

1.5 Applications

Due to their unique properties and the availability of chirality and electronic structure sorted material, SWCNTs play important roles in a number of emerging applications. They are employed as atomic force microscopy probe tips,[46] ultrafast optical switches,[47] and drug delivery agents for targeted cancer therapy.[48,49] Carbon nanotubes are also known to serve as near-infrared (NIR)[50] and radio frequency (RF)[51] absorbers, that when directed into tumors and irradiated with NIR or RF waves, cause tumor heating and destroy cancer cells in the targeted area. SWCNTs can be embedded into a epoxy polymer matrix improving its thermal and mechanical properties. Metallic SWCNTs can be used as efficient field emission sources,[52] in which large electric field gradients can be generated at the nanotube tips by the application of modest electrical potentials. They can also serve as nanoscale electrical interconnects[53] in nano-circuits. Semiconducting SWCNTs may form the basis for next-generation single-nanotube field-effect transistors[54-56] or prove useful as near-infrared fluorescent markers[57,58] in the field of nanomedicine.

1.6 Characterization methods overview

Many such applications require the use of well-characterized SWCNT samples.

Some of the most common methods of carbon nanotube characterization are STM, AFM, Raman spectroscopy, absorption and photoluminescence spectroscopy. High resolution STM can provide well-resolved images of carbon nanotubes (Figure 1b) from which their length, diameter and chirality can ideally be determined. This technique is mostly useful for observing features of individual nanotubes.[17]

AFM also images individual SWCNTs providing information about their length and diameter. Even though AFM spatial resolution is lower than that of STM, the former is more widely used in routine SWCNT characterization as a less laborious technique. AFM has been used to assess length distributions in SWCNT samples[43] and the degree of SWCNT aggregation.[59]

Raman spectroscopy offers a different way of characterization: carbon nanotubes were found to have diameter-specific radial breathing mode vibrations that are active and may be resonance-enhanced in Raman.[18,60] Therefore, knowing the frequencies of the breathing mode Raman peaks, one can determine the diameters of carbon nanotubes that are present in the sample and have electronic resonances near the Raman laser wavelength. Other major SWCNT specific Raman peaks include the G-band, corresponding to the stretching mode of sp^2 hybridized C-C bonds, and the D-band, which is related to sp^3 carbons and to imperfections and defects in the SWCNT.

Absorption spectroscopy of carbon nanotubes[61] is another structure-specific tool widely used for characterization of SWCNT sample composition and purity. Unlike Raman, absorption spectroscopy has advantage of simultaneous signal detection from all SWCNT species. This is often used to estimate the metallic or semiconducting fraction in SWCNT samples based on the ratio of integrated areas under background-subtracted

metallic and semiconducting SWCNT peaks.[62] In addition, absorption backgrounds in SWCNT spectra have been used to evaluate nanotube sample purity.[63] As a result, absorption spectroscopy provides an efficient approach for chirality and electronic structure-specific assessment of SWCNT samples. Finally, one of the latest and most powerful characterization techniques for semiconducting carbon nanotubes in photoluminescence spectroscopy.

1.7 Carbon nanotube photoluminescence

The phenomenon of carbon nanotube photoluminescence was discovered in 2001 by Prof. Weisman's group at Rice University[64]. Single walled carbon nanotubes were studied in aqueous suspension while coated with sodium dodecyl sulfate (SDS) surfactant (Fig 4) that allowed dispersion of individual SWCNTs in water. Surfactant coating together with intense ultrasonic agitation prevented SWCNTs from aggregating into bundles. A centrifugation process was further used to reduce the amount of catalyst particles and nanotube bundles in suspension.

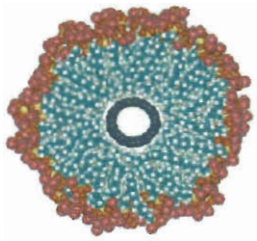

Figure 4. Model of a carbon nanotube suspended by SDS surfactant[64].

Absorption and emission spectra of sonicated and centrifuged carbon nanotube samples were found to have matching spectral features (Figure 5) suggesting that SWCNTs might be displaying so-called "bandgap photoluminescence".[64] In such a

process optical excitation of SWCNTs on higher order transitions may be followed by subsequent emission at E_{11} (Figure 6).

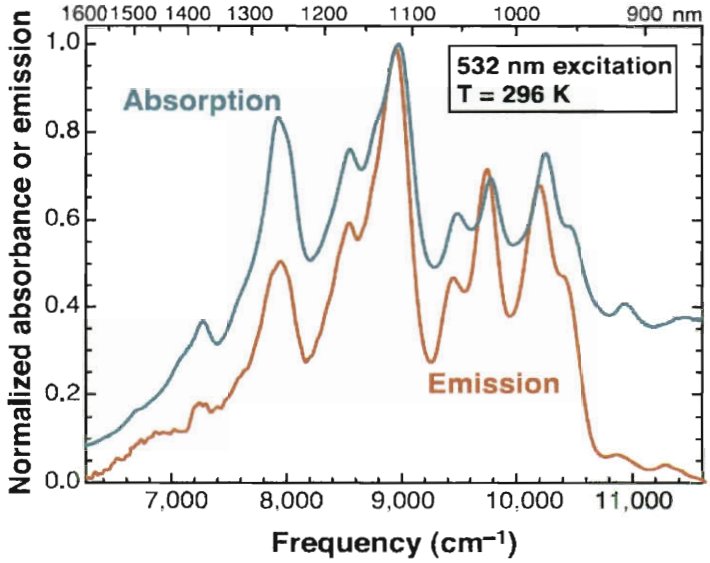

Figure 5. Absorption and emission spectra of carbon nanotubes in aqueous sodium dodecyl sulfate[64].

Various peaks in Figure 5 were analyzed and attributed to different structural types of SWCNTs, which indicted that carbon nanotube photoluminescence is a structure-selective approach.

Pursuing that work, Bachilo et al.[20] have further measured carbon nanotube photoluminescence as a function of E_{22} excitation wavelength and E_{11} emission wavelength. In that process of photoluminescence described by a diagram in Figure 6, an electron from the second valence sub-band, v_2, is excited to c_2 via the absorption of a photon. After that, the excited electron nonradiatively relaxes to c_1, losing its energy to vibrations. This is followed by its final radiative relaxation to v_1 with emission of a near-infrared E_{11} photon.

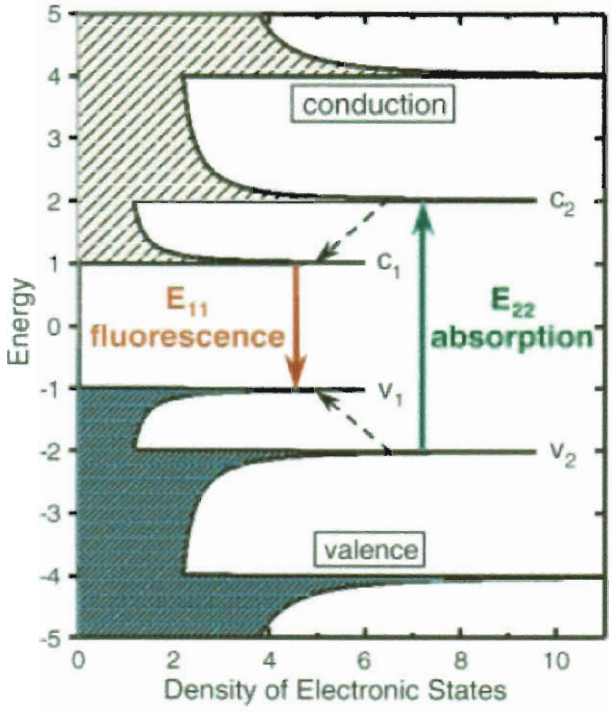

Figure 6. Semiconducting single-walled carbon nanotube photoluminescence energy diagram[20].

The electron-hole pair formed in the excitation process can be considered as a separate entity, an exciton that is bound by Coulomb interaction. Due to the quasi-one-dimensional structure of carbon nanotubes, the binding energy of the exciton is relatively large.[65] That makes excitonic effects important in the optical transitions of carbon nanotubes[66] affecting both absorption[67] and photoluminescence. A number of studies have recently been directed towards characterizing exciton dimensions,[65] excursion lengths,[68,69] mobilities[69] and lifetimes in SWCNTs.[68,70-72] As a result, excitons in pristine SWCNTs were described as ~2 nm wide, with a mean excursion range of 90 to 300 nm as measured for individual SWCNTs, and lifetimes on the order of 5 - 200 ps. Exciton lifetimes are affected by such effects as charge-induced quenching,[73] photobleaching[74]

and exciton-exciton annihilation.[75,76] Excitonic studies provide important insights in to carbon nanotube photoluminescence and photophysics in general.

Based on the apparent structure specificity of SWCNT absorption and photoluminescence spectra (Figure 5), Bachilo et al. have suggested that each type of semiconducting SWCNTs has a specific set of excitation and emission wavelengths. As seen from Figure 7a, the excitation/emission 2D scan revealed a number of well-defined bright spots, each corresponding to a certain chirality of SWCNTs with clearly defined n and m indices.

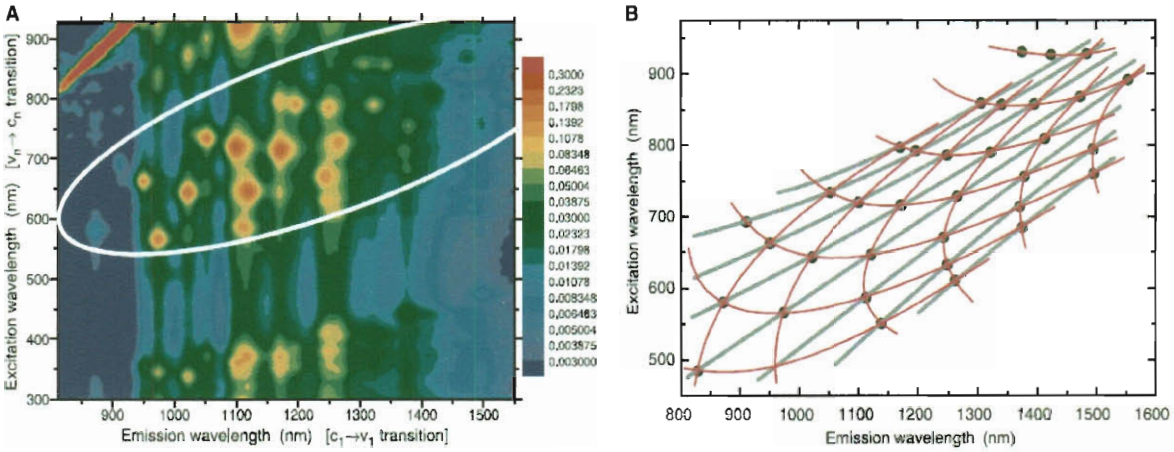

Figure 7. a – Photoluminescence intensity contour plot of excitation versus emission wavelength for carbon nanotubes.[20] b – Perceived structural patterns among the nanotubes in white oval in the frame a.[20]

That discovery was highly important, since it showed that E_{11} and E_{22} transition energies were structure dependent, linking the physical and electronic structures of SWCNTs. It can be clearly seen from Figure 7a that bright spots (excitation/emission peaks) appear in a certain pattern. Bachilo et al. have studied possible structural arrangements that lead to such distribution of peaks on excitation/emission spectrum,

dividing carbon nanotubes into several families according to their values of n and m. Figure 7b shows perceived patterns in the spectral positions of carbon nanotube photoluminescence peaks.

Actual assignments of n and m values to specific peaks in the excitation/emission spectrum (Figure 7) were made with a help of resonance Raman spectroscopy[20]. As described above, SWCNT Raman breathing modes depend on diameters of carbon nanotubes in the sample. [18] The authors have used that to identify the correct structural assignment among several possible ones. As a result, each observed fluorescent peak was tagged with a specific (*n*,*m*) index(Fig 8).

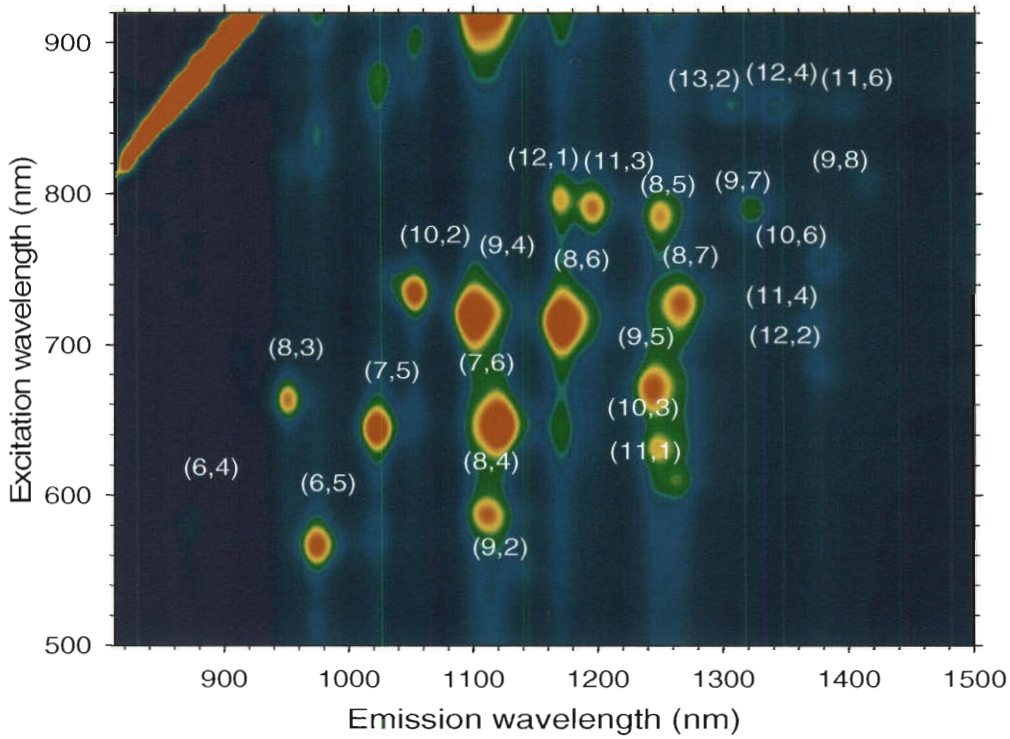

Figure 8. Structure–assigned SWCNT photoluminescence contour plot of excitation versus emission.[20]

This technique opened the way to various revolutionary experiments that require

knowledge of the chirality distribution of carbon nanotubes in various samples.[77,78] It provides efficient characterization for applications that require chirality or electronic structure sorted SWCNT material.[79] This method has also found many other applications since it is sufficiently reliable and easy to perform. For example, the dependence of carbon nanotube photoluminescence on pH[80] or glucose concentration[81] suggests the potential use of carbon nanotubes as biological sensors.

CHAPTER 2

Electric Field-Induced Quenching of Single-Walled Carbon Nanotube Photoluminescence[82]

2.1 Introduction

Due to their outstanding physical, electronic, and thermal properties[83] carbon nanotubes are currently a subject of intense research even beyond the field of spectroscopy. Potentially, they can be used in different areas of science such as atomic force microscopy where carbon nanotubes are already being employed as AFM tips.[84] They are suitable for such applications due to their high Young's modulus, which is on the order of one terapascal.[85] A great interest is directed towards the applications of SWCNTs in modern electronics. Their ballistic conductivity[86] allows metallic SWCNTs to be used as efficient conductors. Semiconducting SWCNTs have already demonstrated to be essential components in field-effect transistors.[54,55] In these transistors SWCNTs serve as a semiconducting medium, a link between the source and a drain. Some of the devices have advanced to the point where the primary carriers in the carbon nanotube can be selected by applying a bias of a certain sign.[87] Such transistors can be used as

microscopic optoelectronic devices exhibiting controlled electroluminescence upon the injection of holes and electrons from the source and drain electrodes.[88,89] Optoelectronic properties of SWCNTs were further studied to observe Raman, photoluminescence and electroluminescence signals from a single suspended single-walled carbon nanotube in a field effect transistor.[90] Furthermore, the dependence of those phenomena on the perturbation of electric field created by the change in the gate voltage was observed.[91] That allows controlling photoluminescence and electrolumoinescence emission from SWCNT-based transistor devices through the gate electrode. Due to the importance of field effects on SWCNT optical and electronic properties, several theoretical investigations have been conducted modeling those properties in the presence of electric and magnetic fields.[92-95] Those studies[92,93,95] suggested that applying a transverse electric field to semiconducting carbon nanotubes would cause a change in bandgap, affecting the lifetime of the excited states and the probability of optical transitions. The applied electric field was also predicted to shift absorption peaks and increase their number by lowering degeneracy.[96] The latest theoretical studies predict significant effects of longitudinal electric fields on absorption and nonradiative excitonic decay in SWCNTs.[97] A lack of experimental evidence on that subject provided an incentive for investigating electric fields effects in SWCNTs. We used photoluminescence spectroscopy and imaging of semiconducting carbon nanotubes[64] as a powerful tool for detecting photoluminescence intensity variations or any significant shifts in nanotube energy level structure resulting from the applied electric field.

Currently it is possible to detect the photoluminescence of individual SWCNTs using near-infrared microscopy.[98] This method allows observing and characterizing them

by length, (*n,m*) identity, orientation in space, etc. Such single-particle spectroscopy opens the possibility for determining the electronic and optical properties of individual carbon nanotubes. Using that approach, we studied the behavior of individual carbon nanotubes in longitudinal and transverse electric fields. Although no significant spectral shifts were found in the present work, we observed dramatic decreases in photoluminescence intensity of carbon nanotubes in longitudinal electric fields.

2.2 Experimental

2.2.1 Sample Preparation

Individual SWCNTs spatially isolated in a poly(methyl methacrylate) (PMMA) matrix were obtained from the raw HiPco nanotube material. At first, HiPco carbon nanotubes were dispersed in water with addition of 1% Triton-X surfactant and bath sonicated for one hour in FS 145 Fischer Scientific bath sonicator. That suspension was then centrifuged at 12000 × g and the top decant was collected. That process helped to reduce the concentration of nanotube bundles and impurities in suspension: bath sonication broke up large bundles and helped to mix carbon nanotubes with surfactant in water, whereas centrifugation precipitated heavy nanotube bundles that were later discarded. Aggregation is undesirable in our experiments due to quenching of SWCNT photoluminescence via charge or energy transfer to metallic SWCNTs present in bundles. After centrifugation, a couple of drops of nanotube suspension in aqueous Triton-X were added to ~5 % PMMA solution in o-xylene. The opaque product obtained after mixing water and xylene solutions was tip ultrasonicated using a Microson Ultrasonic Cell Disruptor at a power high enough to stimulate water evaporation. That was done with the

purpose of randomly dispersing and incorporating SWCNTs inside the PMMA matrix. Large ultrasonicator tips were used to deliver maximum power without damaging individual nanotubes. Due to the immiscibility of xylene and water and the fact that the boiling point of water (100°C) is lower than that of xylene (114°C), the water evaporated from the solution first. With no water present, the liquid became transparent. In addition to evaporating the water, tip ultrasonication facilitated dispersion of SWCNTs in the PMMA solution and wrapping of SWCNTs with PMMA molecules, which prevented SWCNT aggregation as seen from SWCNT photoluminescence spectra. Two types of PMMA with molecular weights of 350,000 and 996,000 were used in experiments. The longer-chain polymer was considered more rigid and therefore more durable.

After such preparation several droplets of dilute SWCNT suspension in PMMA/xylene were spin-coated onto a fused silica microscope slide with electrodes on it. During the process of spin-coating, the solvent quickly evaporated, leaving a clear PMMA film several micrometers thick with embedded individual SWCNTs. The small thickness and high uniformity of the PMMA films was achieved by using relatively low concentrations of PMMA in o-xylene, resulting in a polymeric solution of a moderate viscosity that could spread uniformly over the slide with electrodes.

2.2.2 Electrodes

Two types of electrodes were employed in our experiments. First, we used glass microscope slides coated with a thin highly transparent layer of ITO (indium tin oxide). The films of PMMA with embedded carbon nanotubes were deposited on the surfaces of two slides that afterwards were compressed together creating a parallel plate capacitor

with a ~ 15μm PMMA-filled gap (Fig 9).

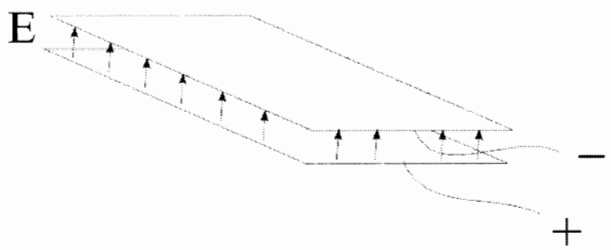

Figure 9. Parallel plate ITO electrodes.

In such a capacitor, carbon nanotubes in PMMA positioned between the plates were subject to electric fields of up to 20 V/μm. At higher voltages some film samples experienced breakdown. The main disadvantage of that configuration was that in the process of spin-coating, due to stretching of the film along the surface of a slide, most of the nanotubes in the film became oriented in the plane of the electrodes and, therefore, perpendicular to the applied field. Such orientation, as explained further in the text decreased the magnitude and hampered the observation of the electric field effects.

Several other configurations of electrodes were used. One of them consisted of a plastic film with an array of gold electrodes (Figure 10).

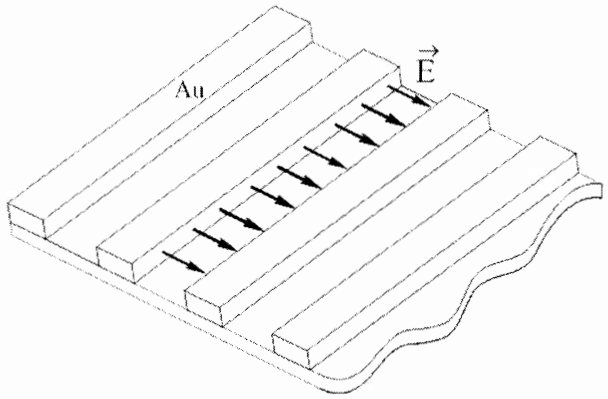

Figure 10. The array of gold electrodes on the plastic film substrate

The plastic substrate itself had some fluorescent emission in the NIR, so a 1250 nm long-pass filter was used to block its photoluminescence. The electrodes consisted of 50 μm wide gold stripes on plastic substrate separated by 50 μm gaps and connected to two separate terminals. In such a configuration, voltages of up to 250 V were applied to electrodes to create fields on the order of several volts per micrometer between them. The piece of film with electrodes was attached to a microscope slide and spin-coated with nanotubes in PMMA.

Later on, a similar array of gold electrodes on a glass substrate was used. These electrodes consisted of 20 μm gold stripes wide with 20 μm gaps between them. Since the 1250 nm filter was no longer needed with a glass substrate, photoluminescence from a larger variety of SWCNT types could be observed.

Another configuration of electrodes was used to vary the direction of the electric field for a certain nanotube situated between the electrodes. It consisted of four triangular electrodes with a gap of about 50x50 μm (Figure 11). These electrodes were fabricated by depositing a nanometer layer of titanium and then a 15 nm layer of gold on the surface of a quartz slide. The triangular electrode pattern was achieved by making two orthogonal

scratches that removed the gold from the surface of the slide.

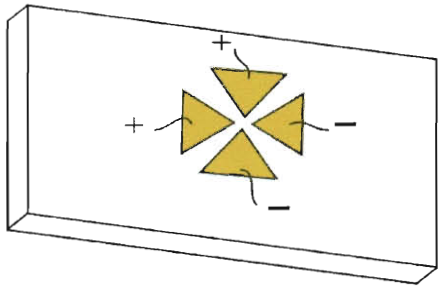

Figure 11. Triangular electrodes for variable field direction.

The individual nanotubes in the gap between the electrodes were subjected to electric fields directed at 0, 45 and 90 degrees to their axes. The direction of electric field was controlled by applying the voltage to certain electrodes or groups of electrodes. As a result, the electric field was rotated 360 degrees clockwise with angle increments of 45 degrees while the photoluminescence from specific individual SWCNTs was recorded.

2.2.3 Photoluminescence microscopy setup

In our experiments the photoluminescence of individual carbon nanotubes was constantly monitored to observe possible changes caused by the electric field. That was done using a standard photoluminescence setup[98] (Figure 12).

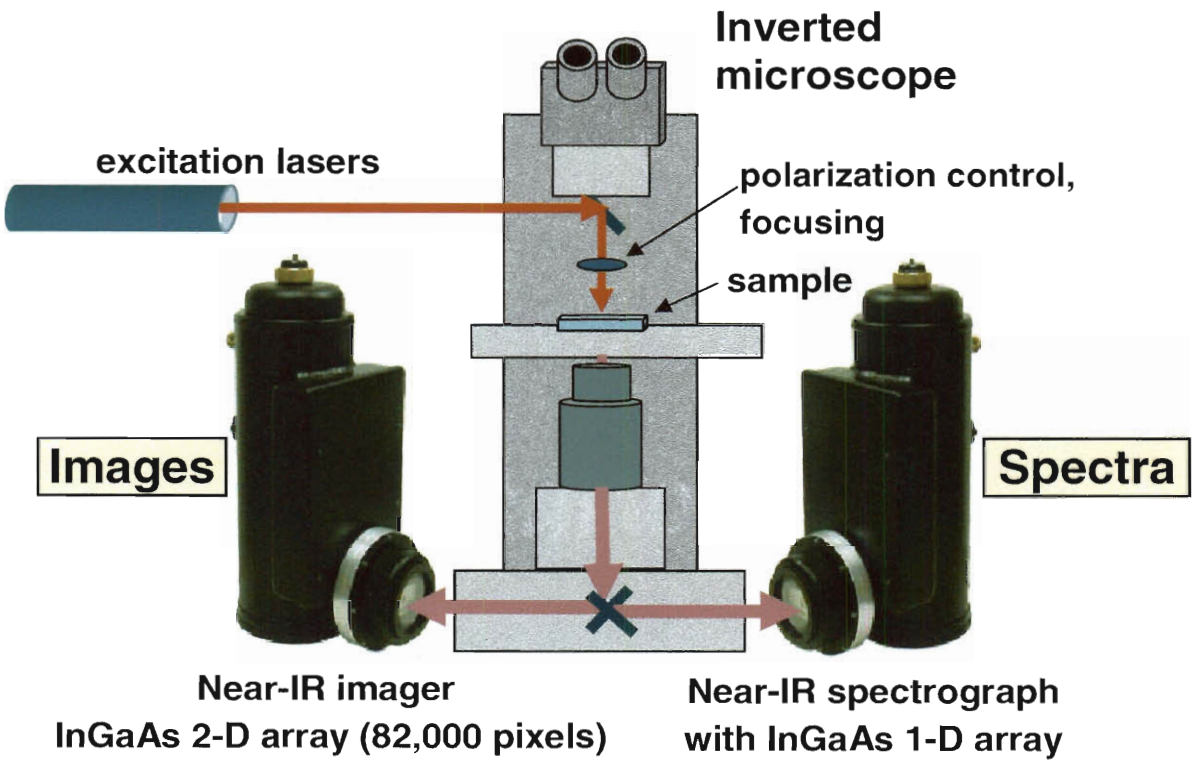

Figure 12. Photoluminescence microscopy setup diagram.[98]

In this setup, 785 nm or 660 nm semiconductor diode lasers were used as an excitation sources. After a series of mirrors and a polarizer, laser light went through a half-wave retardation plate that was used to rotate its polarization plane in order to determine the orientation of carbon nanotubes in PMMA with respect to the electrodes. It is known that carbon nanotubes exhibit the most efficient excitation when light is polarized along their axis. Therefore, the orientation of individual nanotubes in the plane of the film was found by maximizing the fluorescent signal while rotating the polarization of excitation beam with the half-wave retardation plate. After going through the half-wave plate, the light was focused onto the sample by an aspheric lens. The lateral position of the focus was adjusted manually. The sample itself was situated on a translation stage connected to a computer-controlled step motor.

The photoluminescence from the sample of nanotubes in PMMA was collected by 60x water- or oil-immersion objectives on a Nikon TE-2000U inverted microscope and directed into one of five possible output ports. Two outputs were coupled respectively to an InGaAs NIR Roper OMA-V 2D camera and a NIR spectrograph equipped with an InGaAs Roper OMA-V array detector. The camera allowed observing photoluminescence of individual SWCNTs situated in between the electrodes, while the NIR spectrograph was used for recording the emission spectra of those nanotubes.

In that way, we were able not only to detect the photoluminescence of individual carbon nanotubes (Fig 13) but also to obtain their photoluminescnce spectra and classify them by their (*n*,*m*) structure.[20,98] The spectrum of a particular nanotube was recorded by moving it to a certain position on the screen (Fig 13) and accumulating the spectrum of that region (0.5x0.1 mm). The spectra were usually recorded as an average of 10 accumulations of 10 seconds each.

Figure 13. Image of carbon nanotubes in PMMA on NIR camera. Each bright spot represents an individual carbon nanotube or a small nanotube cluster.

The voltage was supplied to electrodes by a Tektronix AFG 2020 signal generator through a two-channel Trek 603 power amplifier with an output of up to 250 V. In

experiments on carbon nanotube photoluminescence quenching, DC voltage was used primarily.

2.2.4 Bulk measurements

In addition to observing individual nanotubes we have also studied the bulk sample photoluminescence from carbon nanotubes embedded in PMMA films. These films were prepared as described above, only using high concentrations of nanotubes and PMMA in xylene. Instead of spin-coating, polymer with large amount of embedded carbon nanotubes was dried on a surface of a glass slide. As a result we obtained rather thick ~0.5mm dark colored films. Such films supplied enough signal for quantitative bulk sample photoluminescence measurements. Later on, each film was stacked between two ITO coated electrodes (Figure 9) and subjected to electric fields of up to 2 V/μm.

The photoluminescence of the films was recorded using a SPEX Fluorolog 3 spectrofluorometer with single-channel InGaAs detector (Figure 14).

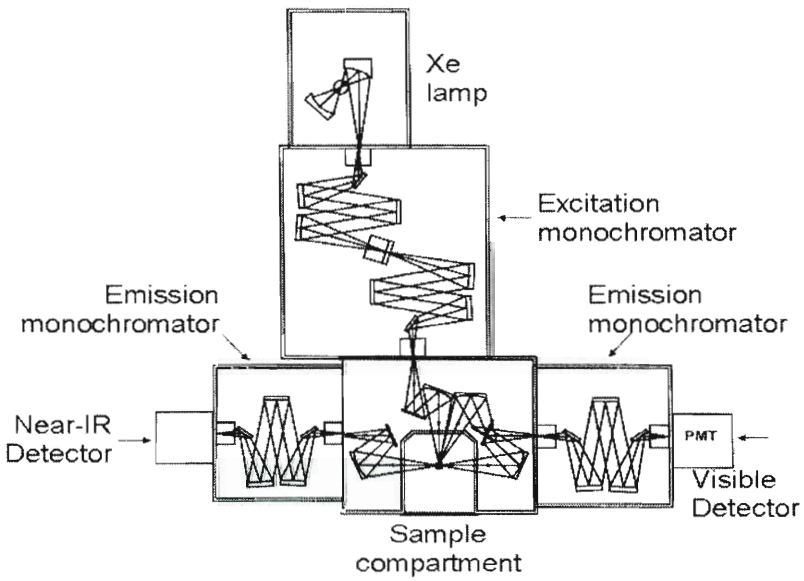

Figure 14. Diagram of SPEX Fluorolog 3 spectrofluorometer.

A Xe lamp served as an excitation source for most of the experiments. The light from the lamp went through a monochromator (Figure 14) that passed a specific excitation wavelength chosen excite the sample. Then, spectrally selected photoluminescence from the PMMA/SWCNT film was directed to a cooled InGaAs detector and presented as a spectrum containing photoluminescence peaks from multiple nanotube species present in the sample. Spectral changes under electric field were observed and analyzed. When a higher photoluminescence signal was necessary to obtain precise quantitative measurements, 980 or 655 nm diode lasers were used as excitation sources.

2.3 Results

2.3.1 SWCNT photoluminescence intensity quenching in the electric field

The effects of the electric field on carbon nanotube photoluminescence were observed with the setup described above. First, the photoluminescence of individual carbon nanotubes was studied using ITO-coated microscope slides as electrodes (Figure 9). Further studies were conducted mostly with gold array electrodes for the reasons described below. In this series of experiments it was discovered that under electric fields of the order of several V/μm, the intensity of fluorescent emission of many carbon nanotubes drastically decreased (Figure 15). Such photoluminescence quenching was recorded at several values of the electric field. The effect was shown to be reproducible and highly reversible: when the voltage was turned off, the fluorescence intensity of carbon nanotubes restored nearly to its initial value (Figure 15).

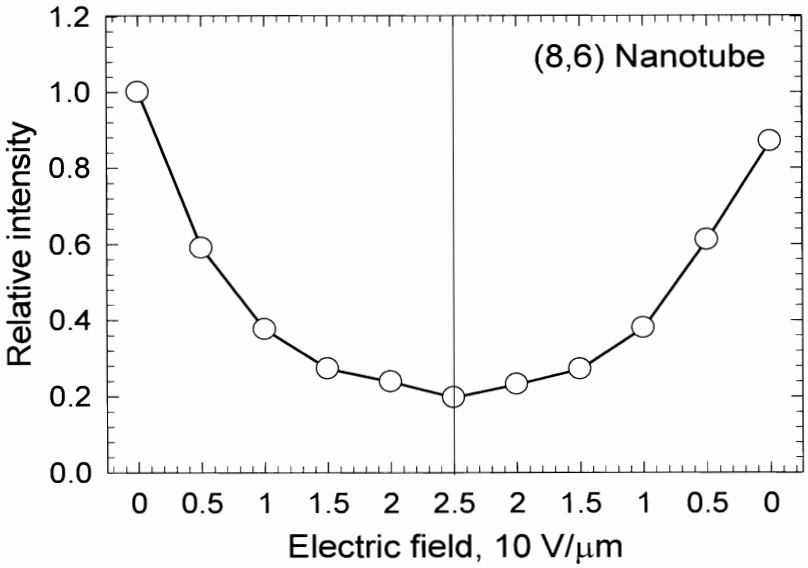

Figure 15. The quenching of the photoluminescence intensity of a single carbon nanotube as a function of applied field. Reversibility of the quenching is apparent.

Each photoluminescence quenching curve was averaged over several runs and plotted versus the increasing field. For example, Figure 16 shows the quenching curve of an (8,6) nanotube oriented at 50 degrees to the electric field. The nanotube type was found from the wavelength of its emission peak recorded with spectrometer. The insets show 2-D fluorescence images of the nanotube at particular values of the electric field. It is possible to infer from this graph that carbon nanotubes experience strong, nearly exponential photoluminescence quenching at the fields of ~ 1 V/μm. In fact, as seen from insets, at higher fields it is hard to distinguish nanotube photoluminescence from the background.

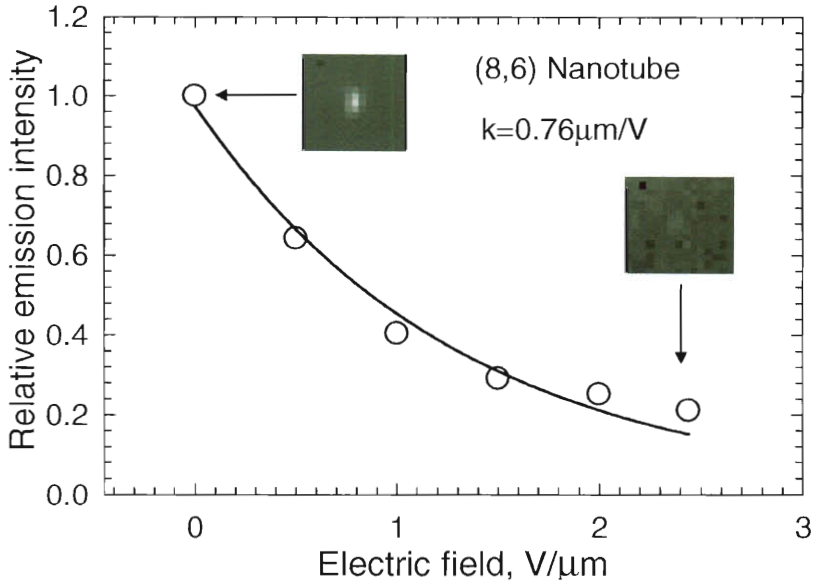

Figure 16. Carbon nanotube photoluminescence quenching curve averaged over several runs and fitted with exponential function.

The data in Figure 16 were fit with a decaying exponential function (Eq. 1) with fixed amplitude and a single parameter, k, that describes the steepness of the curve and therefore the sensitivity of carbon nanotube photoluminescence intensity to applied electric field.

$$I = \exp(-k \cdot E) \tag{1}$$

Several other fit functions were tried, including an inverse hyperbolic cosine (Eq. 2) that sometimes represented quenching curves more accurately than the simple exponential. In Eq.2, k again is a quenching parameter that shows how the photoluminescence intensity decreases with the electric field, E.

$$I = \frac{1}{(\cosh(k \cdot E))} \tag{2}$$

As later studies have shown, out of several hundreds of SWCNTs studied in this

work, carbon nanotubes that experience weaker quenching at low fields exhibit behavior that resembles inverse hyperbolic cosine more than exponential (Fig .17).

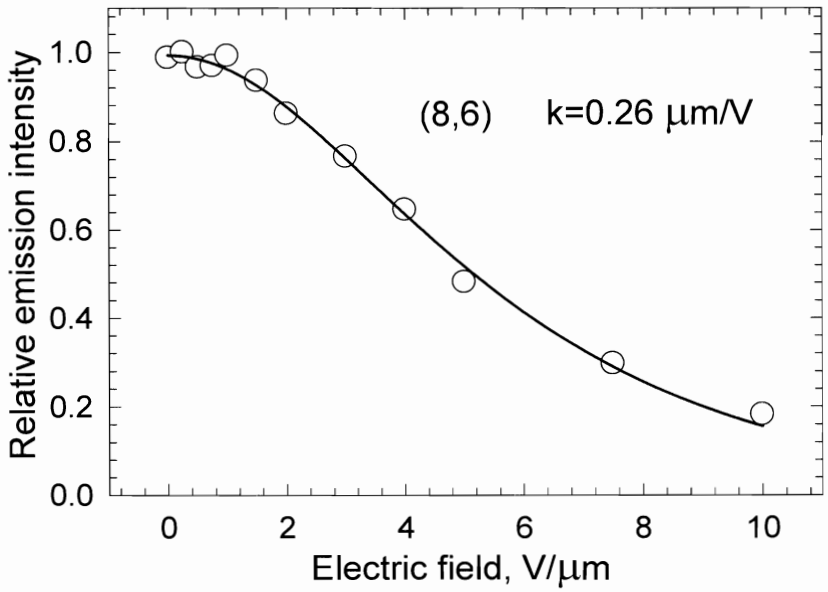

Figure 17. Inverse hyperbolic cosine fit of carbon nanotube photoluminescence quenching curve.

As seen from Figure 17, the first part of the curve could not be described by a single-parameter exponential. Nevertheless, if one would apply higher electric fields at the beginning, or if the nanotube would be more sensitive to the field, the flat part of the graph (Figure 17) seen at the lower fields of 0 to 1.5 V/μm would be less evident, making the quenching curve look more like an exponential. That could explain why quenching curves for some SWCNTs had apparent exponential forms and for others did not. For example, one can see that the carbon nanotube represented by Figure 16 was very sensitive to the electric field: at small fields around 1 V/μm the photoluminescence was

already quenched by 70%, which is also reflected by the high quenching parameter k = 0.76 μm/V. That could imply that we simply have not observed a flat part of the quenching curve for that nanotube because the quenching was already high at small fields, resulting in the quenching curve of apparent exponential form. This example suggests that inverse hyperbolic cosine may be used as the simplest universal function to model carbon nanotube photoluminescence quenching in the electric fields.

2.3.2 Possible theoretical explanations

There could be several theoretical explanations for the observed photoluminescence quenching phenomenon. One possible model accounts for the direct effect of electric fields on excitons in carbon nanotubes. As presented before, excitons could be considered as electrostatically bound electron-hole pairs with binding energies on the order of 400 meV.[65] When an electric field is applied, unless the nanotube is perpendicular to the field, the electron and the hole in the exciton are pulled towards the opposite ends of the nanotube. Although the fields of 1 V/μm may not be large enough to tear an exciton apart, they may increase the probability of exciton dissociation. This idea can be illustrated by modeling an exciton potential well in the presence of the electric field. Such a model involves a simple simulation of Coulomb interactions of an electron and a hole on a cylindrical carbon nanotube of 1.1 nm diameter. Dielectric screening and the effects of the surrounding dielectric environment were taken into account by introducing an effective dielectric constant for carbon nanotubes in the range of 3 to 6.

The outcome (Figure 28) appeared to be consistent with experimental results and calculations in ref. [65], where the binding energy of the exciton in a carbon nanotube was

found to be 420 meV and electron-hole separation – on the order of 1 nm.

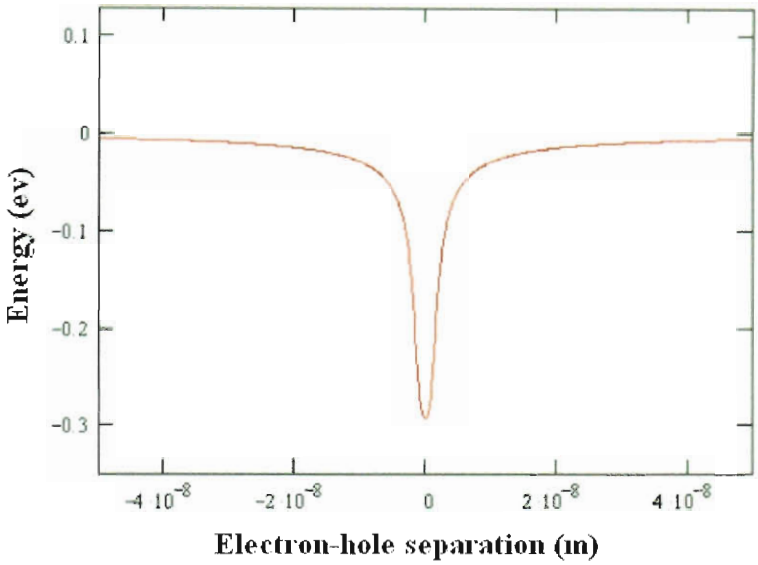

Figure 18. The potential well of an exciton with no electric field applied

When an electric field of 4 V/μm was introduced into calculation, it tilted the potential (Figure 29) increasing of the probability of tunneling-induced exciton decay through the right wall of the potential well.

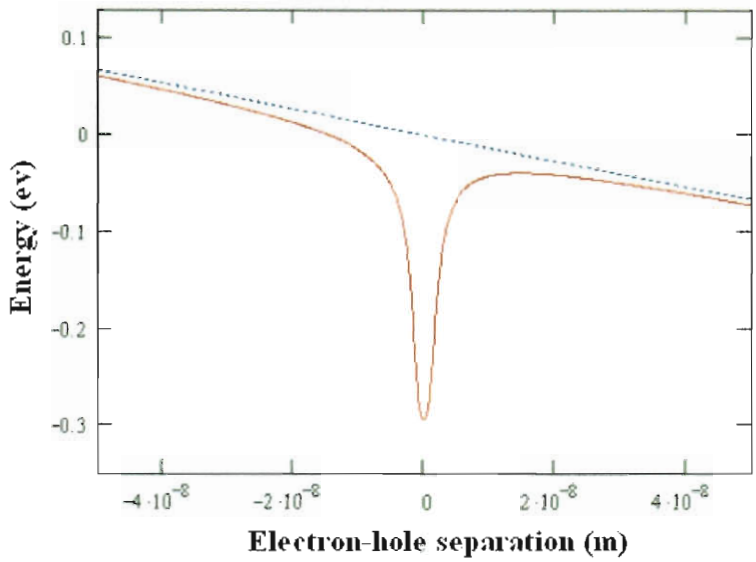

Figure 19. The potential well of an exciton with electric field of 4 V/μm applied.

This idea of exciton dissociation in the electric field was later supported by Perebeinos et. al.[97] Their calculation, based on a solution of the Bethe-Salpeter equation for bound states of a two particle system (exciton), has shown a non-zero probability of electron or hole tunneling out of the exciton potential well. That probability increased considerably with applied electric field. After such dissociation, the electron could experience non-radiative phonon-assisted relaxation to the ground state, diminishing the radiative decay rate and, therefore, quenching the photoluminescence.

A couple of experimental reports based on photocurrent measurements in SWCNT films also support the concept of exciton dissociation.[99,100] They suggest that in the presence of sufficient electric fields, SWCNT excitons experience field-assisted tunneling into the free carrier states.

Another possible mechanism of carbon nanotube photoluminescence quenching by electric field could arise from charge carrier effects. In the series of additional

experiments, we showed that semiconducting carbon nanotubes acquire positive or negative charge depending on the solvent they are suspended in. In these experiments, SWCNTs dispersed in different liquid solvents and placed on the surface of gold array electrodes moved to either only positive or only negative electrodes when the electric field was applied. That indicates the presence of net charge of one particular sign on the SWCNT.

Thus, if an exciton runs into a charge carrier, whether it is an electron or a hole, it can collapse and instead of emitting a photon give its energy to the carrier it encountered, promoting it into a higher state. Such Auger quenching processes would decrease the intensity of the nanotube's fluorescence emission. Field-induced exciton dissociation would contribute to this type of quenching by creating additional charge carriers.

When an electric field is applied, the charges that were previously trapped[65] in defects or weakly bound elsewhere on the SWCNT surface could become mobile and drift towards the ends of the nanotube. Then, due to accumulation of charged carriers, greater photoluminescence quenching would be expected at the ends, or particularly at one end if, as suggested previously, there is initially an excess charge of one sign on the nanotube.

This predicted effect was detected experimentally in relatively long (3-4 μm) carbon nanotubes. In such SWCNTs it was possible to optically resolve the ends and record the photoluminescence intensity at each end as a function of applied electric field. As a result we have obtained a quenching curve for each end of a long (9,5) nanotube (Figure 20) in the electric field. The direction of the electric field was varied by increasing voltage from -50 V to zero and then up to +50 V, thereby reversing the field

vector.

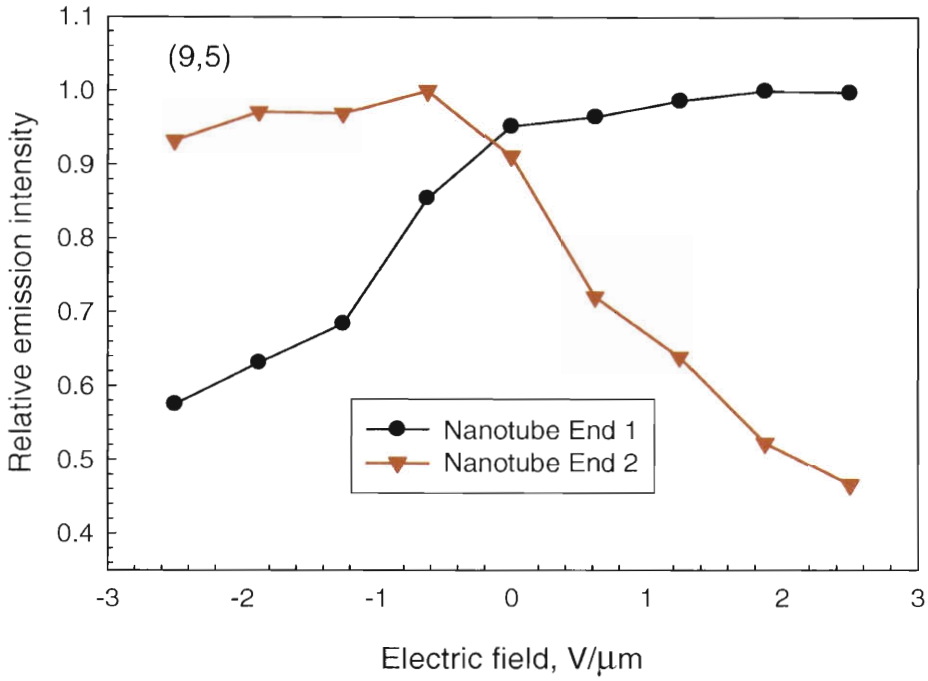

Figure 20. Photoluminescence quenching for two ends of a long carbon nanotube. The insets show fluorescence images of a nanotube at particular values of electric field.

As seen from Figure 20, depending on the direction of the electric field, different ends of carbon nanotube experienced a decrease in fluorescent emission intensity: end 2 quenched at positive voltages and did not quench at negative ones, whereas end 1 did not quench at positive voltages but experienced strong quenching when negative voltage was applied. That finding can be explained by the charge carrier quenching model: in the presence of an electric field a charge of one sign accumulated on the SWCNT surface would move towards one end of the nanotube and stay there, quenching photoluminescence in that particular area. The other end where charge carriers are mostly depleted would not experience significant quenching. When the direction of the field is

reversed, the carriers are expected to move to the other end and quench the photoluminescence there. That is also reflected in Figure 20: when the field polarity is reversed, the opposite end of the nanotube quenches and the one that was quenched before recovers its photoluminescence intensity. As a result, the decrease of fluorescence intensity at the ends of carbon nanotube shown in Figure 20 suggests that charge carrier quenching could be an important component of electric field induced photoluminescence quenching in carbon nanotubes. Thus, we propose that the actual SWCNT photoluminescence quenching process may be a combination of the exciton dissociation and charge carrier quenching effects.

2.3.3 Angle dependence

In the electric field experiments we observed that carbon nanotube photoluminescence quenching was significantly stronger if gold array electrodes (Figure 10) were used instead of the ITO parallel plate electrode configuration. In the experiments with ITO electrodes, the photoluminescence intensity decrease was just noticeable at 3.13 V/μm and became significant at about 18-25 V/μm, whereas in the case of using gold array electrodes, the photoluminescence intensity was already quenched significantly at 2 V/μm. A possible reason for that difference could be that, as mentioned before, during the process of spin-coating SWCNTs were mostly spread on top of ITO electrodes in the plane parallel to them. That way, most of the SWCNTs appeared to be nearly perpendicular to the electric field lines. However, on gold array electrodes, where the electric field was parallel to the substrate, after spin-coating the carbon nanotubes were oriented at various random angles to the field. This suggests that photoluminescence

quenching varies with the angle between the nanotube axis and the electric field with minimum quenching in the perpendicular configuration. It can be proposed then, that only the component of electric field along the nanotube contributes to its photoluminescence quenching. That idea is consistent with assumptions listed in reference [97], where the critical component of the electric field is oriented along the SWCNT axis.

To explore this point, photoluminescence of carbon nanotubes found at different angles to the field was studied. In the series of experiments, quenching curves were recorded for several nanotubes at various angles and their quenching coefficients were calculated using the inverse hyperbolic cosine approximation. We found that with increasing angle between the nanotubes and the field lines, the rate of photoluminescence quenching and, therefore, the quenching coefficient k, decreased (Figure 21).

Since we now observe that carbon nanotube electric field-induced photoluminescence quenching depends on the projection of electric field along the nanotube axis, the expression for the quenching curve hyperbolic cosine fit in Eq. 2 may be modified to:

$$I=\frac{1}{(\cosh(-k_0\cdot|\cos(\alpha)|\cdot E))} \qquad \text{(Eq.3)}$$

where $|\cos(\alpha)|\cdot E$ is the projection of the electric field on the nanotube axis and k_0 is a quenching coefficient independent of the angle.

Thus, in order to come back to regular hyperbolic cosine fit we can incorporate the angle dependence in the quenching coefficient: an actual quenching coefficient k would be then represented as $k_0\cdot\cos(\alpha)$. Such angle dependence of the actual quenching

coefficient was tested by fitting the data (k versus α) in Figure 21 with a cosine curve. The fit was very successful suggesting that photoluminescence quenching depends on the projection of the electric field on the nanotube axis.

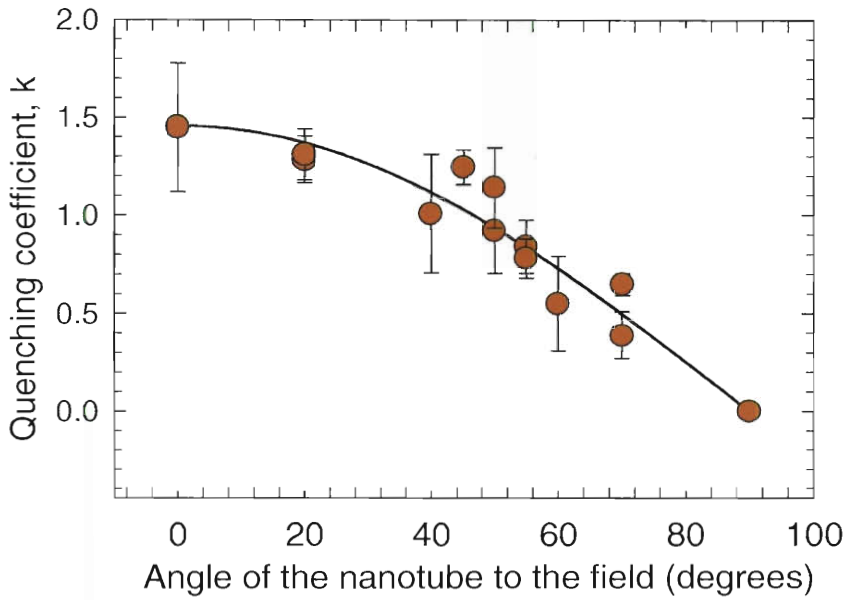

Figure 21. Cosine fit of the quenching coefficient dependence on the angle between the nanotube and the electric field.

Deviations from cosine behavior could be explained by the fact that quenching may also depend on some other parameters not controlled in that experiment. Among them are the presence of possible structural defects, carbon nanotube length, and diameter, all of which vary from nanotube to nanotube. To eliminate those variables we have observed the electric field angle dependence of photoluminescence quenching for one stationary nanotube. In that experiment, the angle between the electric field and the SWCNT axis was varied from 0 to 360 degrees in 45 degree increments using specially fabricated electrodes (Figure 11). At each angle photoluminescence quenching for 50 V

applied to electrodes was recorded. After the quenching amplitudes were normalized and corrected for non-uniform distance from nanotube position to all four electrodes, they were plotted (Figure 22) and fit with the absolute value of $\cos(\alpha)$.

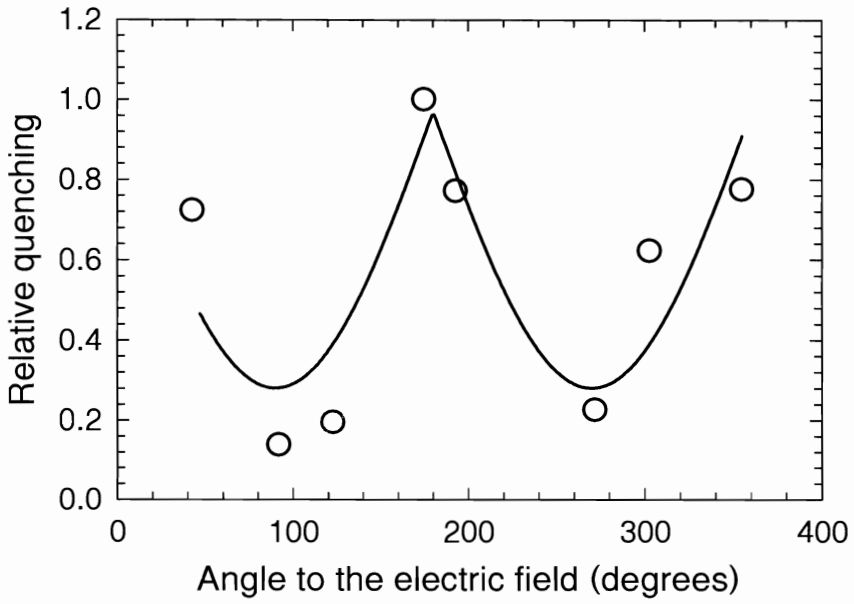

Figure 22. Single nanotube photoluminescence quenching in the rotating electric field.

The single-nanotube measurements in figure 22 show nearly $|\cos(\alpha)|$ behavior. The deviations from the fit could be caused by imperfections in the electrodes, variations in the fluorescence intensity over multiple quenching events, possible defects and the presence of bundles, metallic nanotubes or particles around the studied SWCNT.

Apart from uncontrolled parameters, imperfections in the electrodes and uncertainty in the estimates of field geometry, figures 21 and 22 illustrate that carbon nanotube photoluminescence quenching in the electric field is highly angle-dependent and that the quenching coefficient is proportional to the cosine of the angle between the

nanotube and the electric field.

2.3.4 Length dependence

SWCNT length effects on electric field-induced photoluminescence quenching were also studied. Nanotubes used in these studies were only mildly ultrasonicated during the dispersion process to avoid ultrasonication-induced SWCNT scission and incorporated into PMMA matrix. Their quenching curves were recorded and compared (Figure 23) to the quenching of average-length nanotubes.

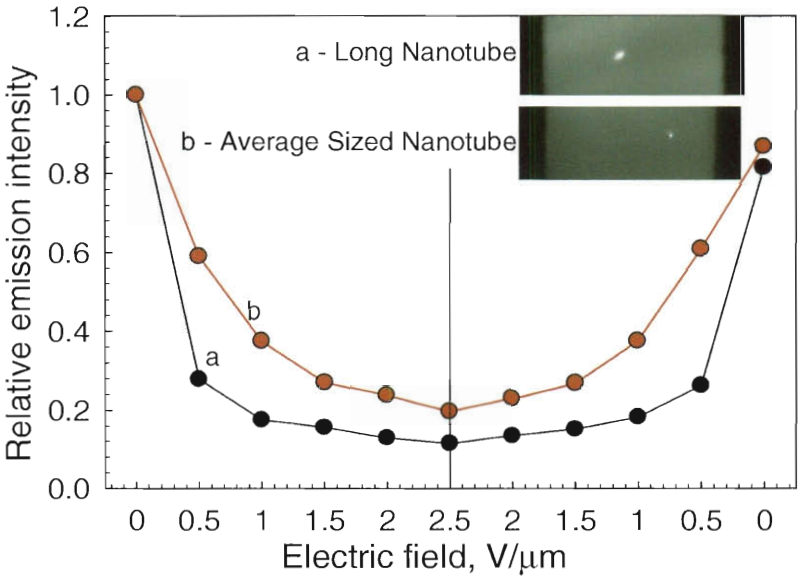

Figure 23. The electric field photoluminescence quenching of the long and average sized carbon nanotubes, both oriented at 50 degrees to the electric field. The insets show photoluminescence images of long and average carbon nanotubes between the electrodes.

As a result of one of such comparison, Figure 23 shows that the longer nanotube experiences significant quenching at lower voltages until it reaches some threshold at

which the quenching process slows down, whereas the shorter one quenches more gradually. This was observed to be a common effect among longer SWCNTs studied in our experiments.

Such a difference in the quenching behavior can in principle be the described by charge quenching model. We note that longer nanotubes may statistically have a larger number of quenchers (such as charge carriers) than the shorter ones. Then, even at low fields, when gathered at one end of the nanotube, all those carriers would cause a significant quenching similar to the one observed initially for longer SWCNT in figure 23. When that end is quenched completely the other one would retain a significant percent of the intensity that would not decrease with the electric field, since all the quenchers moved to the other end. This might be the cause of the plateau observed in Figure 23 for longer SWCNTs reached after a certain field magnitude. Shorter nanotubes on the other hand are expected to have more gradual photoluminescence decrease due to lower numbers of quenchers and the proximity of SWCNT ends.

2.3.5 Diameter and type dependence

The study of the diameter dependence of carbon nanotube photoluminescence quenching was conducted in bulk with thick PMMA/SWCNT films between ITO electrodes. The benefits of bulk photoluminescence measurements were that both the angle and length dependences averaged out due to the large number of carbon nanotubes of various lengths and orientations in the sample. In addition to that, bulk spectroscopic measurements allowed observing the effects of electric field on the whole range of different nanotube (n,m) types at once (Figure 24).

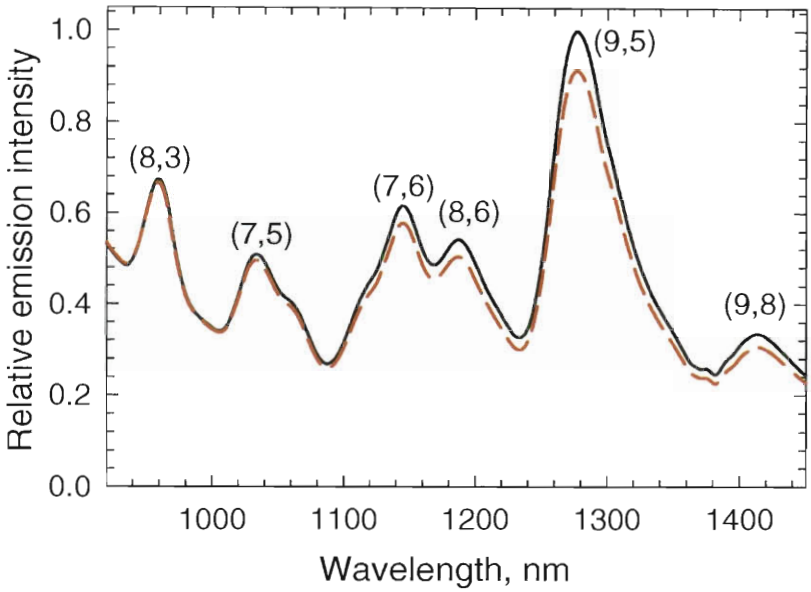

Figure 24. Bulk SWCNT sample photoluminescence spectra taken with 660 nm laser excitation. Solid curve – spectrum with no field applied. Dashed curve – spectrum of the carbon nanotube in an electric field of 2.27 V/μm.

As seen from Figure 24, carbon nanotube peaks display different quenching at a field of 2.27 V/μm. Peaks at the lower emission wavelength ((8,3) and (7,5)) experience almost no quenching at all, whereas the ones at the longer wavelengths, corresponding to emission from (7,6), (8,6) and (9,5) nanotubes, are quenched significantly. Thus, Figure 24 implies that carbon nanotubes with longer emission wavelength and, therefore, of greater diameter,[101] experience more quenching in the electric field. This assumption was tested by measuring photoluminescence quenching for 12 carbon nanotube species at the field of 2.27 V/μm and plotting the quenching amplitude versus diameter of SWCNTs (Figure 24). Quenching measurements for each photoluminescence peak corresponding to a particular nanotube type were conducted separately using appropriate excitation

wavelengths.

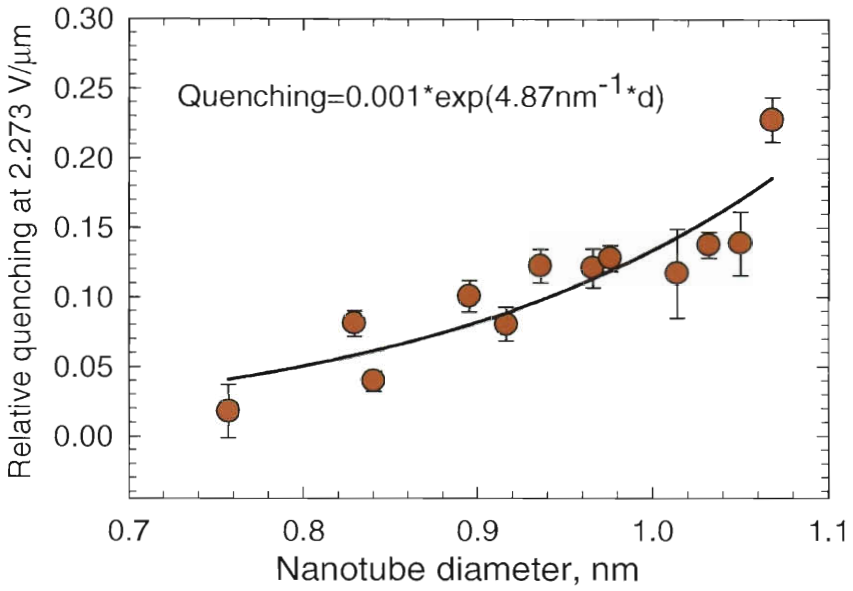

Figure 25. Photoluminescence quenching as a function of SWCNT diameter.

Figure 25 shows that the relative quenching of carbon nanotube photoluminescence depends nearly exponentially on the diameter of the nanotube. Such a strong dependence indicates that SWCNT diameter has a great influence on the photoluminescence quenching process.

This matter was studied further to obtain the information about the nature of diameter dependence. First, the photoluminescence intensity was recorded at several voltages for one particular spectral peak corresponding to the emission from (9,5) nanotubes (Figure 26).

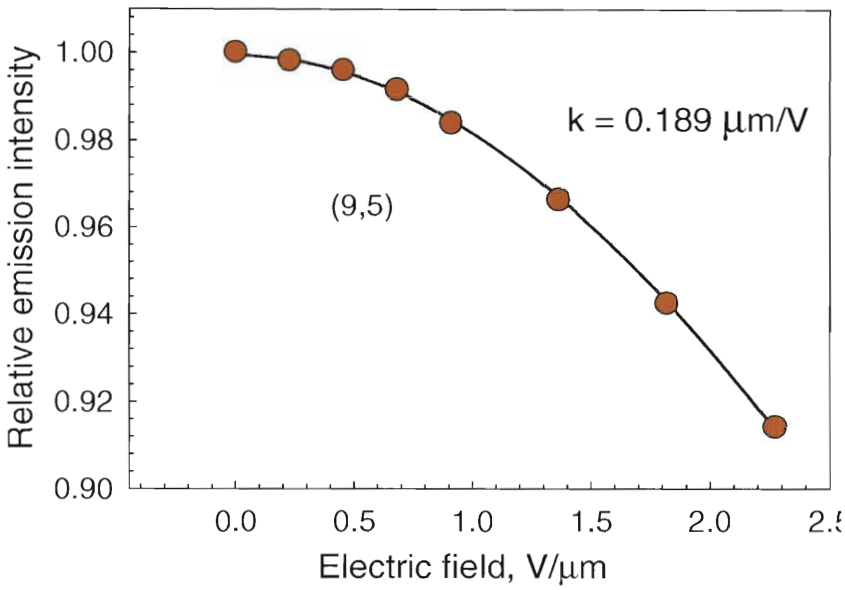

Figure 26. Photoluminescence quenching of (9,5) SWCNT spectral feature.

The best fit for the quenching curve in Figure 26 also appears to be a single-parameter inverse hyperbolic cosine function with quenching parameter k = 0.189 μm/V. This fit is similar to the one in Figure 17 and the only major difference is that in Figure 17 a wider field range was used. However, if in Figure 17, we zoom in on the part between 0 and 2.5 V/μm, the fit would closely resemble one in Figure 26. That resemblance together with the simplicity of the fit involved suggests that inverse hyperbolic cosine provides a successful model of carbon nanotube photoluminescence quenching curves for the bulk samples and for individual nanotubes.

Later on, quenching curves were measured for several other types of SWCNTs (Figure 27) using selected excitation wavelengths specific for each SWCNT type and a monochromated lamp as an excitation source. Five nanotube photoluminescence peaks were sampled.

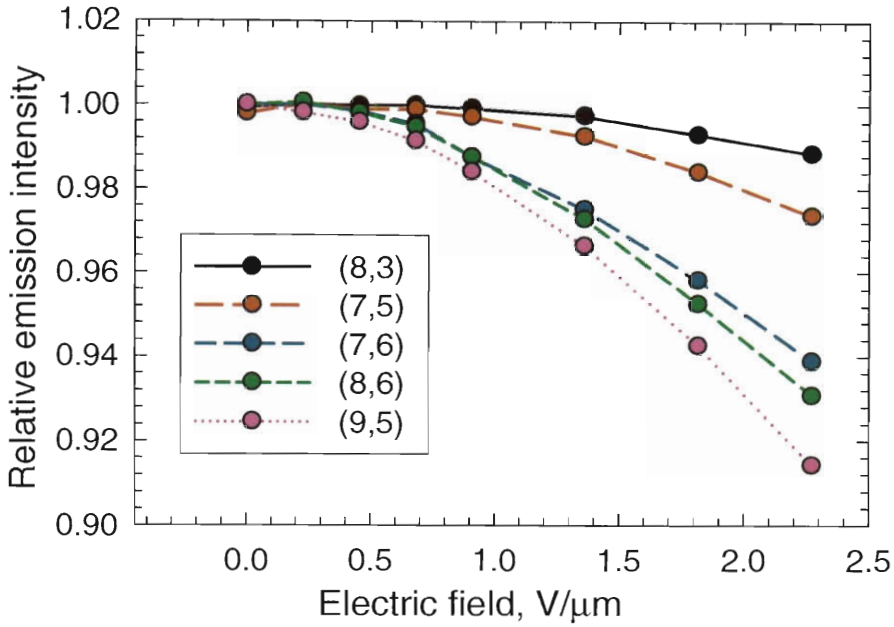

Figure 27. Quenching curves for five different SWCNT types, lamp excitation. For these curves error bars are usually smaller then the point size.

Figure 27 shows again that the strongest quenching, reflected by the steepness of the quenching curves, was observed for larger diameter (9,5) and (8,6) nanotubes. These curves were fit with inverse hyperbolic cosine and the quenching coefficient for each of them was recorded. As a result, quenching coefficients for several types of nanotubes were plotted versus diameters of those nanotube species (Figure 28). This analysis is more exact then the one reported in Figure 25 since in this case we monitored photoluminescence quenching at several values of the electric field, whereas previously (Figure 25) a relative quenching was recorded at just one point (2.27 V/μm).

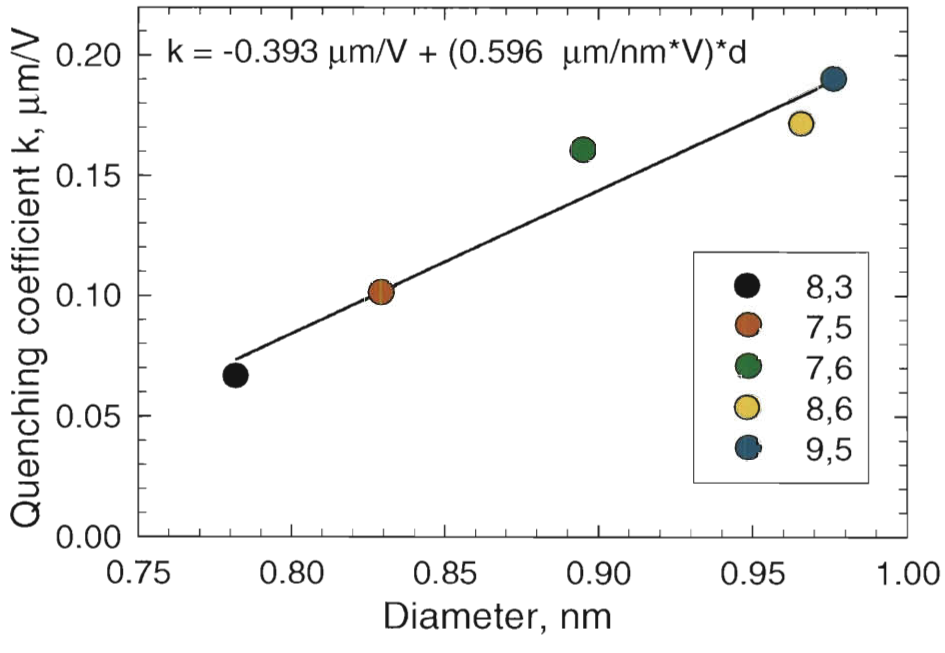

Figure 28. SWCNT diameter dependence of the quenching coefficient.

Figure 28 shows that photoluminescence quenching efficiency depends linearly on the diameter of the nanotubes. Using the E_{11} values tabulated for different SWCNT species,[101] we also find that the quenching coefficient has a linear dependence on E_{11} transition energy of different SWCNT types (Figure 27). This graph ties the nature of the quenching process with electronic structure of carbon nanotubes.

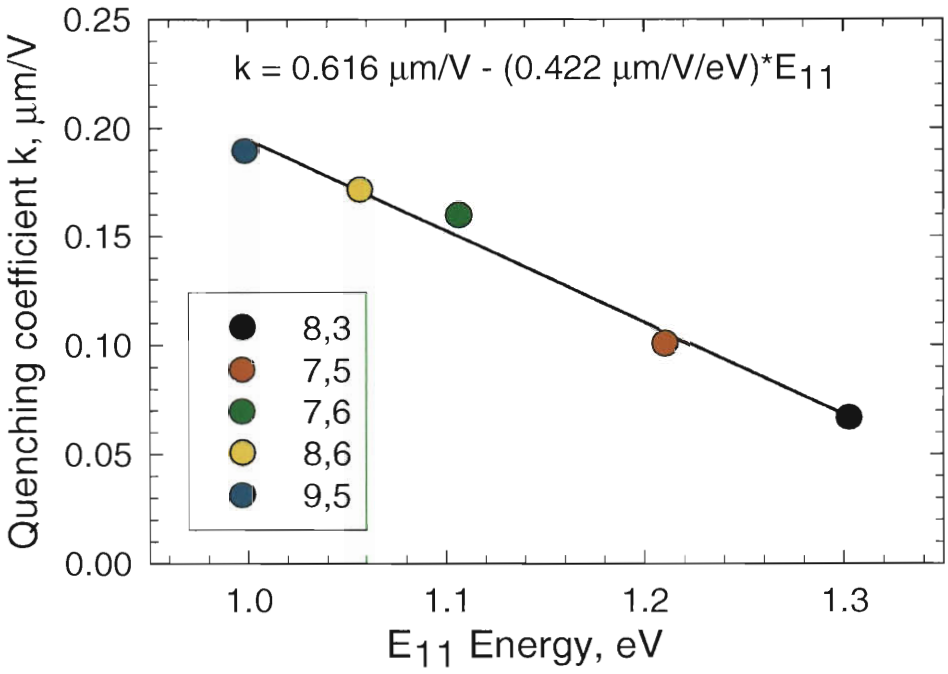

Figure 29. Dependence of the quenching coefficient on E_{11} transition energy.

We note that diameter dependence of quenching coefficient depicted in Figure 28 may also serve as a means of relating electric field-induced photoluminescence quenching to excitonic effects. Exciton binding energy can be found from the model described above as the depth of the potential well (Figure 18). It depends on several modeling parameters including SWCNT diameter, d. After calculating binding energies for several possible values of d, we have plotted the model's dependence of exciton binding energy on the nanotube diameter (Figure 30).

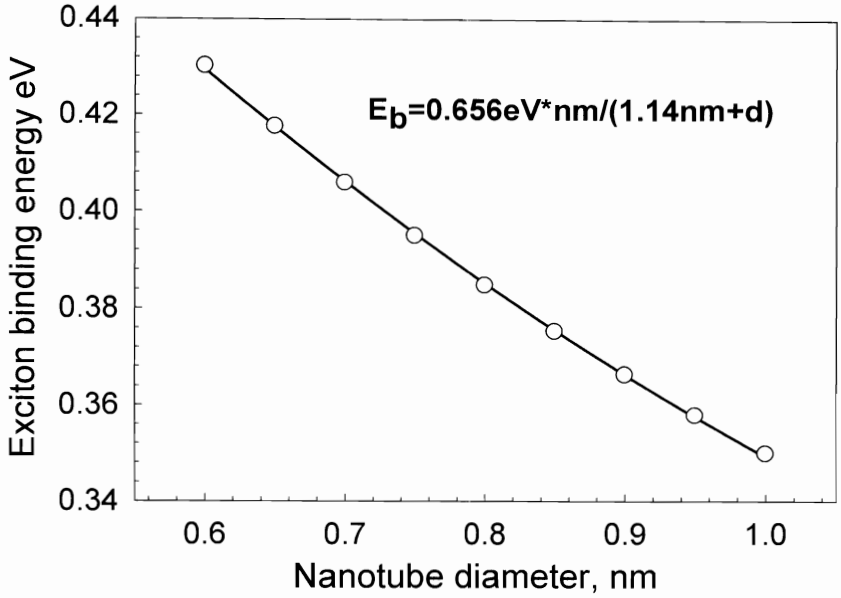

Figure 30. Dependence of calculated exciton binding energy on SWCNT diameter.

According to Figure 30, exciton binding energy is inversely proportional to SWCNT diameter, as has also been deduced in more rigorous theoretical models.[102,103] That result is important with regard to this work, since electric field photoluminescence quenching coefficients were experimentally found to be linearly proportional to the diameter of the nanotube (Figure 28). That suggests that the quenching coefficient is inversely proportional to exciton binding energy. This finding supports the exciton dissociation model, according to which the stronger the exciton is bound, the smaller would be the probability of pulling it apart. Furthermore, if the interpolation equations on both Figure 30 and Figure 28 are combined, the resulting formula (Eq. 9) may show an approximate relation between quenching coefficient k and exciton binding energy.

$$E_b \approx \frac{0.39 \frac{eV \cdot \mu m}{V}}{1.1 \frac{\mu m}{V} + k} \quad \text{(Eq. 4)}$$

This formula can be further refined by conducting a series of quenching experiments complemented by more advanced quantum mechanical modeling to provide an important experimental route to exciton binding energies.

2.3.6 In-depth study of carbon nanotube photoluminescence quenching process and electric field-induced spectral shifts

Even though a couple of possible quenching mechanisms were proposed above, some details of the quenching process are still unclear. For example, it is not known at which stage of the photoluminescence process the quenching is most likely to occur. It can happen while the excitonic electron resides in either c_1 or c_2 conduction sub-bands (Figure 6). To clarify this issue, a series of experiments were conducted with bulk SWCNT/PMMA films. Two diode lasers with wavelengths of 660 and 980 nm were used to selectively excite (8,6) carbon nanotubes on E_{22} and E_{11} transitions respectively. For the E_{11} excitation, (8,6) SWCNTs were excited through the phonon resonance, 1600 cm^{-1} above the E_{11} emission peak to avoid the interference from scattered excitation light. Figure 6 shows that if E_{11} excitation is used, the electron is promoted directly to c_1, whereas in the case of E_{22} excitation, it first enters the c_2 sub-band and then non-radiatively relaxes to c_1. Therefore, if the majority of the photoluminescence quenching occurs in c_1, the quenching curve obtained with E_{11} excitation would look just like the one for E_{22} excitation. On the other hand, if the quenching process happens mostly in the c_2 sub-band, the photoluminescence quenching should be much less with E_{11} excitation

than with E_{22} excitation. The analyses of carbon nanotube photoluminescence peaks recorded using the Spex Fluorolog 3 instrument showed that quenching curves for E_{22} and E_{11} excitation exhibit similar behavior and their quenching coefficients are also close (Figure 31). The 20% difference between k values suggests that a minor field induced quenching process may occur only for c_2 sub-band excitation. The major part of the photoluminescence quenching, though, is carried out in c_1. That result is quite reasonable considering that the lifetime of the c_2 sub-band electron is several orders of magnitude less then the lifetime in c_1.

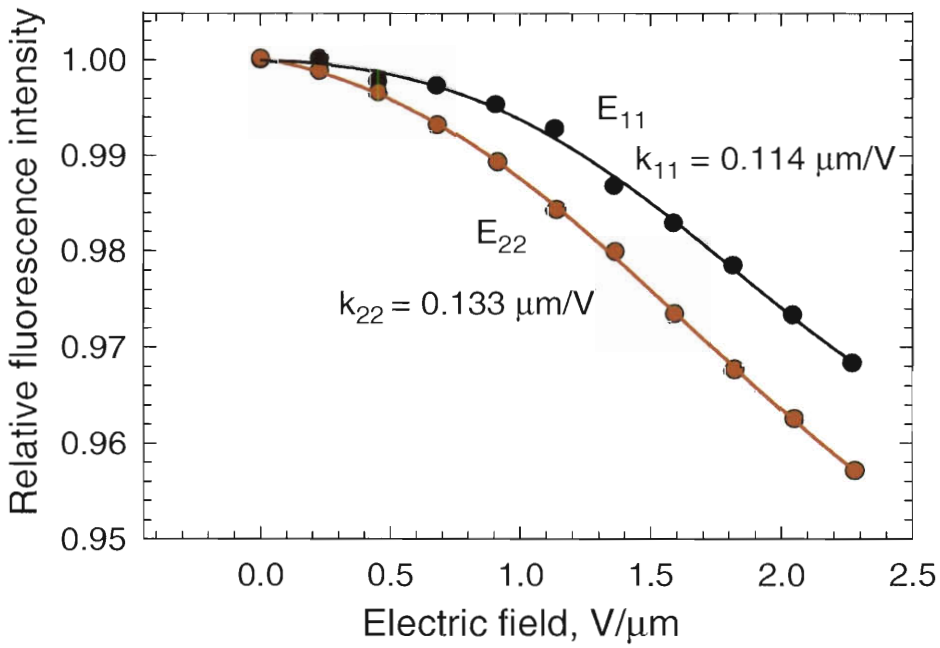

Figure 31. Quenching curves for E_{11} and E_{22} laser excitation of (8,6) nanotube.

One of the side goals of our experiments was to test prior theoretical predictions[92,93,95,96] that a transverse electric field would influence the electronic structure of a nanotube and thereby produce spectral shifts in carbon nanotube emission spectra.

We explored such a possibility and at times observed red spectral shifts on the order of several nanometers in single nanotube (Figure 32). However, these shifts were not as large as predicted.[92,93,95,96] In addition, even though the intensity of the emission peak decreased due to the photoluminescence quenching, its position as determined by peak fitting some times did not change (Figure 33) or changed randomly.

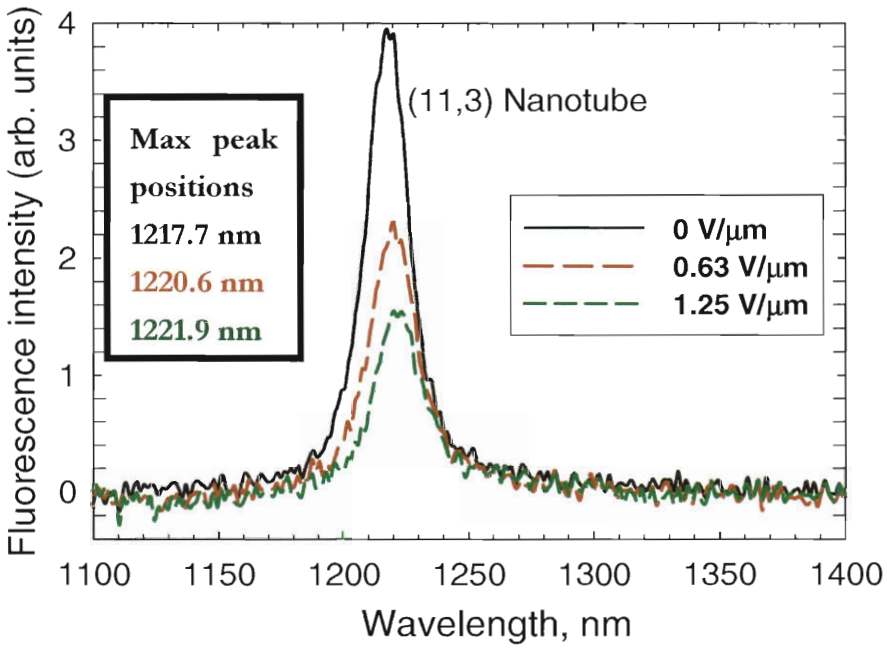

Figure 32. Photoluminescence spectra of an individual nanotube in the electric field.

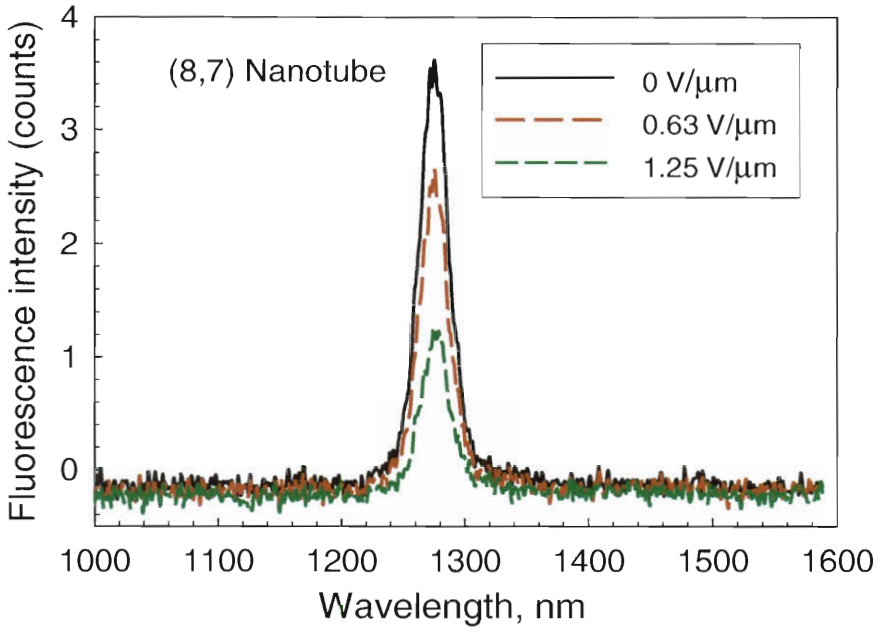

Figure 33. Photoluminescence spectra of an individual nanotube in the electric field - no shift observed.

Such irregular behavior could be explained by the fact that the fields predicted to induce substantial spectral shifts[92,93,95,96] were significantly greater then the ones used in our experiments. Thus, it is possible that due to limited electric field strengths, the effect was small compared to our experimental uncertainties. We propose that these spectral shifts might be observed more clearly at substantially higher fields, which could not be achieved in our experimental setting due to breakdowns.

2.4. Summary

In a series of experiments designed to detect possible variations in the photophysical properties of carbon nanotubes induced by external electric fields, carbon nanotube photoluminescence quenching was observed. The effect is clear and reproducible. At first, the photoluminescence intensity of carbon nanotubes in polymers was found to decrease reversibly with the electric field. A thorough investigation showed that the photoluminescence quenching follows an inverse hyperbolic cosine pattern characterized by a single quenching parameter that reflects the steepness of the quenching curve and, therefore, the susceptibility of SWCNTs to electric field quenching.

It was experimentally determined that electric field photoluminescence quenching in carbon nanotubes depends on the angle between the nanotube axis and the electric field. Within experimental uncertainty, the quenching coefficient varied as a cosine of that angle for a number of individual nanotubes. Length of carbon nanotubes was also found to be an important factor influencing field-induced photoluminescence quenching. It was discovered that long carbon nanotubes experience strong quenching at low voltages and then reach a certain saturation level where the photoluminescence intensity is nearly constant.

In addition, a strong diameter dependence of carbon nanotube photoluminescence quenching was detected. We found that SWCNTs of larger diameters experienced stronger quenching than the ones with smaller diameters and higher transition energies. A simple theoretical model was used to correlate this effect with variations in exciton binding energy among different (n,m) types.

Potential future research on this topic may include investigating temperature and

pH effects on electric field photoluminescence quenching. Since non-radiative decay processes are temperature-dependent, these studies may reveal how the photoluminescence quenching depends on the non-radiative decay rate.

The effect of carbon nanotube photoluminescence quenching can be applied in several areas of industry and science such as semiconductor electronics and in any general device utilizing carbon nanotube photoluminescence. For example, the dependence of SWCNT photoluminescence on applied electric field could be used to modulate photoluminescence emission from individual carbon nanotubes in nanoelectronic semiconductor photodevices. In addition, this effect suggests using SWCNTs as microscopic sensors of electric fields.

CHAPTER 3

Quantifying the semiconducting fraction in single-walled carbon nanotube samples[79]

3.1 Introduction

Much of the interest in single-walled carbon nanotubes arises from their outstanding physical, optical and electronic properties, which include both semiconducting and metallic structural forms.[18] In a number of possible applications of SWCNTs, such as field emission sources[52], nanoscale electrical interconnects,[53] field-effect transistors,[54-56] and conductive transparent films,[104,105] nanotubes of only a single electronic type are needed. Such select samples can be obtained through controlled growth or post-production sorting.

Most of the growth processes such as HiPCO, arc discharge, laser ablation and regular CVD have been shown before to produce polydisperse SWCNT samples with different amounts of metallic and semiconducting SWCNTs. Some of the methods, though, were refined to yield SWCNT batches limited by chirality (lower temperature CoMoCAT SG[24,25] synthesis) or by electronic type (pre-conditioned CVD growth[106]). Although such advanced growth methods are strongly selective, many applications require samples that have undergone even more rigorous structure and electronic type sorting. That may be achieved by several post-growth processing methods such as density gradient ultracentrifugation (DGU) or DNA-assisted ion exchange chromatography.[27-29,31,32,107]

It is also highly important to have a well-characterized starting nanotube material for a number of applications described above. The composition and the yield of the

electronic type enrichment processes can be assessed using several scientific tools. At the level of individual nanotubes, the metallic and semiconducting SWCNTs can be distinguished and counted by specific (n,m) determination through highly resolved scanning tunneling microscopy (STM)[17] or electron nanodiffraction.[108,109] However, these precise microscopic methods involve complex analyses and are too laborious for routine use. The metallic/semiconducting composition of a sample can also in principle be found by counting individual nanotubes using voltage-contrast SEM, which distinguishes metallic from semiconducting SWCNTs.[110] We note that this approach involves the complexity of size exclusion chromatography followed by electrophoretic SWCNT deposition. In addition, systematic errors may arise from nonuniform sampling or the presence of small bundles of mixed electronic type. Additional complications may also be caused by charging SWCNTs with electron beam. Another SWCNT counting method is based on direct charge transport or electrical breakdown measurements on SWCNT field-effect transistors that classify nanotubes as metallic or semiconducting.[111,112] The laborious nature of this approach makes it difficult to achieve high statistical accuracy. Results may also be influenced by clustering and sampling inefficiency in addition to difficulties in characterizing SWCNTs with a significant number of conductivity-affecting defects. Photoluminescence spectroscopy offers an incisive probe of bulk or individual semiconducting SWCNTs,[20,98,113] but does not detect metallic species. Raman spectroscopy also provides a relatively rapid tool for studying SWCNTs as individuals or bulk ensembles.[114,115] However, it has the disadvantage of requiring a wide variety of incident laser wavelengths to detect nanotubes spanning a range of structures. Raman has been used to estimate the relative semiconducting and metallic contents in processed

SWCNT samples,[28,116,117] but the calibration factors needed to extract reliable values of this ratio are not known either for G^+ or G^- bands or for radial breathing mode peaks. Visible-near-IR absorption spectroscopy of SWCNT samples reveals distinct optical transitions of semiconducting and metallic species.[61,118] It appears more promising for quantitative determination of metallic/semiconducting ratios, if adequate and consistent calibration methods become available. Recent reports show progress in that area but some challenges remain in accurately subtracting background absorptions and acquiring well-characterized reference samples.[111,119,120] Further research directed towards determining the sources of absorption background and diminishing those would increase the capability of absorption spectroscopy as the tool for assessing SWCNT sample electronic type composition. In addition, a reference SWCNT sample with known semiconducting fraction would have to be used to calibrate absorption peaks.

In view of the problems in the assessment of electronic composition we introduce a new counting-based method for the absolute measurement of semiconducting fractions in SWCNT samples. In this approach, AFM and near-IR photoluminescence are used to image dried dilute SWCNT dispersions. Both semiconducting and metallic species are visible in the AFM images, while only semiconducting nanotubes appear in photoluminescence. The ratio of observed nanotube surface densities therefore gives the semiconducting fraction in the sample. This analysis was performed on a variety of SWCNT batches prepared by different growth methods and/or sorted using DGU. The results provide compositional reference data that should be useful in the electronic-type specific applications of SWCNTs or for the calibration of bulk analysis methods.

3.2 Experimental

3.2.1 SWCNT material for the assessment of semiconducting fraction

Several SWCNT batches produced by different methods were studied in this work. These included raw product made by the HiPco method at Rice University (batch 166.12), by a CVD process at the Honda Research Institute USA Inc. (Columbus, Ohio), by laser ablation at NASA-Johnson Space Center, and by the University of Oklahoma CoMoCAT method at SouthWest Nanotechnologies Inc. The CoMoCAT samples were purified and freeze-dried before analysis. Those included commercial grade (CG) samples produced at higher temperatures and standard grade (SG) SWCNTs grown at low temperatures. We also analyzed SWCNTs that had been processed by density gradient ultracentrifugation at Northwestern University starting from raw HiPco SWCNTs (Carbon Nanotechnologies, Inc., batch R0559). Those samples consisted of metallic-enriched, semiconducting-enriched and the initial HiPco SWCNT material.

3.2.2 Sample preparation

Raw SWCNT samples were initially bath sonicated for 3 h in 1% aqueous sodium dodecyl sulfate (SDS) solutions to obtain concentrated SWCNT suspensions. Those were further centrifuged at 26700 × g for 6 h to remove large aggregates. To avoid excessive losses, the smaller CVD and laser ablation samples were centrifuged at 14500 × g for 10 to 30 min in a table-top centrifuge. After centrifuging, the pellets were discarded and the supernatants were diluted by factors of 14 to 24, depending on the sample, to adjust SWCNT and SDS concentrations to convenient levels. Diluted suspensions were further tip-sonicated for 2 min at 5 to 7 W to disaggregate residual SWCNT bundles. Resulting

material was then spin-coated onto polished fused silica slides. This substrate was intentionally chosen for its flat surface and transparency allowing photoluminescence to pass through the slide to the objective of the inverted microscope. The slides we pre-conditioned by spin-coating with 0.05% aqueous SDS solution, thoroughly rinsing with deionized water, and annealing for 30 minutes in air at 550 °C. This cleaning procedure was intended to wash off larger dust particles and then burn the smaller organic contaminants accumulated on the slide. As a result, cleaned slides had exceedingly even surface yielding higher quality AFM images. In addition to cleaning, reducing surfactant concentration has strongly decreased the amount of dry SDS clusters on a sample surface and therefore also facilitated clear AFM imaging. The sample preparation procedure for DGU-processed SWCNTs was quite different due to the form and composition in which those samples were supplied. Sorted SWCNTs were extracted from the density gradient in suspensions containing SDS, sodium cholate, and iodixanol[35] and further concentrated in step density gradients. To prevent uneven AFM backgrounds arising from highly concentrated sodium cholate and iodixanol aggregates, the samples were dialyzed into 1% w/v SDS aqueous solution for 49 h using 20k molecular-weight cutoff dialysis cassettes (Pierce Chemical), which removed the sodium cholate and iodixanol from solution. The extent of the dialysis was monitored using photoluminescence spectra of dialyzed fractions. Since spectral peak positions of SWCNTs in different surfactants vary depending on the surfactant structure[121], it was possible to observe a shift (Figure 34) between the spectra of the initial and dialyzed samples as sodium cholate left SWCNT surface and was substituted by SDS. Furthermore, SWCNT photoluminescence peak positions after dialysis corresponded to the ones of SDS-dispersed SWCNTs.

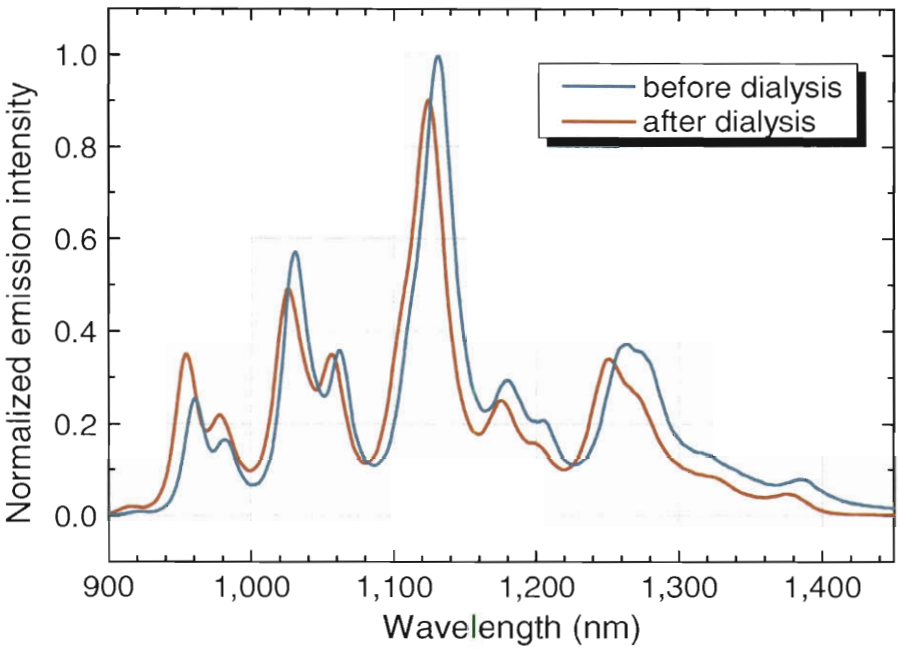

Figure 34. Photoluminescence spectra of semiconducting-enriched SWCNT sample before and after dialysis.

Dialyzed suspensions were diluted by factors of 14 to 24 and subjected to intense bath sonication (Sharpertek ultrasonic cleaner). Resulting samples were then tip-sonicated for 30 s at 5 W and spin-coated onto 15 × 15 × 0.15 mm mica slides. Mica slides provided high quality flat substrates for AFM, and were transparent enough for successful photoluminescence imaging.

3.2.3 Measurements

The total number of SWCNTs per unit area was determined from AFM images, and the number of semiconducting SWCNTs per unit area was found from near-IR photoluminescence images. A Veeco AFM (Multimode 3A) was used to study up to 40 regions, each 10 × 10 μm or 6 × 6 μm (for DGU sorted samples), within a ~100 × 100 μm

area of the sample. The number of SWCNTs in each image was counted (Figure 35) and the average nanotube density per unit area was calculated. Photoluminescence of individual semiconducting SWCNTs on the sample surface was observed using a custom built near-IR fluorescence microscope (Figure 12). In this setup, semiconducting SWCNTs were excited in their E_{22} transitions with 660 and 780 nm diode lasers. The combination of these excitation wavelengths was in our experience sufficient to induce detectable emission from essentially all semiconducting (n,m) species in the studied samples. Few off-resonance SWCNT species will still be excited but with slightly less efficiency decreasing the photoluminescence intensity. Near-IR E_{11} photoluminescence emission from SWCNTs on the substrate was collected through the quartz or mica substrate by a Nikon Plan Apo 60×, NA= 1 water immersion objective or a Nikon CF Plan 100×, NA=0.95 air objective of a Nikon TE-2000U inverted microscope (Figure 12).[98] The microscope was coupled through a 946 nm long-pass filter to a liquid nitrogen-cooled Roper OMA V 2D InGaAs camera used to image NIR emission from semiconducting SWCNTs on the sample surface (Figure 36). Spectra of individual SWCNTs were collected by directing the emitted light from a small region of the image plane into a spectrograph with a nitrogen-cooled 512-channel InGaAs linear array detector. In each photoluminescence image, several areas of 10 × 10 μm or 6 × 6 μm (depending on the magnification of the objective) were examined to find the number of semiconducting SWCNTs per unit area. Since the resolution of photoluminescence images is 10 times less than the lateral resolution of AFM, the former had to be thoroughly examined in order to resolve SWCNTs that might be close to each other. Low SWCNT concentrations achieved by diluting suspensions prior to deposition decreased

that risk significantly. From AFM and photoluminescence image analyses, the semiconducting fraction in each sample was found as the ratio of the number of semiconducting SWCNTs per unit area to the total number of SWCNTs per unit area. Replicate measurements were made on the same SWCNT batch to obtain the average semiconducting fraction and the statistical error of the mean.

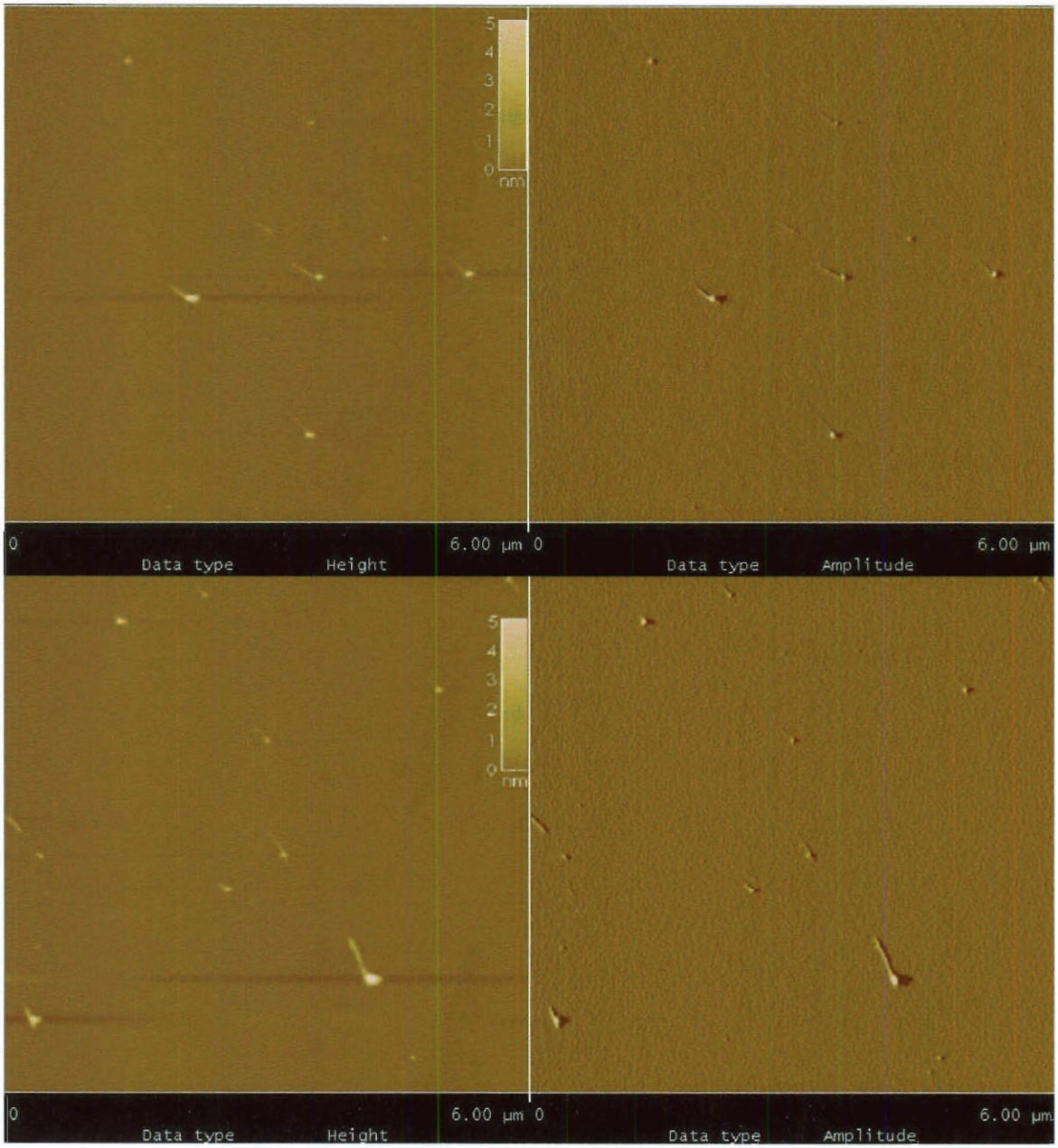

Figure 35. Tapping mode AFM images of individual SWCNTs from DGU-processed semiconducting-enriched sample in dried SDS on a cleaved mica surface. Amplitude image is shown in the right panels; height is shown in the left panels. Each panel shows a 6×6 µm region.

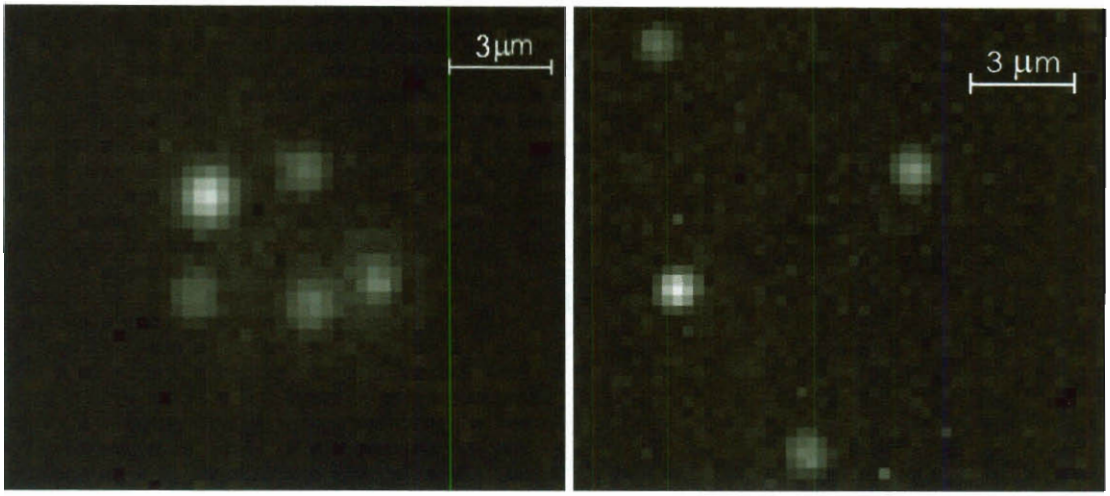

Figure 36 -Near-IR photoluminescence images of individual SWCNTs from the same DGU-processed semiconducting-enriched sample in dried SDS on a cleaved mica surface.

3.3 Results

3.3.1 Potential error estimates

In our experiments only individual, disaggregated SWCNTs were counted. During AFM studies the few residual bundles were identified on the basis of height profiling and omitted from the counts. The histogram in Figure 37 shows the height distribution recorded from SWCNT samples used in this work. The left lobe of this bimodal distribution represents SWCNTs of diameters less than 1.5 nm that were identified as individual SWCNTs, whereas the right lobe that includes larger features is attributed to nanotube bundles. The bundle features larger than 1.7 nm in diameter, therefore, were not included in the counting process.

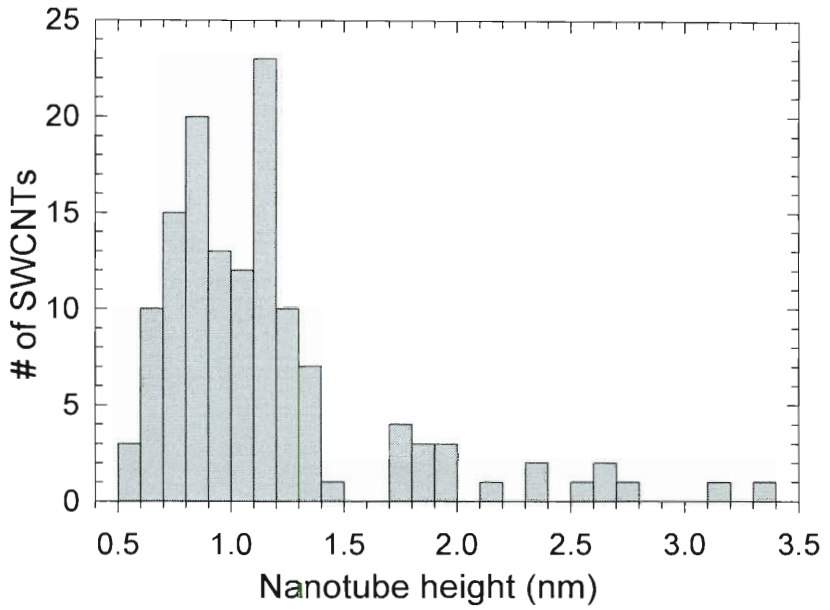

Figure 37. SWCNT height distribution histogram constructed from AFM measurements of four different sample batches.

Although SWCNTs on the substrate were mostly covered by a layer of dry surfactant, the height measurements were preferentially made at the points along the nanotube where surfactant coating appeared to be absent or minimal, providing a realistic SWCNT diameter estimate. From this histogram and a general knowledge about the samples used in this work, we infer that individual SWCNTs counted in this work had small enough diameters to exhibit photoluminescence emission within the spectral range of our InGaAs detector.

As seen from Figure 35, SWCNT features in 6 x 6 μm regions could be easily counted and their heights found from height profile analysis. SWCNT profile heights in Figure 35 measured at the regions with minimal or no surfactant ranged from 0.7 nm to 1.35 nm, consistent with the diameter distribution of SWCNTs in our samples and

smaller than would be expected for bundled nanotubes.

As mentioned before, the photoluminescence images having far coarser spatial resolution than AFM, may not distinguish individual nanotubes from bundles or loose aggregates. To avoid counting those, we examined the emission spectra of objects that appeared not to be point emitters and excluded them if their spectra were broader or more complex than expected for an individual SWCNT (see Figures 38a and b for examples of single Lorentzian emission spectra of individual SWCNTs studied in this work). Bundles in samples containing significant metallic content are likely to be nonemissive, and hence uncounted, because of efficient energy transfer to metallic SWCNT, that quenches photoluminescence.[64] However, there is the possibility that our method may not distinguish small semiconducting bundles in photoluminescence that were recognized and omitted in AFM. To estimate the possible error arising from such occurrences, we have examined diameter distributions in a number of samples. These distributions show that the fraction of nanotube objects appearing to be bundles in AFM images ranges from 5 to 15% (Figure 37), with semiconducting-rich samples falling near the bottom of this range. That leaves a minor chance of encountering purely semiconducting bundles and decreases the significance of that source of error.

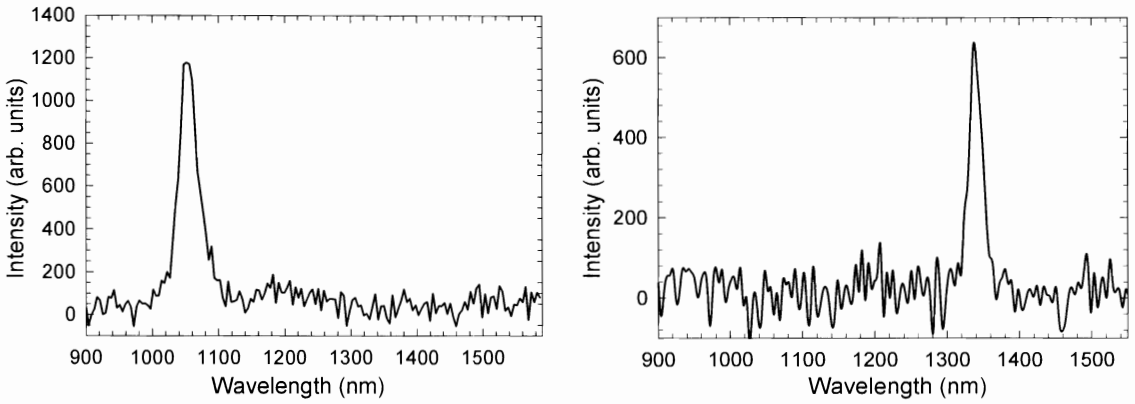

Figure 38. Near-IR photoluminescence spectra of single SWCNTs in dried SDS on a fused silica substrate.

Due to intense ultrasonication used to disaggregate SWCNTs, some of them could be shortened or damaged, which would create photoluminescence quenching centers along the nanotube surface (charge-induced quenching process described in previous chapter). In that case, most undamaged areas of the nanotubes would still be expected to emit. The detection limits for SWCNT emission in the apparatus described above are low enough to observe SWCNTs with emitting segments of 100 nm and higher. In the unlikely event of damaging large areas of the nanotube, such semiconducting SWCNTs would be non-emissive and contribute to the statistical error in this experiment. The significance of that error might be reduced by a larger sampling. SWCNTs cut into segments shorter than 100 nm could also introduce additional uncertainty. However, according to AFM SWCNT length analysis preformed on a fraction of SWCNTs in each batch, the vast majority of nanotubes in our sample are distributed between 200 and 700 nm in length.

Another possible error source arises from the fact that we do not image exactly

the same sample regions in AFM and photoluminescence. There is a possibility that different small regions of the same slide studied with AFM and photoluminescence microscopy may have different surface densities of SWCNTs. This lack of image registration can contribute uncertainty to the measured semiconducting percentage for a particular small region. To decrease that uncertainty we collected the data from many equivalent regions across the sample surface and found an average SWCNT surface density. Given a random distribution of SWCNTs on a slide surface, that should statistically approach the outcome of registering AFM and PL in exactly same areas.

Typically at least 40 different areas, each 10 × 10 μm or 6 × 6 μm (for DGU sorted samples), were studied for every sample batch, giving a nanotube count exceeding 200 in AFM and 400 in photoluminescence measurements. The total number of SWCNTs counted in this work exceeds 12000. The measurements for each batch were divided among a number of spin-coated replicates prepared from each sample batch to further decrease the errors associated with uneven sample surface coverage. The semiconducting percentages were found for each replicate and averaged to obtain statistical estimates of the semiconducting fraction (Table 1). The standard error of the mean was calculated, ranging from 0.4 to 4%.

Table 1. Compositions determined for as-produced or processed SWCNT samples.

Sample	Source	% semiconducting	% metallic	% standard error
HiPco	Rice Univ.	62.9	37.1	0.5
CoMoCAT, standard grade	SWeNT Inc.	92.1	7.9	1.1
CoMoCAT, commercial grade	SWeNT Inc.	51.9	48.1	3.5
Laser ablation, low T method	ERC Inc/NASA-JSC	54.7	45.3	1.4
CVD preferential growth	Honda Res. Inst.	15.4	84.6	2.6
HiPco, starting material	Northwestern Univ.	60.5	39.5	3.8
HiPco, semicond.-enriched by DGU	Northwestern Univ.	96.0	4.0	0.6
HiPco, metallic-enriched by DGU	Northwestern Univ.	3.1	96.9	0.6

3.3.2 Assessment of semiconducting fraction

The results in Table 1 generally seem consistent with expectations based on the growth and processing methods used to prepare the samples. For example, HiPco SWCNTs are known to grow in a wide variety of smaller diameter (n,m) structures and are presumed to exhibit a nearly statistical distribution of 2/3 semiconducting and 1/3 metallic SWCNTs. Our results (Table 1) show a HiPco semiconducting content within 4 % of that expected value. The standard grade CoMoCAT SWCNTs produced by a lower temperature process are expected to contain large amounts of the semiconducting (6,5) and (7,6) species[77] and, therefore, a high semiconducting content above statistical 66%. As anticipated, our findings (Table 1) indicate a large semiconducting fraction of 92.1% in standard grade CoMoCAT samples.

The expectations of a large semiconducting fraction in these samples arise from the growth mechanism. Recently it has been proposed that the formation of caps leading

to zig-zag nanotubes is thermodynamically and kinetically unfavorable for smaller diameter SWCNTs.[122] The armchair and near-armchair caps are considered much more stable; however, the activation energies for incorporating carbon atoms into the nanotube in the growth process are high for armchair SWCNTs. Therefore, at low temperatures when there is not enough energy to overcome the activation barrier, the conditions are more favourable for the growth of near-armchair (e.g., (6,5), (7,6), etc.) semiconducting SWCNTs that are somewhat less stable, but allow carbon incorporation with a lower activation energy. Activation energy differences between armchair and near-armchair SWCNTs are expected to be greatest in the small-diameter region, narrowing the distribution of chiralities obtained in low-temperature synthesis and yielding samples highly enriched in small-diameter near-armchair semiconducting SWCNTs.[123] The commercial grade CoMoCAT sample, produced at higher temperatures, is then expected to have a broader range of SWCNT chiralities with a fair portion of armchair metallic SWCNTs present. According to our counting-based analysis, it was found to contain a greater than statistical metallic fraction of 48% with only 52% semiconducting SWCNTs.

Even though CoMoCAT commercial grade synthesis produced a higher than statistical percentage of metallic SWCNTs, it was shown possible to tune a CVD growth process for even higher metallic contents. This was illustrated by the samples from Honda Research Institute USA Inc., that were grown at 860 ^{o}C via methane decomposition on Fe nanocatalysts. Those were preprocessed by annealing in situ in a He ambient containing H_2 / H_2O species. Our counting analysis found this product to contain 15% semiconducting, and therefore 85% metallic SWCNTs. This semiconducting fraction is considerably lower than the one found in the other CVD samples analyzed

here (CoMoCAT SWCNTs), which reveals an important advance in electronic type-specific CVD SWCNT growth. In addition, this appears to be the lowest semiconducting fraction found among the samples that had not undergone post-growth separation treatments. Our analysis is consistent with an independent estimate of the semiconducting content obtained by analyzing ratios of integrated Raman radial breathing mode intensities (with a 632.8 nm excitation wavelength) and comparing to a HiPco standard.[124] This approach suggests a semiconducting fraction of ~20%. Even though that Raman characterization method lacks multi-wavelength analysis that would detect a wider range of SWCNT chiralities, it still provides a crude estimate of the electronic composition confirming the validity of our findings.

In addition to HiPco and CVD grown SWCNTs, we have also analyzed samples produced by laser ablation method at the NASA-Johnson Space Center.[125-128] The synthesis was carried out at lower temperatures of 900 ^{o}C (as opposed to more common 1200 ^{o}C) in order to reduce the average diameter and bring SWCNT E_{11} transitions into the detectable range of our spectrometer.[129] This laser ablation sample was found to contain 55% semiconducting nanotubes.

In order to further test our method and characterize the semiconducting fraction in more refined SWCNT samples with known large excesses of semiconducting or metallic nanotubes, we have analyzed SWCNT batches prepared at Northwestern University. These consisted of fractionated HiPco nanotubes enriched in semiconducting or metallic SWCNTs. The semiconducting fraction was found for starting material as well as in the enriched samples. The starting material showed semiconducting content of 60.5%, close the value determined separately for HiPco SWCNTs (Table 1). The metallic and

semiconducting-enriched samples differed dramatically from the starting material, with semiconducting fractions of 2.6% and 96%, respectively (Table 1). These results indicate a successful highly selective electronic type DGU sorting and agree with crude purity estimates found by optical absorbance alanyses.[35] More detailed statistics regarding the measurements presented in this work may be found in Table 2.

Table 2. Detailed statistical data describing counting determinations of SWCNT semiconducting fractions

	HiPco	CoMoCAT SG	CoMoCAT CG	Laser ablation	CVD	HiPco DGU starting	HiPco DGU SC-enriched	HiPco DGU M-enriched
SWCNTs counted in AFM	223	227	645	591	328	378	395	1117
AFM area scanned, μm^2	2200	12600	4600	4200	4100	2600	3600	5100
SWCNTs counted in PL	1363	1347	1104	1100	686	2099	708	427
PL area scanned, μm^2	22800	41200	16400	14100	53900	25400	7300	3800
Percent SC, sample 1	62.5	90.0	49.0	54.9	19.2	60.5	97.3	2.6
Percent SC, sample 2	62.4	93.2	48.0	52.2	16.6	53.9	96.8	3.8
Percent SC, sample 3	63.9	93.3	58.8	57.0	10.5	67.0	95.2	2.4
Percent SC, sample 4							97.1	5.1
Percent SC, sample 5							94.5	1.6
Mean percent SC	62.9	92.1	51.9	54.7	15.4	60.5	96.2	3.1
Standard deviation	0.86	1.85	5.98	2.40	4.48	6.52	1.24	1.38
Std error of the mean	0.49	1.07	3.45	1.39	2.58	3.77	0.56	0.62

3.4 Summary

We have demonstrated a new counting-based approach for measuring the semiconducting fraction in SWCNT samples. This method combines the reliability of single-SWCNT level techniques with the versatility of an optical-based approach. In our work it was used to find the semiconducting fraction in a variety of as-grown or DGU-processed SWCNT samples. The results indicate that a growth method can significantly influence the semiconducting SWCNT fraction, which ranges from 15.7% achieved with a special CVD synthesis up to 92.2% in a CoMoCAT SG sample. DGU sorting was shown to be an effective method for obtaining more than 90% single electronic type enrichment of a standard polydisperse HiPco sample. With a total statistics of 12000 SWCNTs, our measurements of semiconducting fraction show good precision and appear consistent with prior expectations for the sample compositions. We expect that our findings will serve as a useful reference for researchers growing or using SWCNTs prepared by these methods in various applications in science and medicine. These results may also allow absolute calibration of bulk characterization methods based on spectroscopic techniques such as Raman and absorption spectroscopy. For instance, an absorbance-based assay has potential for providing a valid estimate of semiconducting fraction given a set of reference values obtained in this work and an improved knowledge of absorption backgrounds discussed in the next chapter.

CHAPTER 4

Investigating sources of absorption backgrounds in single-walled carbon nanotube samples

4.1 Introduction

As described above, SWCNTs are used in a number of applications such as chemical sensors,[130,131] field emission sources,[52] and medical therapeutic agents[50,132,133] that require pure and well-characterized material. The impurities in SWCNT bulk samples may include residual metallic catalyst, multiwalled carbon nanotubes, amorphous carbon, and giant fullerenes. Moreover, the SWCNT composition is heterogeneous, containing a range of structural species with different diameters, roll-up angles, and electronic types; a distribution of nanotube lengths; and nanotubes in different states of aggregation and perfection. Sample characterization and purification are therefore essential tasks for SWCNT researchers.

SWCNT sample purity can be assessed through thermogravimetric analysis,[134-136] fluorescence efficiency[137] and bulk absorption measurements.[138-140] Compositional studies are often performed with Raman, absorption and photoluminescence spectroscopy. Absorption spectroscopy is one of the simplest and most commonly used tools for both SWCNT composition and purity analysis in the visible and near-IR. This wavelength range includes the distinct, structure dependent optical transitions of metallic and semiconducting SWCNTs.[20,64,141] Underneath these resonant transition peaks is a broad and nearly featureless background. Such background has been previously attributed to near-ultraviolet plasmon resonances of nanotubes and carbonaceous impurities.[61,142] Itkis et al. devised a sample purity measure based on the ratio of resonant to background

absorptions for dispersed samples in which individual (n,m) peaks are not resolved.[63] Tan and Resasco have presented a similar "resonance ratio" assessment for samples with resolved peaks.[143] Both assays are based on the assumption that a significant part of the background absorption arises from sample impurities. Absorption spectroscopy is also used as a compositional assay to deduce sample's (n,m) distribution by modeling its structured absorption spectrum.[144,145] Such simulations rely on prior knowledge of the (n,m) species' peak positions.[20,113] These methods, in contrast to fluorimetric analysis of background-free SWCNT near-IR emission spectra,[77,137] introduce an improvised correction to account for the broad background absorption and deduce relative magnitudes of specific (n,m) peaks. A third application in which absorption backgrounds play an important role is estimating the ratio of metallic to semiconducting SWCNTs in bulk samples.[119] Characterization and control of these ratios is particularly important for a number of applications such as SWCNT-based field effect transistors,[54-56] electrical vias,[53] and conductive transparent films[104,105] that require nanotubes of a single electronic type. Microscopic methods for determining metallic-to-semiconducting ratios have been developed,[111,146,147] but despite their versatility and high accuracy, they are impractical for routine use. Instead, the relative integrated absorption intensities of bands from metallic and semiconducting species may be used to form the basis of convenient bulk assays.[111,148] Accurate background subtraction is still an essential step here, because a majority of SWCNT samples typically show broad absorption backgrounds that are more intense than the bands to be quantified. Current approaches rely on modeled absorption backgrounds.[145] Limitations of these models can lead to inaccurate analyses hampering quantitative determinations of sample electronic composition.

We report here an experimental investigation of the source of SWCNT absorption backgrounds. This study is intended to aid the process of absorption-based SWCNT sample characterization by revealing the sources of absorption backgrounds and possibly accounting for them. One of our experimental approaches involves subjecting SWCNT samples with low initial backgrounds as a result of nonlinear density gradient ultracentrifugation (DGU)[149] to selected perturbations intended to increase backgrounds. Spectral changes induced by these perturbations help to identify extrinsic and intrinsic background contributions. The effects explored include backgrounds induced by ultrasonication of SWCNTs and surfactants; differences related to nanotube lengths; plasmonic absorption of SWCNTs and carbonaceous impurities; contributions from chemical derivatization; spectral broadening from bundled nanotubes; spectral congestion from closely spaced spectral peaks in samples with many (n,m) species; and absorptions of metallic SWCNTs. We find that several of these factors can contribute to absorption backgrounds in SWCNT suspensions and suggest an approach for quantitative analysis of those contributions.

4.2 Experimental

4.2.1 Sample preparation and processing.

Most of the SWCNT suspensions were prepared using HiPco SWCNTs from the Rice University reactor (batch 188.4). Studies of ultrasonication effects on SWCNT absorption backgrounds were performed with (6,5)-enriched SWCNT suspensions prepared according to the nonlinear DGU protocol reported recently.[149] This sample was chosen for its low initial absorption background and a single-specie spectrum allowing

convenient observation of spectral shifts, broadening and induced backgrounds. These DGU-processed samples were transferred from aqueous sodium cholate (used in DGU process) to 1% SDBS by filtering a suspension through a Nanosep 10K centrifugal filter, washing the nanotubes to remove sodium cholate, and resuspending them in 1% aqueous SDBS with the aid of bath and tip sonication.

Bath ultrasonication in our experiments was carried out using a Sharpertek model Stamina XP (4.5 L). Tip sonication experiments were performed on sample volumes of 1.5 mL using a Misonix model XL-2000 at powers of 4 to 5 W. Sonication-induced turbidity in SWCNT suspensions and surfactant solutions was reduced by centrifuging at 2817 × g for 5 min or by passive sedimentation under ambient conditions for 12 h.

Absorption backgrounds induced by carbonaceous impurities were studied using two amorphous carbon sources: 99.99% pure acetylene carbon black (Strem Chemicals, CAS# 7440-44-0) and thermally produced N134 (Continental Carbon) with particle sizes of 40 nm and 20-40 nm respectively. These materials were ultrasonically dispersed in 1% aqueous SDBS creating 6 suspensions for each carbon source with concentrations of 10, 6.67, 5, 2, 1 and 0.5 mg/L.

The effects of SWCNT sidewall functionalization were investigated by stepwise injection of up to 290 μg of gaseous ozone (produced by Ozone Services model GE60 generator) in O_2 into 80 μL of (6,5)-enriched SWCNTs in 1% aqueous sodium cholate.

For assessing spectral contributions from aggregation, a SWCNT sample dispersed in 1% sodium cholate and lightly centrifuged to remove impurities was compared to the one subjected to special processing that removed bundles. This procedure involved centrifugation for 30 min at 10,000 × g intended to eliminate large

bundles and additional DGU processing to further separate individual nanotubes from bundles.[150] The density gradient was prepared by discrete layering of pre-mixed aliquots of water and iodixanol of variable density (1.5 ml of 1.32 g/cm^3, 1.0 ml of 1.25 g/cm^3, 0.5 ml of 1.2 g/cm^3, 0.5 ml of 1.15 g/cm^3, 0.5 ml of 1.10 g/cm^3, 0.5 ml of 1.10 g/cm^3). The centrifuge tube was capped and tilted at an angle of 10° for 30 minutes. 0.5 mL of previously prepared SWCNT suspension in sodium cholate was added to the mixture. The sample was then centrifuged for 12 h at 268000 × g. The resulting suspension separated into two distinct fractions. The upper fraction containing mostly individual SWCNTs was collected for further characterization. The absorption spectrum of this aggregate-depleted sample was used extensively in this work for the studies of backgrounds arising from spectral congestion and metallic SWCNTs.

In order to investigate effects of SWCNT length on absorption background, SWCNTs were dispersed in 1% aqueous sodium deoxycholate by the means of sequential bath and tip sonication followed by a bundle removing DGU protocol described above. The sample was then length fractionated by electrophoresis in a 5% agarose gel using a procedure similar to that of Heller et al.[43] The specifics of this electrophoretic length separation are extensively described in the experimental section of Chapter 5. Fractions were further drop-cast onto silicon substrates, washed, and annealed at 450 °C to decrease the amount of residual surfactant. After this treatment, length distributions of SWCNTs in each fraction were assessed by AFM.

Metallic SWCNT contributions to absorption background were studied with SWCNTs from two different sources. For the purpose of comparing metallic and semiconducting SWCNT spectra, electronic type-enriched samples were obtained from

the HiPco (batch 188.4) starting material. Semiconducting (6,5) single-chirality enrichment was carried out using nonlinear DGU sorting procedure[149] in aqueous sodium cholate. Metallic sorting was achieved in a separate DGU protocol[151], after which SWCNTs were dialyzed to 1% sodium cholate in a 10 kD dialysis cassette.

A concentration dependence of absorption background contribution from metallic SWCNTs was assessed using suspensions prepared from 99% metallic-enriched SWCNT sample (NanoIntegris Inc). Portions of the sample were dispersed in 1% sodium cholate via tip sonication in ice bath at 4 W for the periods of 20 min at the concentrations of 2.5, 5.6 and 14.28 mg/L. Concentrations were deduced from sample weight measurements on a microbalance prior to dispersion.

The metallic contribution for modeling spectral congestion was evaluated by finding an absorbance per unit mass of a sample with known concentration. For that purpose a weighted amount of HiPco SWCNTs was dispersed in a certain volume of DMF by 20 min of tip sonication at 4 W. The absorption spectrum of the resulting suspension was measured, and DMF was then evaporated on a hot plate to constant weight. The resulting value of absorbance per unit mass found as the ratio of absorbance at 700 nm to the sample weight was further used to estimate SWCNT concentration in the aggregate-depleted sample from its absorption spectrum.

4.2.2 Apparatus

Visible-near-IR absorption and Raman spectra (740 nm laser excitation) were measured using a prototype NS2 NanoSpectralyzer (Applied NanoFluorescence, LLC). The configuration of this instrument allowed near-IR and visible absorption

measurements along the same optical path through the cell (Figure 39), minimizing discrepancies. The Raman signal from a SWCNT suspension was collected by a Si detector array thermoelectrically cooled to 0°C.

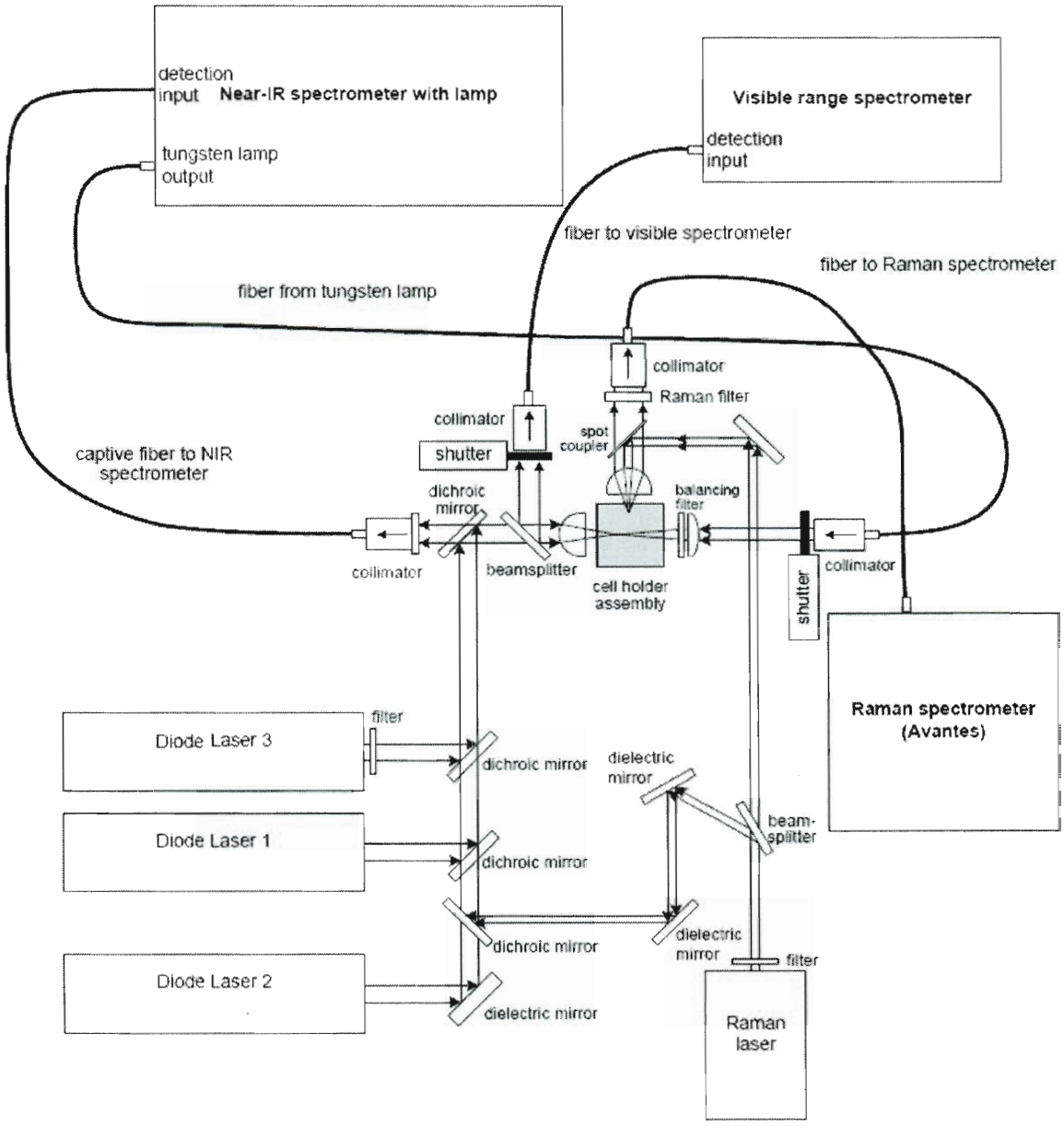

Figure 39. Schematics of the prototype NS2 NanoSpectralyzer (Applied NanoFluorescence, LLC) with Raman spectroscopy capabilities.

A Veeco Multimode 3A atomic force microscope was used in this work to image SWCNTs and assess SWCNT length distributions in electrophoreticaly separated fractions.

4.3 Results

4.3.1 Extrinsic factors

4.3.1.1 Ultrasonication: surfactant effects

Tip or bath ultrasonication is a standard step in the preparation of nearly all SWCNT suspensions. The effects of this procedure on SWCNT absorption backgrounds were examined using a starting sample that had been purified and enriched in (6,5) SWCNTs through nonlinear density gradient ultracentrifugation (DGU) and suspended in 1% aqueous sodium dodecylbenzenesulfonate (SDBS). The sample initially displayed low relative background absorption, as shown by the bottom trace in Figure 40a. Hourly absorption measurements during a total 3 h period of bath sonication did not show significant background changes. Some minor spectral variations observed in this experiment were not consistent with sonication time and therefore attributed to the uncertainty of absorption measurements.

Further testing of ultrasonication procedures continued with a harsher tip sonication applied for periods of 30 min to 3 h. This treatment induced significant systematic increases in absorption background, as shown in Figure 40a. This effect might have been attributed to sonication-induced changes in SWCNT structure leading to plasmonic-like absorption. However, the appearance of visible turbidity in the sonicated sample suggested that the observed background elevation could be due to light scattering

instead of absorption. To test whether the SDBS surfactant, rather than the SWCNTs, are the source of such sonication-induced scattering, we subjected a solution containing only SDBS to up to 3 h of tip sonication. This processing produced similar systematic increases in absorption baseline with sonication time (Figure 40b). However, the sample's spectrum returned to its initial level after mild centrifugation or after leaving the sample undisturbed for 12 h under ambient conditions. This suggests that extensive tip sonication of SDBS solutions can cause the formation of small particles, significantly denser than water, that are responsible for light scattering in the sample. Such particles may be formed due to chemical reactions of SDBS during solvent cavitation.

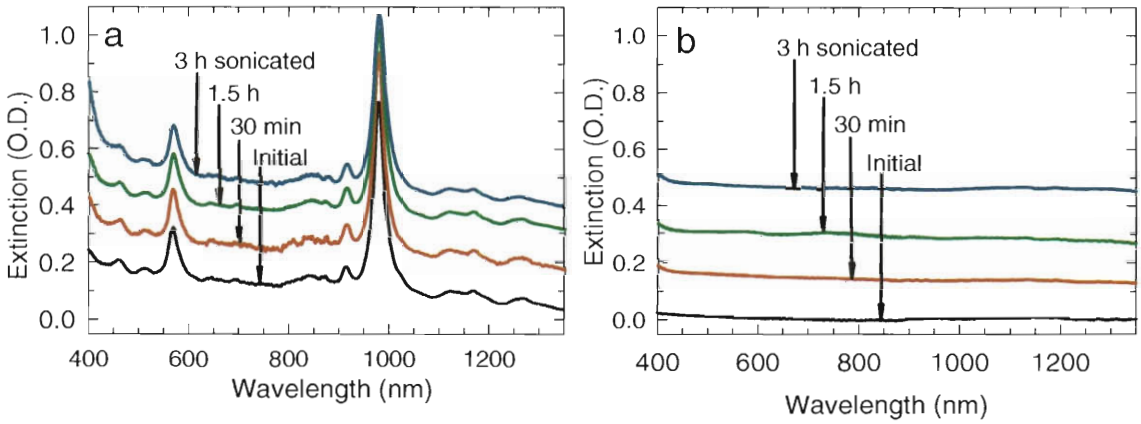

Figure 40. Effects of tip sonication on the absorption spectra of (a) a (6,5)-enriched SWCNT sample suspended in 1% aqueous SDBS and (b) 1% aqueous SDBS without nanotubes. Tip sonication times are 0 min (black curve), 30 min (red curve), 1.5 h (green curve), and 3 h (blue curve).

4.3.1.2 Ultrasonication: SWCNT effects

Even though the background increase observed in Figure 40a appeared to be mostly due to surfactant effects, the possibility of SWCNT contributions to sonication-induced spectral changes had to be investigated. For that purpose the background due to surfactant scattering was eliminated by mild centrifugation at the same conditions that removed the elevated background (Figure 40b) in a control surfactant solution. The residual background absorption of the sample sonicated for 3 h and then centrifuged was further compared to the absorption spectra of a sample sonicated for 3 h and then left settled at also ambient conditions for 12 h and with initial SWCNT suspension (Figure 41a) that had not undergone excessive sonication treatment. According to the heights of (6,5) E_{11} and E_{22} peaks, there was no significant change in SWCNT concentration in the process of centrifugation. We note that standing for 12 hours at ambient conditions resulted in a spectrum similar to the one after mild centrifugation. However, there are still significant differences between the initial spectrum and that after sonication and centrifugation. The main difference between those two absorption lines shapes was an elevated background in the short-wavelength part of the spectrum and a ~ 3 nm read shift of absorption features, illustrated clearly by the subtracted plot of Figure 41b. On this plot the derivative shapes at the positions of the E_{22} and E_{11} peaks arise from processing-induced spectral shifts. Short-wavelength background increase together with a red shift suggests that SWCNTs have undergone some chemical change in the process of sonication such as functionalization or damage. Raman spectroscopy of sonicated aqueous SWCNT suspensions was used to monitor the D-band intensity, which corresponds to the degree of disorder in SWCNT structures. However, these Raman

spectra (Figure 42) reveal only a slight change in D-band intensity. Therefore we attribute the resonant red shifts and additional absorption background to some minor variations in SWCNT structure induced by intense sonication.

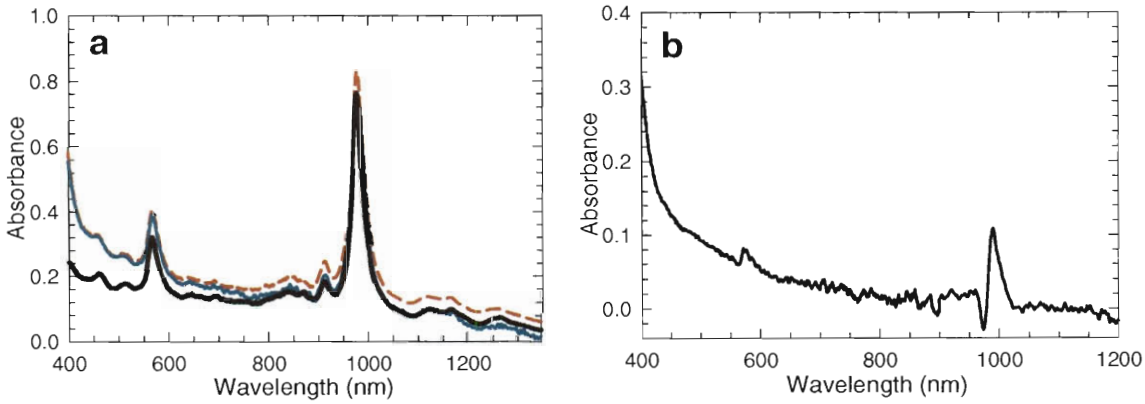

Figure 41. Persistent effects of tip sonication on the absorption spectrum of a (6,5)-enriched SWCNT suspension in aqueous SDBS. (a) spectra before tip sonication (thick black curve), after 3 h of sonication followed by 12 h of settling (dashed red curve), and after 3 h of sonication followed by mild centrifugation (thin blue curve). (b) difference spectrum showing net effect of 3 h of sonication and mild centrifugation. Features near 570 and 1000 nm arise from broadening and red shifts of the resonant absorption peaks.

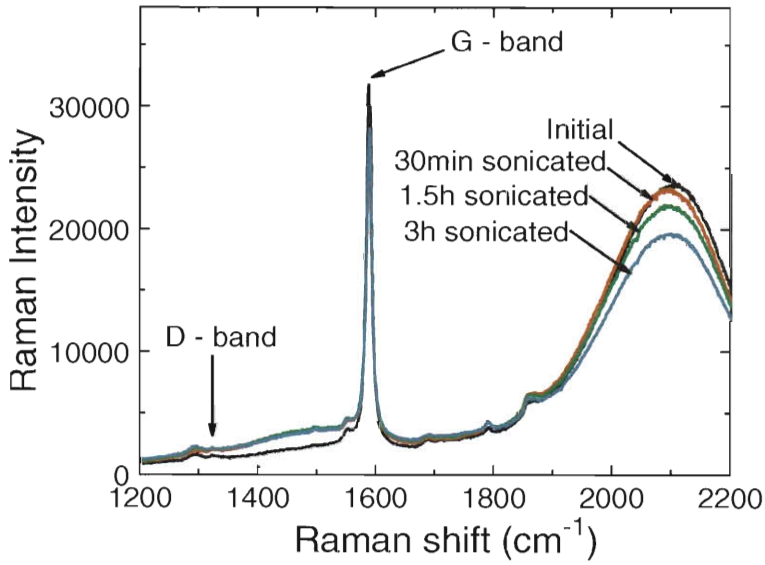

Figure 42 – Raman spectrum of (6,5) SWCNT enriched nanotube suspension in aqueous SDBS after the periods of 30 minutes to 3 hours of tip sonication. Broad features in the background of sharper Raman peaks represent SWCNT photoluminescence produced by 740 nm Raman excitation laser.

4.3.1.3 Chemical functionalization

Chemical functionalization is commonly used to solubilize SWCNTs without the aid of surfactant. Some functionalization can also occur during harsh treatment of SWCNTs such as acid purification or high power ultrasonication. Typical covalent functionalization of a SWCNT converts carbon atoms on the nanotube sidewall from sp^2 to sp^3 hybridization. This removes electrons from the delocalized π-system and introduces local electronic perturbations. Such defects in SWCNT structure may quench nanotube photoluminescence[68] through the charge-induced quenching mechanism described in Chapter 2. It has also been shown that extensive covalent functionalization strongly affects absorption spectra. It eliminates resonant peaks leaving a broad,

featureless spectrum.[152,153] To monitor the early spectral changes induced by covalent sidewall functionalization, we exposed a (6,5)-enriched sample of surfactant-suspended SWCNTs to modest doses of gaseous ozone. Figure 43a shows the sample's absorption spectra before and after this reaction and Figure 43b illustrates the difference between them. Chemical derivatization has weakened, broadened, and slightly red-shifted the resonant absorption features (Figure 43a). It has also added a substantial broad absorption background, increasing in the short-wavelength region. In Figure 43b this background is approximated by the smooth curve. The peaks in the subtracted spectrum beneath the fit curve arise from broadening and red shift of absorption features after ozonation. The shape of the functionalization-induced background resembles the one in Figure 42b, suggesting a possibility of a slight sidewall derivatization in the process of high power tip sonication. Finally, as a result of this study we infer that even minor functionalization can contribute to SWCNT absorption backgrounds.

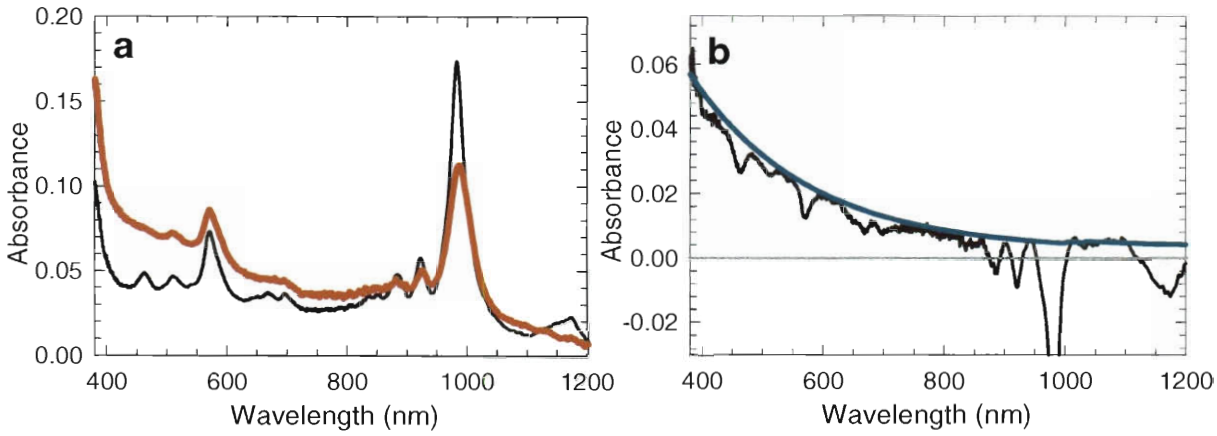

Figure 43. Spectral effects of covalent sidewall reaction. (a) absorption spectra of a sample of (6,5)-enriched SWCNTs suspended in sodium cholate before (thin black curve) and after (thick red curve) injection of ozone. (b) difference spectrum of the traces in (a). Sharp features reflect weakened and broadened resonant peaks in the reacted sample. The smooth blue curve shows an estimate of the broad spectral background induced by the sidewall reaction.

4.3.1.4 Amorphous carbon impurities

Amorphous carbon is considered to be a common SWCNT contaminant that may contribute to absorption backgrounds.[154] It exhibits strong plasmonic absorption peaking in the near-ultraviolet.[155] To quantify the effect of carbonaceous impurities on absorption backgrounds of impure SWCNT samples, two types of amorphous carbon, acetylene carbon black (Strem Chemicals) and N134 (Continental Carbon) were studied. Figures 44a and b illustrate the systematic background increase with concentration of amorphous carbon. Clearly, backgrounds from those carbon sources have different spectral shapes. However, each can be fit to the three parameter exponential form $A = a \cdot (y_0 + e^{-b \cdot \lambda})$ with

b fixed for a specific carbon source. Both fits reveal a linear relationship (Figure 44c) of the amplitude parameter *a* with concentration in accordance with Beer's law, with proportionality constants α_{N134} and α_{Ac}. The differences between fit parameters indicate that the background shapes will depend on the type of carbonaceous impurity. However, it is possible to estimate a rough upper limit to the amorphous carbon content in SWCNT samples by fitting the improvised absorption baseline by the exponential function given above and dividing the deduced amplitude parameter by a typical α value of about 0.1 L/mg.

To simplify the assessment of absorption background sources other than amorphous carbon, we suggest the use of ultracentrifugation or chromatographic purification[156] in order to decrease the concentration of carbonaceous impurities.

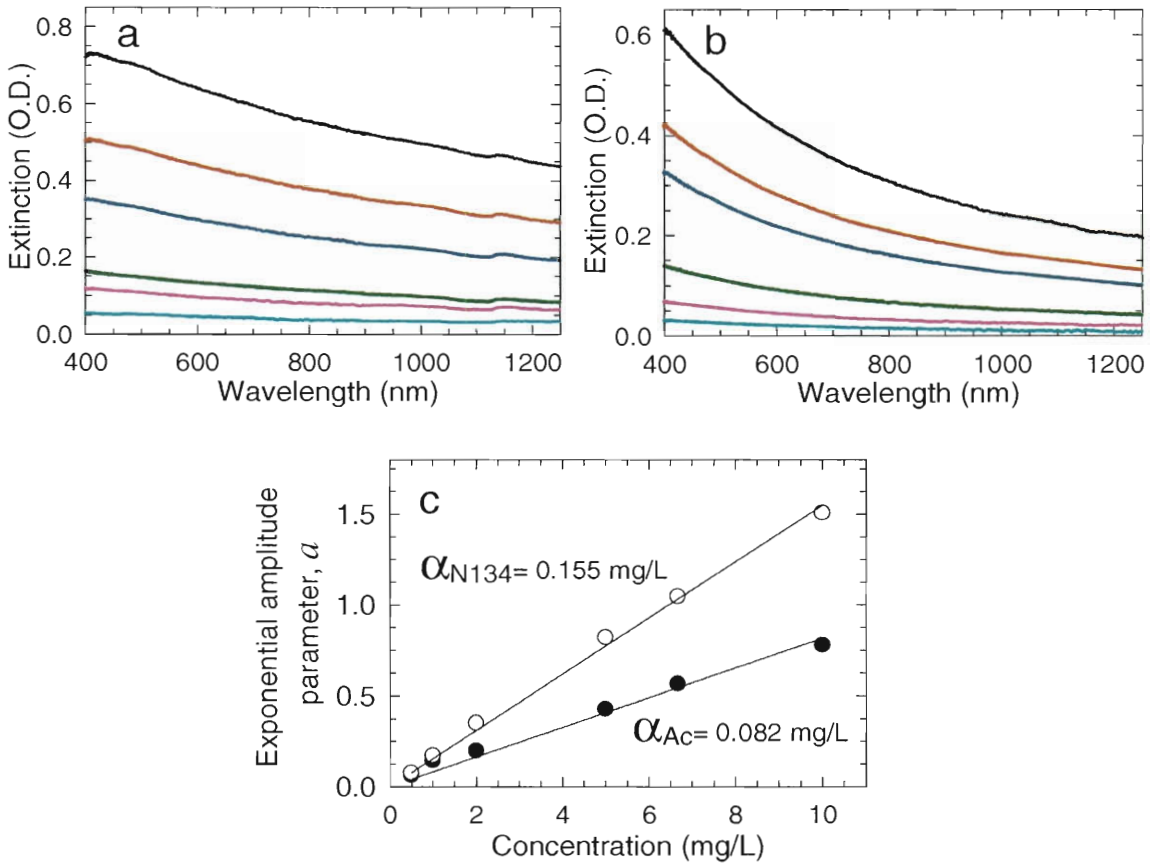

Figure 44. Spectral effects of amorphous carbon content. Absorption spectra are shown for different concentrations of two amorphous carbon types: Acetylene carbon black (a) and N134 (b). Concentrations from top to bottom curve vary as 10, 6.67, 5, 2, 1 and 0.5 mg/L. Absorption spectra were approximated with exponential decay fit $A = a \cdot (y_0 + e^{-b \cdot \lambda})$ with a fixed fit parameter b. For acetylene carbon black b = 0.00155 nm^{-1} whereas for N134 b = 0.003 nm^{-1}. The linear dependence of fit parameter a on the concentration of amorphous carbon: $a = \alpha \cdot C$ is described in (c). α_{N134} and α_{Ac} are the slopes of those linear fits.

4.3.1.5 Aggregation

Another possible source of absorption background is aggregation of SWCNTs into nanotube bundles. Aggregation was noticed to broaden and red-shift the resonant absorption features,[64] through electronic coupling, allowing charge and energy transfer between bundled SWCNTs. To examine the influence of bundling on the absorption background, we have designed a reverse experiment starting from more bundled SWCNT sample and progressing to a less bundled one. In this experiment absorption spectra of a polydisperse SWCNT sample in 1% aqueous sodium deoxycholate were compared before and after purification by a specific DGU procedure. That process, based on a difference in buoyant densities of SWCNTs and SWCNT aggregates, efficiently separates out most of the bundles without changing the nanotube length distribution or introducing defects. Figure 45a displays absorption spectra of the sample before and after such bundle depletion. The processed sample spectrum shows substantial increases in peak-to-valley ratio. That parameter, which is widely used as a measure of SWCNT sample purity,[63,143,157] here reflects a change in aggregation rather than purity. We suggest that nanotube aggregation broadens the resonant absorption peaks and leads to background growth and decrease of peak-to-valley ratio through increased spectral congestion (see following section).

To describe the effects of individual absorption peak broadening on the combined spectrum we have simulated near-infrared part of the absorption spectrum of an aggregate-depleted sample as a sum of individual E_{11} components representing a number of different semiconducting SWCNT chiralities (for procedure, see following section). When the simulated individual peak widths were increased by up to a factor of 3 to model

aggregation-induced broadening, the peak-to-valley ratios in the combined spectrum decreased (Figure 45b). The values of peak-to-valley ratios will of course vary depending on a sample's (*n*,*m*) distribution. In the case of our HiPco spectrum, we show in Figure 45c the how the ratio found at the 1264 nm absorption peak varies with individual peak width used in simulations. The results indicate that SWCNT aggregation in typical polydisperse samples can cause a factor of two decrease in peak-to-valley absorbance ratios. This parameter can in principle be used to assess the extent of aggregation in SWCNT suspensions relative to a chosen standard disaggregated sample.

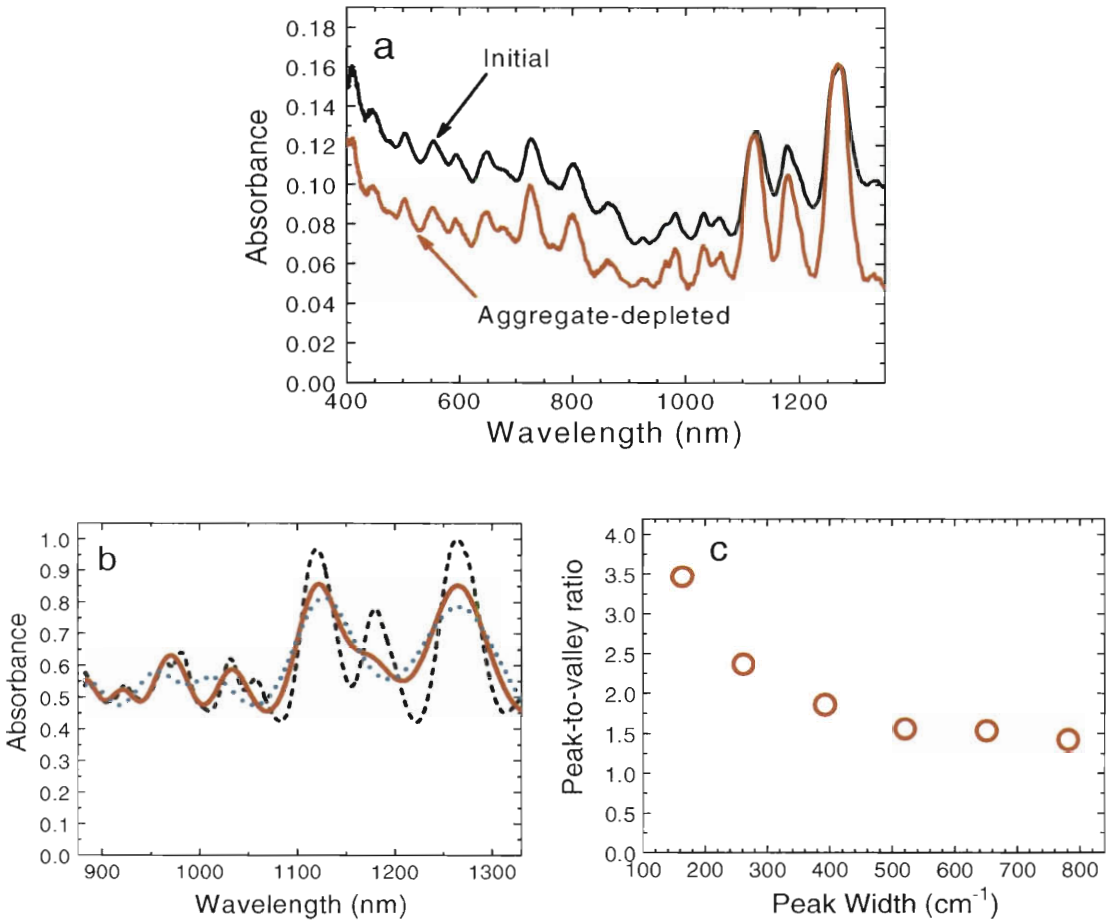

Figure 45. Spectral effects of SWCNT aggregates. (a) upper (black) curve shows the absorbance of a SWCNT sample in aqueous sodium deoxycholate, and the lower (red) curve shows the spectrum of the same sample after DGU processing to remove aggregated SWCNTs. The aggregate-depleted spectrum has been scaled to match absorbance values at the 1270 nm peak. (b) simulated spectra obtained as a sum of individual components that are broadened, as compared to the ones in the initial disaggregated spectrum (highest black curve), by factors of 2 (medium red curve) and 3 (lowest blue curve). (c) dependence of peak-to-valley ratios at the 1264 nm absorption peak on the widths of individual fit components.

4.3.2 Intrinsic factors

4.3.2.1 Spectral congestion

Another possible contribution to absorption backgrounds is congestion: the presence of numerous, closely spaced transitions that overlap over large ranges. In sorted SWCNT spectra containing few absorption peaks (Figure 42) this effect is absent. However in samples containing relatively large average diameters and broad (n,m) distributions providing a significant number of overlapping absorption features, spectral congestion may result in additional absorption backgrounds. To test this idea, we used a measured absorption spectrum of the DGU-processed aggregate-depleted sample similar to the one described in the section above on aggregation effects. As a starting correction, we subtracted a background contribution from metallic SWCNTs estimated using the procedure described in the section below on metallic backgrounds and a rough assessment of total SWCNT concentration (see Experimental section). The NanoSpectralyzer fitting software was then used to model the spectrum. Since the modeling routine is intended for simulating SWCNT photoluminescence, only the near-IR part of the absorption spectrum was modeled. This simulation used a parameter set with the positions, widths, and shapes of numerous (n,m) semiconducting emission peaks deduced from prior photoluminescence analysis of similarly prepared samples in the same surfactant. Minor fitting adjustments were allowed to account for small Stokes shifts between absorption and emission peaks and a slight peak broadening that could arise from a small fraction of nonemissive bundles remaining after disaggregation. Those contribute to absorption but not fluorescence spectra, therefore adding broader

components only to absorption peaks. The result of the simulation is shown in Figure 46a as a thin white curve representing the sum of the (n,m) absorption components plotted below it. Note that although each absorption component in the simulation is assumed to have zero baseline, their sum results in a spectrum with a substantial background. Since this simulation neglects E_{22}^{S} transitions situated in the visible part of the spectrum, which have greater spectral widths than near-IR E_{11}^{S} transitions, we infer that spectral congestion will cause even larger absorption backgrounds at shorter wavelengths in polydisperse SWCNT samples.

We propose a method to distinguish between background components from spectral congestion and other sources in polydisperse samples. It involves finding a calibration curve that relates apparent peak widths to the background absorptions from the other sources. Since most of those sources including amorphous carbon and metallic SWCNTs (see following section) induce exponential-like backgrounds, we simulated such a situation by adding backgrounds of the form $A = a \cdot e^{-\lambda b}$ to the spectrum in Figure 46a. Exponential parameters were chosen so that the shape factor b = 0.00155 nm^{-1} reflects the exponential behavior of backgrounds from acetylene carbon black and metallic SWCNTs and an amplitude parameter a varies from 0 to 0.49 times the peak absorbance at 1264 nm. After the addition of exponential backgrounds, modified spectra were modeled using the same simulation routine, allowing only variation of the shared width of individual peaks. Though this simulation the apparent widths used for successful fitting were found to increase with added background (Figure 46b). To use this graph, an experimental spectrum should be simulated as a sum of (n,m) peaks of uniform width (in cm^{-1}). Then Figure 46b is used with the best-fit width value to estimate the corresponding

underlying exponential background. After subtracting such background the remaining part is attributed to spectral congestion.

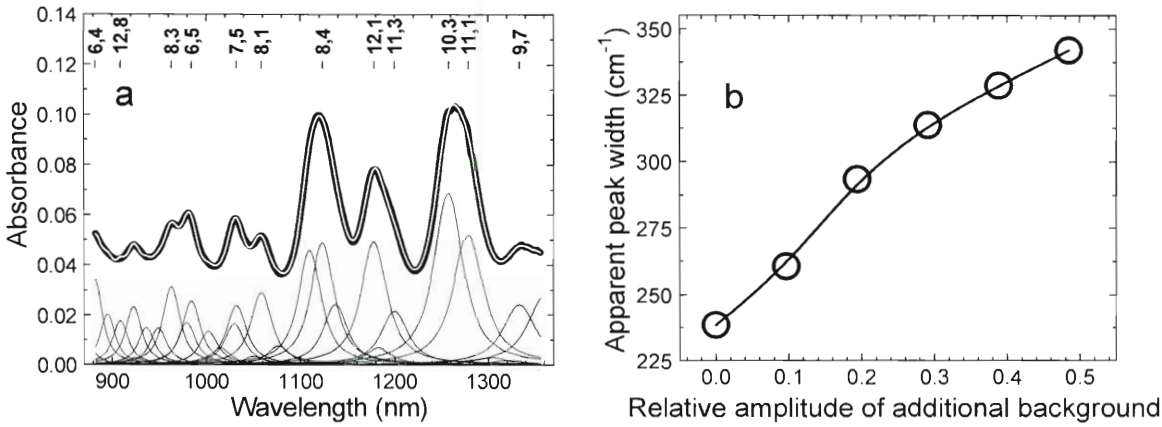

Figure 46. Background effects of spectral congestion. (a) - simulation of a SWCNT near-IR absorption spectrum illustrating spectral congestion. Thick black curve is the measured spectrum of disaggregated SWCNTs in aqueous sodium deoxycholate with subtracted background contribution from metallic SWCNTs (Figure 8 c). The thin white curve shows a simulation of that spectrum computed as the sum of the individual 238.5 cm^{-1} wide zero-background (*n*,*m*) components drawn below as thin black curves. (b) – describes the increase of the individual peak widths obtained in the process of spectral fitting with addition of exponential backgrounds of the form $A = a \cdot e^{-b \cdot \lambda}$ with fixed b = 0.00155 nm^{-1} to the infrared part of the spectra. The x axis represents fit amplitude, *a*, normalized by the intensity of 1264 nm feature.

4.3.2.2 SWCNT length effects

Nanotube length is the one of intrinsic properties of SWCNTs that may possibly affect absorption background. It can be influenced by the growth conditions and altered during the processing step. For example, SWCNT dispersion by ultrasonic agitation is known to shorten SWCNTs, cutting them into smaller segments.[40,42,158,159] Since nanotube ends containing sp^3-hybridized carbons would appear as defects to the π-electron system, shorter nanotubes could be considered to have higher defect densities than longer ones, and therefore more perturbed spectra. Background elevation due to functionalization-induced sidewall defects was described in section 4.3.1.3. To investigate if shorter SWCNTs would have elevated backgrounds, we studied SWCNT fractions of substantially different lengths separated by agarose gel electrophoresis. Figures 47b and 47c show length histograms of two of these fractions with average SWCNT lengths of 120 and 650 nm, as obtained from AFM image analyses. In Figure 47a we plot the absorption spectra of the two fractions. These spectra have not been normalized in order to avoid scaling absorption features that could have been broadened by aggregation during the electrophoretic separation. We suggest that the lower peak-to-valley ratios, smaller peak features, and altered relative peak heights in the short fraction may reflect a combination of minor aggregation and change in diameter distribution induced by the electrophoresis process.[43] However, absorption backgrounds of these two fractions are very similar in both shape and magnitude. Therefore we deduce that nanotube shortening to ~100 nm does not provide a major contribution to observed absorption backgrounds.

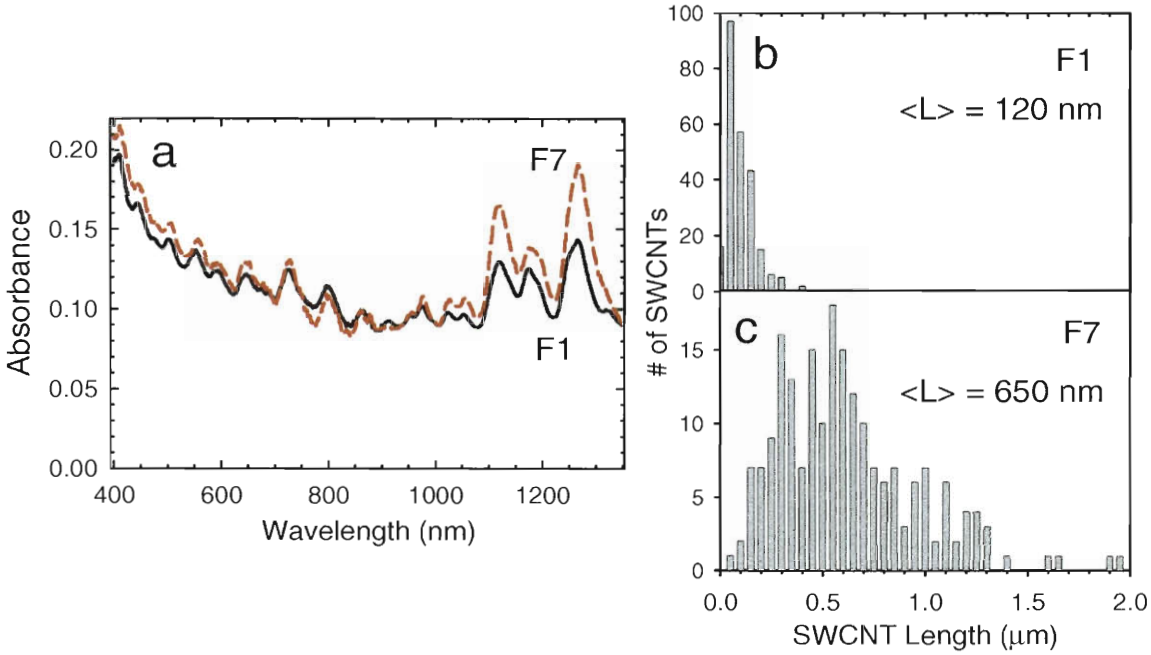

Figure 47. Dependence of absorption backgrounds on SWCNT length. (a) Absorption spectra of two SWCNT fractions: F1 (black solid curve) with average length of 120 nm, and F7 (red dashed curve) with average length of 650 nm. (b),(c) Length histograms of the two fractions obtained by gel electrophoresis. Total numbers of measured nanotubes were 241 and 204, respectively.

4.3.2.3 Metallic SWCNT contributions

Finally we consider the presence of absorption backgrounds in pure, pristine, disaggregated SWCNT samples free of spectral congestion. To address this, we used nonlinear DGU[149] to prepare a purified aqueous SWCNT dispersion highly enriched in the semiconducting (6,5) species. This sample contained few chiralities and was depleted of bundles and amorphous carbon due to DGU processing. Its absorption spectrum, represented by a blue curve in Figure 8a, shows a very low background, less than 2% of

the E_{11}^{S} peak height. This demonstrates the absence of intrinsic absorption backgrounds in pure semiconducting SWCNTs.

To investigate whether metallic SWCNTs have similarly low intrinsic backgrounds, we prepared a metallic-enriched sample using the same starting material and comparable processing methods. In this processing, individually suspended SWCNTs were sorted by electronic type and also separated from less buoyant impurities and nanotube bundles. The absorption spectrum of the metallic-enriched SWCNT sample (a red curve in Figure 48a) showed several resonant features between 500 and 650 nm assigned to the transitions of metallic species. The presence of several (n,m) species in this sample may account for some spectral congestion and, therefore, elevated background below 700 nm. However, a significant absorption extending beyond 1000 nm cannot be assigned to the tails of the Lorentzian peaks between 500 and 650 nm.

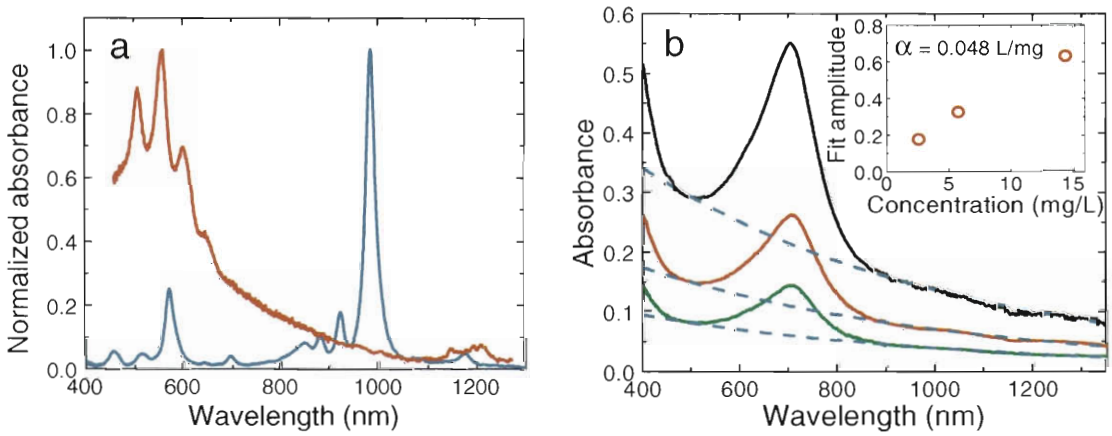

Figure 48. Absorption spectra of DGU-purified SWCNT fractions. Frame (a) shows absorption spectra of highly enriched (6,5) semiconducting species (blue curve) and highly enriched in metallic species of similar diameter (red curve). Frame (b) includes absorption spectra of NanoIntegris metallic-enriched SWCNTs at 2.5, 5.6 and 14.3 mg/L (green, red and black curves respectively), with their backgrounds

approximated by the exponential decay fit $A = a \cdot e^{-b \cdot \lambda}$ (blue dashed curve) with fixed b = 0.00155 nm^{-1}. An inset in the middle frame represents a dependence of exponential fit amplitude parameter a on the concentration of SWCNTs in suspension with a slope α = 0.048 L/mg.

We suggest that such broad background is intrinsic to metallic SWCNTs. This view is consistent with the dramatic reduction in background absorption found by Nish et. al. when metallic species were excluded from suspension by PFO-assisted dispersion.[160] One possible interpretation is that the broad absorption inherent to metallic SWCNTs is the tail of the π-plasmon resonance,[161] which may be more intense (relative to E_{11} transitions) in metallic than in semiconducting nanotubes. Another possible assignment is to perpendicularly polarized E_{01}^{M} transitions (Figure 49), which would appear at lower energies than E_{11}^{M} and have no counterpart in semiconducting nanotubes.[162] Since unlike semiconducting species, metallic SWCNTs have no electronic band gap, these transitions would form a continuous spectrum that may result in broad background absorption tailing into near-infrared to approximately half of the M_{11} transition energy (Figure 49). Although theory predicts such transitions to be weak because of depolarization effects, we speculate that they might be intensified by perturbations such as nanotube defects or non-uniform environments. In addition, we also consider the possibility of E_{00}^{M} transitions (Figure 49). Otherwise symmetry forbidden, those may appear in chiral metallic SWCNTs, in which a lack of the axial symmetry present in armchair and zigzag species[163] leads to sub-bands of mixed angular momentum character.

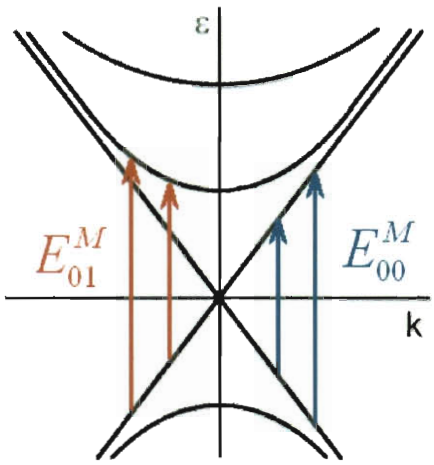

Figure 49. Band structure of a metallic carbon nanotube with E_{01}^{M} transitions shown with red arrows and E_{00}^{M} transitions – with blue arrows.

More rigorous theoretical modeling is necessary to determine the actual source of the metallic background. However, regardless of detailed assignment, our experimental results indicate that intrinsic absorption backgrounds are present in metallic but not in semiconducting SWCNTs.

To quantify these backgrounds with respect to metallic SWCNT concentration we have used a dry metallic-enriched SWCNT powder provided by NanoIntegris Inc. to create suspensions in 1% sodium cholate at different concentrations of SWCNTs. Absorption spectra of these suspensions (Figure 48b) show a single unresolved metallic peak at a position red-shifted from the ones in Figure 8a due to larger diameter of SWCNTs used as a starting material for DGU sorting in NanoIntegris. Nevertheless all of these spectra still have an apparent absorption background tailing into near-infrared that increases with concentration. To assess that dependence, we have fitted backgrounds with

observed a linear correlation between amplitude parameter *a* and the concentration of SWCNTs (inset in Figure 48b). The intercept of the line is quite close but not equal to zero contrary to the expectations from the Beer-Lambert Law. Such a discrepancy may be attributed to minor additional scattering backgrounds from surfactant disrupted in the process of sonication. A slope, α, of the inset graph in Figure 8b found from the two first points (complete sample dispersion was not achieved in the highest concentration sample) describes the relation between the concentration of metallic SWCNTs in the sample and the absorption backgrounds, they induced.

That allows a unique possibility of estimating metallic contribution to absorption background even in polydisperse SWCNT samples. If the total SWCNT mass concentration of a sample is known, its metallic concentration can be assessed using experimental values of metallic fractions reported for nanotubes from a variety of sources.[79] The deduced metallic SWCNT concentration is then multiplied by α to obtain parameter *a* in the expression $A = a \cdot e^{-b \cdot \lambda}$ that represents the background contribution of the metallic nanotubes.

4.3.3 Suggested procedure for estimating and decreasing absorption backgrounds

We can use the findings described in the sections above to minimize complications arising from absorption backgrounds. Some of the background contributions can be eliminated by specific sample processing. First, a solid SWCNT sample should be dispersed in a surfactant known to provide good individualization, using the minimum ultrasonic agitation needed for complete dispersion (avoiding

sonication-induced background contributions). The rigorous DGU procedure used for aggregate depletion in section 4.3.1.5 will then remove nanotube bundles as well as residual catalyst and amorphous carbon impurities. The relative extent of disaggregation can be monitored by measuring peak-to-valley ratios in the absorption spectra (as in Figure 45).

Following this processing, the absorption spectrum of the purified sample can be analyzed for spectral congestion and metallic background components. Spectral congestion is evaluated using the procedure described in the corresponding section above. The apparent peak widths found from the fitting procedure can be then used to estimate the background elevation from other sources (see Figure 46b). Assuming no significant sample functionalization happened during the growth and purification processes, this remaining background is attributed to metallic SWCNTs. Such a procedure was applied to find the metallic background in a DGU aggregate-depleted sample (Figure 50).

The knowledge of metallic background magnitude allows estimating the corresponding concentration of metallic SWCNTs using the value of α, given in Figure 48b, and the amplitude of exponential (metallic) background found from Figure 46b. If the total SWCNT mass concentration is known for the sample, then this procedure allows estimation of the semiconducting-to-metallic ratio. Such spectroscopic evaluation is more accessible to general researchers and less laborious then previously mentioned microscopy-based techniques.

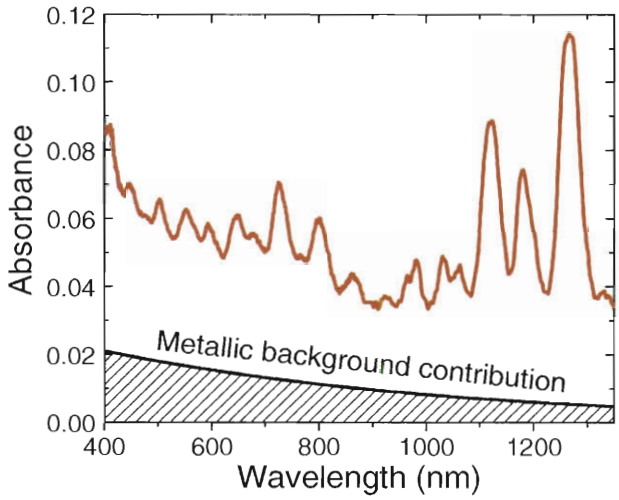

Figure 50. Deduced metallic contribution to absorption background in disaggregated HiPco SWCNT sample.

4.4 Summary

We have investigated and quantitatively assessed a number of possible sources of absorption background in aqueous SWCNT samples. Extended intense ultrasonication used to disperse SWCNTs can give reversible background absorption attributed to particulate formation from damaged surfactant. Strong tip sonication is also observed to induce a persistent background component in the short-wavelength part of the spectrum that may arise from unintended nanotube chemical reactions or damage, but appears not to result from sonication-induced SWCNT shortening down to ~100 nm. Sidewall chemical functionalization broadens spectral components and adds a background also increasing toward shorter wavelengths. An additional background is induced by plasmonic absorption of carbonaceous impurities. It has been calibrated for the concentration of amorphous carbon from two sources. Well-dispersed SWCNT samples that have been DGU-enriched in a specific pristine semiconducting (n,m) species display

nearly background-free absorption spectra. However, similar samples purified by DGU but containing a wide range of semiconducting species can show elevated backgrounds from spectral congestion due to absorption peak overlap. A spectral simulation fitting routine distinguishes backgrounds from spectral congestion and other sources. We also observe that spectral congestion background is increased by nanotube aggregation. Extent of aggregation may be monitored using peak-to-valley ratios at selected peak positions. In contrast to their semiconducting counterparts, metallic SWCNTs exhibit intrinsic broad absorption backgrounds. An absorptivity coefficient found in this work allows estimating the magnitude of these backgrounds from the concentration of metallic SWCNTs in the sample.

Our results suggest that a combination of sample processing and analysis methods can minimize the absorption backgrounds of SWCNT samples and identify the remaining contributions from spectral congestion and metallic SWCNTs. This procedure allows finding relative magnitudes of (n,m)-specific E_{11} absorption bands and, therefore, provides an important insight into the sample composition. If total SWCNT concentration is known, it is also possible to estimate the semiconducting-to-metallic ratio in the sample. We believe that our findings will allow improved understanding and modeling of SWCNT absorption spectra while compensating and accounting for absorption backgrounds. It should then be possible to use absorption spectroscopy as a more powerful tool for analyzing SWCNT sample purity and content.

CHAPTER 5

Length-dependent optical properties of single-walled carbon nanotubes

5.1 Introduction

In addition to high demand in diameter and chirality-separated samples,[35,149,164-166177-179] a number of potential applications such as carbon nanotube fibers[167-170] or nanotube-reinforced polymeric materials[6-9,171,172] require SWCNTs of certain lengths. Longer SWCNTs of a specific electronic type can be also effectively used in electronics as ballistic conductors[173-175] or as major components in field effect transistors.[176-179]

Length separation of SWCNTs has been carried out using several methods that include density gradient ultracentrifugation[39,180] extraction into organic phase,[38] size exclusion chromatography[40-42] and gel electrophoresis.[43-45] SWCNT lengths in the aqueous suspension can be altered by such common preparation procedure as ultrasonication. In the process of ultrasonication, due to the energy transfer from air bubbles collapsing in the liquid, SWCNTs can be damaged or cut into shorter segments[40,42,43,158] depending on the time of exposure.

Solubilized SWCNT samples abundant in long nanotubes desirable for the number of applications described above can be dispersed with very mild sonication.[181] However such preparation may result in a significant concentration of SWCNT aggregates. To counter this problem, we suggest a method of obtaining well dispersed and disaggregated SWCNT surfactant suspensions with a large population of SWCNTs over 1 μm long by using high pressure microfluidics. In this method, SWCNT dispersion occurs without prior sonication due to shear forces in the microchannels. Optically these

suspensions appear to be similar to SWCNTs specifically disaggregated using a rigorous DGU procedure.[182]

The methods of length separation, shear-assisted dispersion and sonication-induced SWCNT scission provide a unique possibility of creating SWCNT batches with controlled length distributions. This allows quantitative optical and compositional studies of length-separated SWCNTs to find length dependence of SWCNT optical properties. Some recent experimental efforts in this area have reported nearly linear (per carbon atom) length dependence of absorption and photoluminescence[183] and one has shown an exponential dependence of quantum yield.[43] However a more refined characterization of SWCNT length-dependent photophysical properties with rigorously sorted samples and proper absorption background subtraction is still desired.

In this work we describe an in-depth study of the optical properties of SWCNTs, length fractionated using agarose gel electrophoresis and bath ultrasonication. The well-characterized narrow length distributed SWCNT fractions with lower absorption background obtained by these methods provide novel information about the length dependence of SWCNT photoluminescence, absorption and quantum yield. These relations offer insights into SWCNT excitonic effects.

5.2 Experimental

5.2.1 Electrophoretic length separation

The initial suspension of SWCNTs in 1% sodium deoxycholate (~ 1 mg/mL) was prepared with ultrasonic agitation (30 minutes bath sonication and 2 hours tip sonication in ice bath at an output power of 2 W/mL). Theesulting suspension was centrifuged for

30 min at 10,000 × g to remove large bundles. To further purify the sample, by separating individual SWCNTs from SWCNT aggregates, a DGU procedure described in the previous chapter was used. The DGU fraction containing individual nanotubes was then collected for further electrophoretic fractionation.

DC electrophoresis was performed using OWL D3 electrophoresis chamber. A running buffer of 0.75% agarose gel, 1% of SDBS, and tris-HEPES-SDS was prepared and poured into the chamber. The SWNCT separation was carried out at a current density of ~7 mA/cm^2 for 5 h. Eight first fractions were analyzed using photoluminescence and atomic force microscopy together with absorption and photoluminescence spectroscopy.

Our standard photoluminescence microscopy setup[98] was employed to record photoluminescence images of individual semiconducting SWCNTs in the length-separated fractions. In this setup, near-IR emission of semiconducting SWCNTs excited with a 659 nm diode laser was collected by a 60×, NA= 1 oil immersion objective on a Nikon TE-2000U inverted microscope and directed to a liquid nitrogen-cooled Roper OMA V 2D InGaAs camera.

Length distributions of SWCNTs in eight eluted fractions were found using Veeco Multimode 3A atomic force microscope. Prior to AFM imaging SWCNTs from length-separated fractions were deposited on 5 × 5 mm silicon chip substrates by a series of spin-coatings with consecutive rinsing of the sample surface with deionized water. A total of 1400 individual SWCNTs were studied with more than 90 SWCNTs analyzed for each fraction.

Absorption and photoluminescence of bulk SWCNT suspensions were recorded using an NS1 NanoSpectralyzer (Applied NanoFluorescence, LLC). Photoluminescence

spectra were simulated with the NanoSpectralyzer software fitting routine to deduce average SWCNT diameters in each fraction.

5.2.2 Shear-assisted dispersion

A model M110-L Microfluidizer (Microfluidics LLC) equipped with a H10Z 18000 psi interaction chamber was used for processing single-walled carbon nanotube (SWCNT) suspensions.[184] In one processing cycle at a pulse pressure of 8000 psi, raw SWCNTs (HiPco batch: 188.4) added to 1% aqueous SDBS or 1% aqueous sodium deoxycholate were dispersed and disaggregated. In this apparatus individual SWCNTs were stripped from the bundles due to shear forces induced by high pressure flow in microchannels.[184] Absorption and photoluminescence of the bulk SWCNT suspensions were recorded using a NS2 NanoSpectralyzer. A sample for disaggregation assessment was prepared by cycling the unprocessed mixture of raw SWCNTs and 1% aqueous sodium deoxycholate once through the Microfluidizer interaction chamber at 8000 psi and centrifuging the resulting suspension at 100000 × g for 1 h to remove impurities. Supernatant containing 70% of initial material according to spectroscopic analysis was collected and compared to the DGU aggregate-depleted sample described in the previous chapter.

Individual Microfluidizer-dispersed SWCNTs were further studied in suspension using photoluminescence microscopy. Their length distributions were assessed with Veeco Multimode 3A AFM. Samples for AFM analysis were prepared on 5×5 mm silicon substrates by immersing them in the vial with SWCNT suspension for up to 3 days. These substrates were then mildly washed and annealed in air for 30 minutes at

450ºC to remove excessive surfactant.

5.2.2 Ultrasonication-induced length scission

SWCNT suspension for length shortening ultrasonication experiments was prepared in 1% aqueous SDBS using shear-assisted dispersion (see previous section). That starting suspension was then bath sonicated for periods from 0 to 420 minutes. After each period a portion of the main sample was collected and length-characterized with AFM and photoluminescence microscopy in the same way as the electrophoreticaly-sorted fractions. Based on these analyses, length distributions were constructed for seven fractions produced with different sonication times. Absorption and photoluminescence spectra of each fraction were recorded using the NS2 NanoSpectralyzer.

5.3 Results

5.3.1. Electrophoretic length separation

During the electrophoresis in agarose gel, some SWCNTs moved further from the injection point than the others, leaving an elongated gray trace in the gel body. This effect can be explained by a greater mobility of SWCNTs that moved a larger distance through the gel, which according to a previous report,[43] is dictated mainly by SWCNT length. To analyze the extent of such length separation, the SWCNT trace in agarose gel was cut into eight fractions from the most eluted to the least and analyzed by several characterization techniques. Atomic force microscopy of eight eluted fractions (Figure 51) showed observable differences in SWCNT lengths, with shorter SWCNTs present in the first fractions that have traveled further. Height profile measurements indicated that

the amount of loose aggregates and SWCNT bundles had increased in the last fractions, consistent with the assumption of lower mobility of bundles.

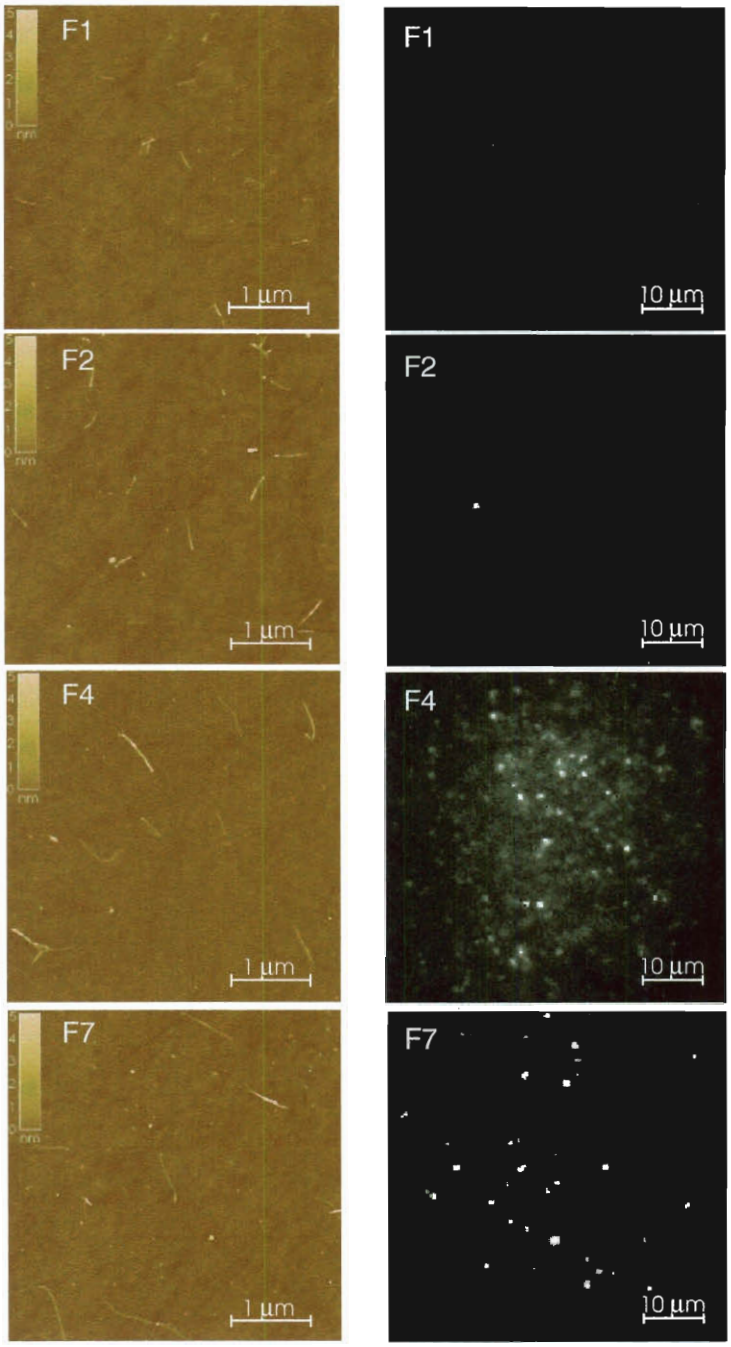

Figure 51. AFM and photoluminescence images of length-separated fractions. Length scales on AFM and photoluminescence images differ by one order of magnitude.

These observations were supported by photoluminescence microscopy of the same fractions. Photoluminescence images (Figure 51) show greater relative abundance of large bright spots representing longer semiconducting SWCNTs and SWCNT clusters in the later fractions. The absolute number of bright spots in those images is mainly dictated by the concentration of SWCNTs in the fraction. Since the resolution of photoluminescence microscopy was considerably lower than that of AFM, the length scale in photoluminescence images was chosen to be an order of magnitude greater. In addition, due to higher resolution of AFM images and the possibility of detecting both semiconducting and metallic SWCNTs, SWCNT length analyses of electrophoreticaly eluted fractions were preformed using atomic force microscopy. For each fraction, a SWCNT length distribution was constructed from measurements on at least 90 individual SWCNTs, adding up to a total statistical count of 1400 (Figure 52). Bundles were omitted from the statistics on the basis of height profile analysis described in Chapter 3. Some error could still arise from discrepancies in length measurements or from omitting SWCNTs shorter than 40 nm due to limited lateral resolution. Such discrepancies could affect only the first few fractions containing the shortest SWCNTs. However, due to the better SWCNT statistics in those fractions, we expect only minor error contributions.

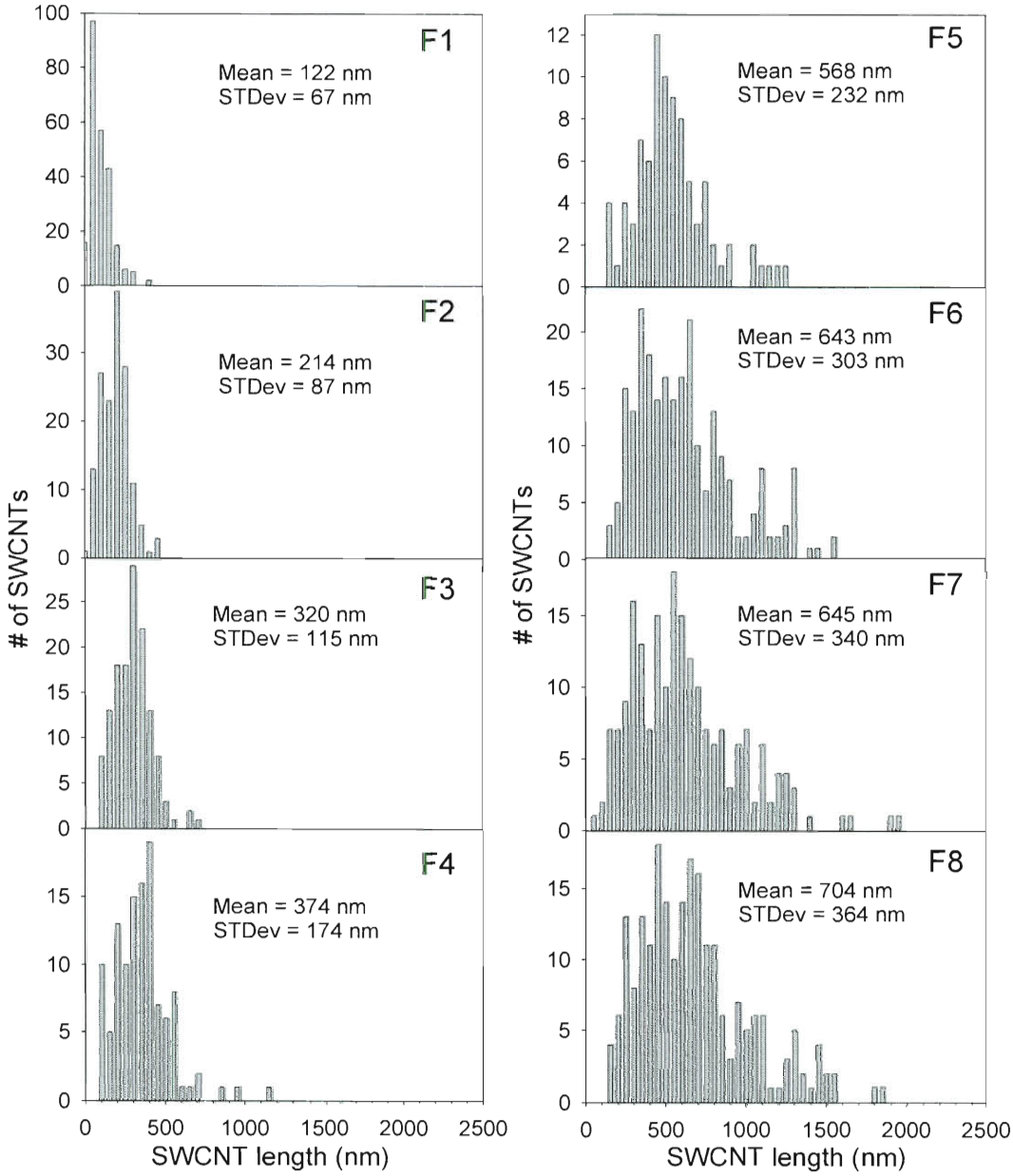

Figure 52. SWCNT length histograms from the AFM studies of eight length-separated fractions.

In Figure 52 the first five fractions have well-defined narrow length distributions with the center shifting towards greater length for each consecutive fraction. The last three length distributions, though, are rather broad and do not show much variation

among them. They represent the limit of length separation, possibly reflecting similar (low) mobilities of SWCNTs or SWCNT aggregates that are greater than a certain length. The mean SWCNT length and the standard deviation (Figure 53a and b) increase monotonically towards the later fractions. A doubled standard error of the mean, shown as error bars in Figure 53a, is small enough to allow precise assessment of the average SWCNT length.

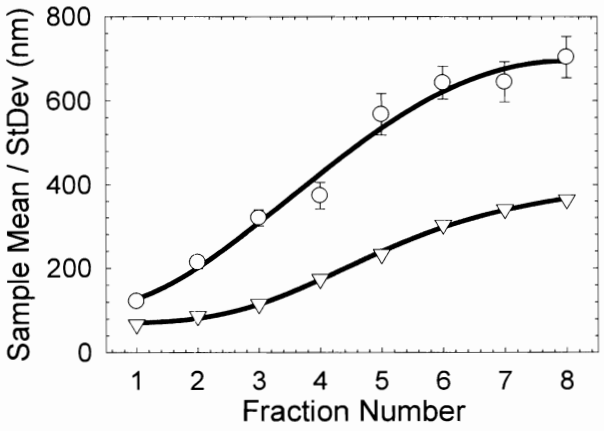

Figure 53. Mean length (circles) and standard deviation (triangles) plot for eight length-separated fractions. Error bars represent doubled standard error of the mean.

Optical properties of electrophoretically eluted fractions varied. For each fraction we have measured and assessed absorption (Figure 54a) and photoluminescence spectra. Since both absorption and photoluminescence depend on SWCNT concentration in each fraction, neither set of spectra on its own could accurately reflect the length dependence. Therefore to account for different SWCNT concentrations in eight eluted fractions, the photoluminescence signal was normalized by integrated absorption, providing concentration-independent emission spectra (Figure 54b). As a result, a clear increase in

normalized photoluminescence signal with average SWCNT length (fraction number) was observed.

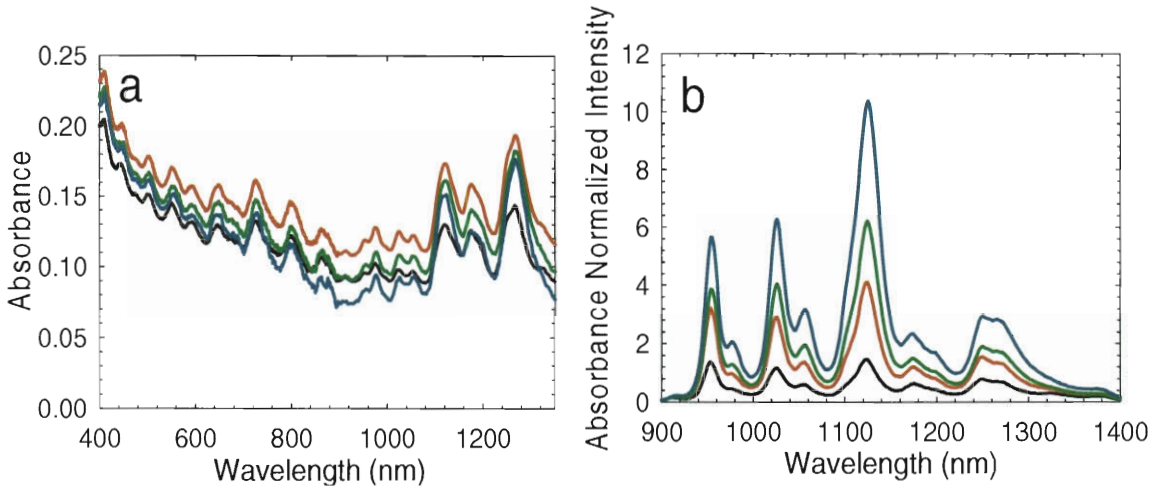

Figure 54. Absorbance (a) and absorbance normalized photoluminescence (b) spectra of four length-separated fractions: F1 (black), F3 (red), F5 (green) and F6 (blue).

However this increase turned out to differ among SWCNT chiralities, with larger diameter SWCNT peaks rising less in the later fractions. This suggests that SWCNTs of larger diameters traveled further through agarose gel than the smaller diameter ones. Such diameter dependence is similar to the one observed by Strano et. al.[43] To further characterize this effect, we calculated the average diameter of SWCNTs in each fraction using NS2 NanoSpectralyzer fitting software. This routine approximated individual SWCNT photoluminescence components and assessed the relative abundances of SWCNT chiralities in the fraction. The results indicate a small decrease in average SWCNT diameter in the later fractions (Figure 55). That confirms a mild diameter separation during electrophoretic length fractionation, although does not suggest it as a

suitable means for efficient SWCNT diameter and chirality soring[37,185] due to the relatively low magnitude of the effect.

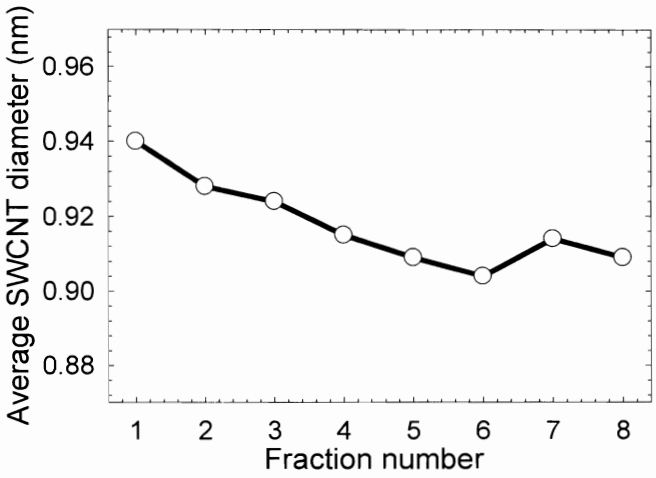

Figure 55. Change in average SWCNT diameter in eight length-separated fractions.

Using photoluminescence and absorption measurements, the relative photoluminescence quantum yield of SWCNTs in each fraction was estimated as the ratio of integrated photoluminescence to integrated absorption. In order to decrease possible uncertainty, the estimate was performed at 1000 – 1046 nm and 1081 – 1156 nm peak features that are largest and most resolved in the emission spectra. The dependence of relative quantum yield on average SWCNT length in eight separated fractions is illustrated in Figure 56. In contrast to a previous report,[43] the relative photoluminescence quantum yield did not increase exponentially with SWCNT length instead but instead rose more gradually to a seeming asymptotic level. The trend in Figure 56 shows lower quantum yields in the fractions with shorter SWCNTs, which can be explained by the

proximity of SWCNT ends that act as defect sites and can quench excitonic emission. This effect was previously described in section 4.3.3.2. Longer SWCNTs, with ends farther apart, are then supposed to have less quenching defects per unit length and therefore increased quantum yield. However, at even greater SWCNT lengths the ends become so far apart that their presence does not contribute significantly to the density of quenching defects. At that point, the SWCNT length no longer influences the quantum yield, which may account for an apparent asymptotic behavior displayed in Figure 56 at the greatest lengths.

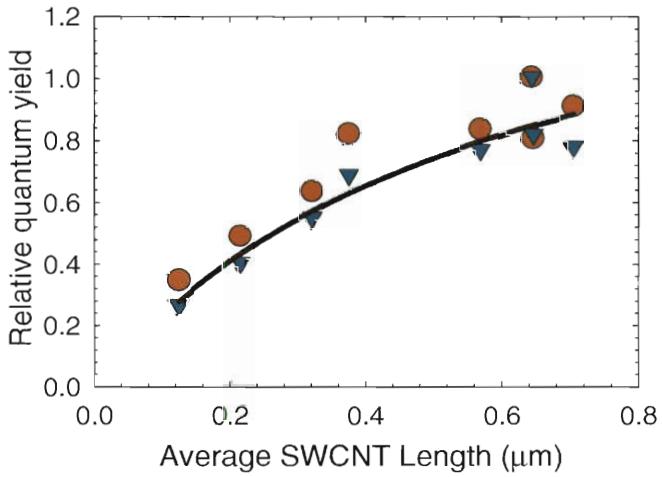

Figure 56. SWCNT length dependence of relative photoluminescence quantum yield calculated at 1000 – 1046 nm (red circles) and 1081 – 1156 nm (blue triangles) peak features. A black line represents a simple hyperbolic dependence best describing the data.

5.3.2. Shear-assisted dispersion

SWCNT suspensions for sonication-induced length fractionation experiments were prepared using shear-assisted dispersion. These samples, rich in SWCNTs over one micrometer long that have not been damaged or cut by ultrasonication, served as a non-perturbed starting material for further invasive processing. The advantages of the shear-assisted dispersion and the quality of the resulting suspensions will be discussed in this section.

This dispersion method is based on the separation of aggregated SWCNTs by shear forces from high-pressure flows inside the microchannels of the Microfluidizer apparatus.[184] As a result of such processing, SWCNTs mixed with 1% aqueous surfactant and cycled once through Microfluidizer interaction chamber at pressures of 8000 psi without prior sonication or centrifugation formed homogeneous suspensions and exhibited strong photoluminescence. Dispersions in two common surfactants, SDBS and sodium deoxycholate, were studied and compared in this work.

Photoluminescence microscopy images of microfluidically dispersed suspensions in SDBS and sodium deoxycholate showed a large number of observably long semiconducting nanotubes (Figure 57a and b). Compared to regular SWCNT suspensions in 1% aqueous SDBS prepared with the aid of 3 h bath and 10 minutes tip sonication (Figure 57c), Microfluidizer-processed samples (Figure 57a and b) show greater numbers of semiconducting SWCNTs over 1 μm long.

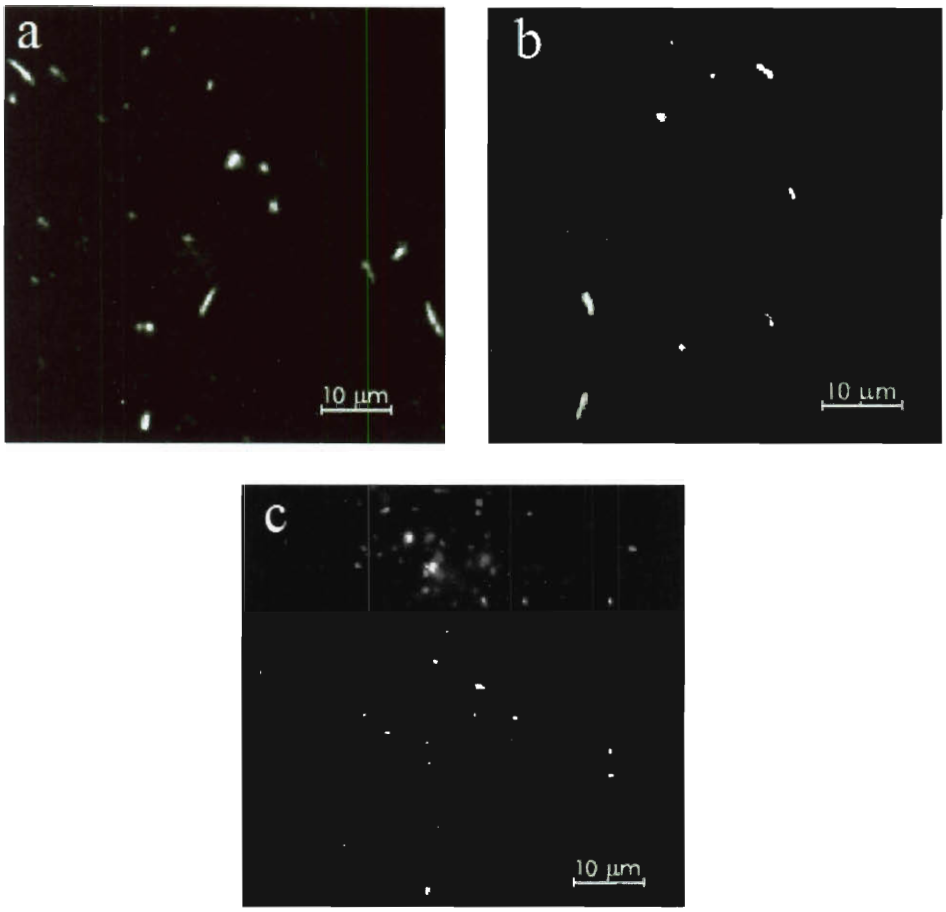

Figure 57. Photoluminescence images of SWCNTs dispersed in 1% aqueous SDBS (a) and sodium deoxycholate (b) using Microfluidizer. (c) - photoluminescence image of SWCNTs dispersed in 1% aqueous SDBS by ultrasonication.

After cycling the suspension several times thorough the Microfluidizer interaction chamber, a dramatic increase in photoluminescence intensity was observed (Figure 58a), indicating further SWCNT disaggregation. Photoluminescence spectra were normalized by integral absorbance to account for different SWCNT concentrations in suspensions that passed through the Microfluidizer interaction chamber different numbers of times. According to Figure 58b, after several cycles, photoluminescence efficiency approached a certain limit representing maximum disaggregation of SWCNTs in suspension for a

particular pressure in the Microfluidizer interaction chamber. Photoluminescence images of suspensions cycled 10 times through the interaction chamber (Figure 58c) also show observable decreases in SWCNT length, likely due to breaking of SWCNTs by shear forces. A similar effect was previously reported for multiwall nanotubes.[184] Although shortening may further aid the disaggregation process (shorter SWCNTs are less likely to form aggregates), for purpose of further length sonication studies, it is essential to obtain initial samples with longer SWCNTs. Thus, in this work we study suspensions processed by the Microfluidizer apparatus only once, which produces suspensions with the longest SWCNTs.

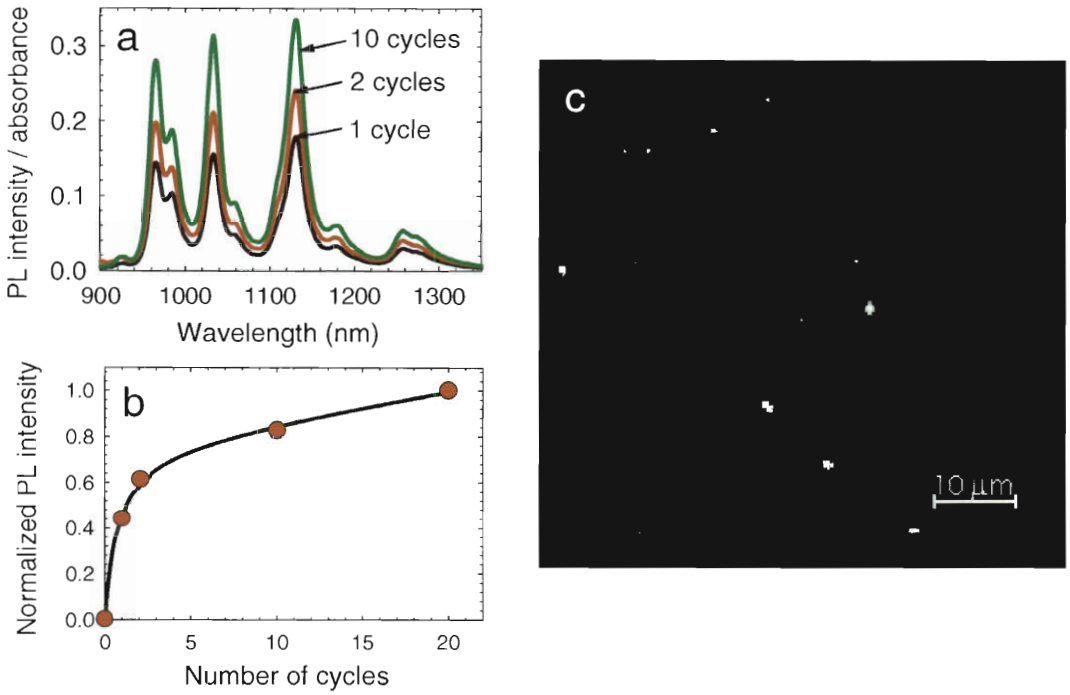

Figure 58. Effects of multiple shear processing. (a) – plot of absorbance normalized photoluminescence spectra of SWCNT suspensions in 1% aqueous SDBS that passed several times through Microfluidizer interaction chamber at 8000 psi. (b) – plot of normalized integrated photoluminescence intensity with respect to the number of times the same SWCNT suspension passed through Microfluidizer interaction chamber. (c) – photoluminescence image of SWCNTs in aqueous SDBS that have passed 10 times through Microfluidizer interaction chamber at 8000 psi.

In order to describe the degree of disaggregation after single-pass Microfluidizer processing, a SWCNT sample, shear-dispersed in 1% aqueous sodium deoxycholate, was centrifuged at 100000 × g for 1 h to remove impurities and compared to an aggregate-free reference. For that purpose we used a SWCNT suspension in aqueous sodium

deoxycholate that had undergone the rigorous DGU aggregate-depletion procedure described in the previous chapter. Absorbance spectra of Microfluidizer-dispersed SWCNTs (Figure 59a) exhibited well defined peak structures, often less prominent in regular sonication-dispersed suspensions, and the peak-to-valley ratios lower than but still comparable to the DGU-purified sample. The3 absorbance-normalized photoluminescence spectrum of shear-dispersed SWCNTs (Figure 59b) showed peak widths and intensities similar to DGU sample, indicating a significant degree of disaggregation among semiconducting SWCNTs after Microfluidizer processing.

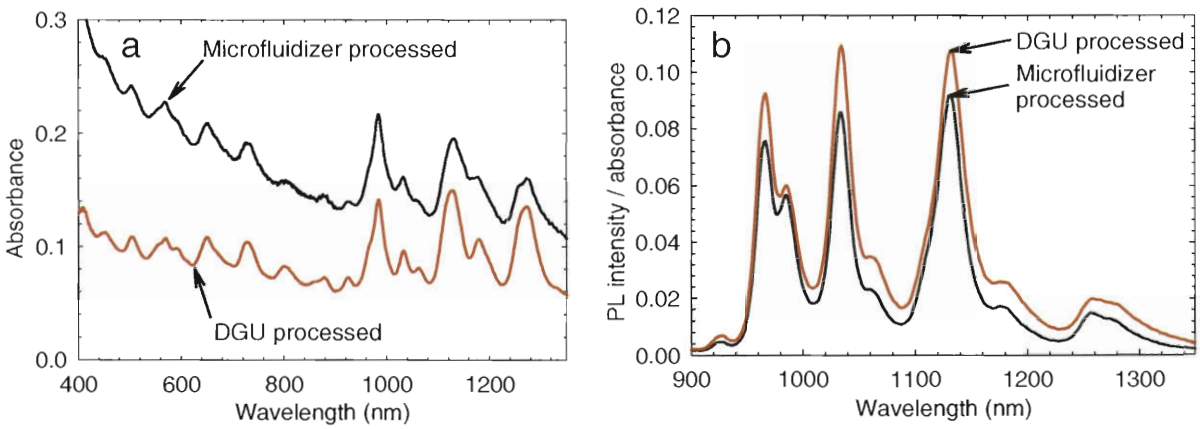

Figure 59. Differences between shear-processed and DGU-processed samples. (a) Black curve - absorption spectrum of SWCNT suspension in sodium deoxycholate after one pass through Microfluidizer interaction chamber at 8000 psi followed by 1 h centrifugation at 100000 × g. Red curve - spectrum SWCNT suspension in sodium deoxycholate processed by density gradient ultracentrifugation (DGU) to remove bundles. (b) – absorbance normalized photoluminescence spectra of corresponding

Microfluidizer-processed (red curve) DGU-processed (black curve) SWCNT suspensions.

In addition to a qualitative estimate of semiconducting SWCNT lengths with photoluminescence microscopy, AFM studies were performed to quantitatively assess SWCNT length distributions. AFM images and height profiles of more than 250 SWCNTs were analyzed (Figure 60) and the lengths of the features identified as individual SWCNTs (see Chapter 3 for the criterion) were recorded. Errors in length measurements were estimated to be up to 10%. Since possible error sources discussed in previous section were mostly attributed to length measurements of shorter SWCNTs, in shear-dispersed samples with generally greater average SWCNT lengths we expect these errors to be less significant.

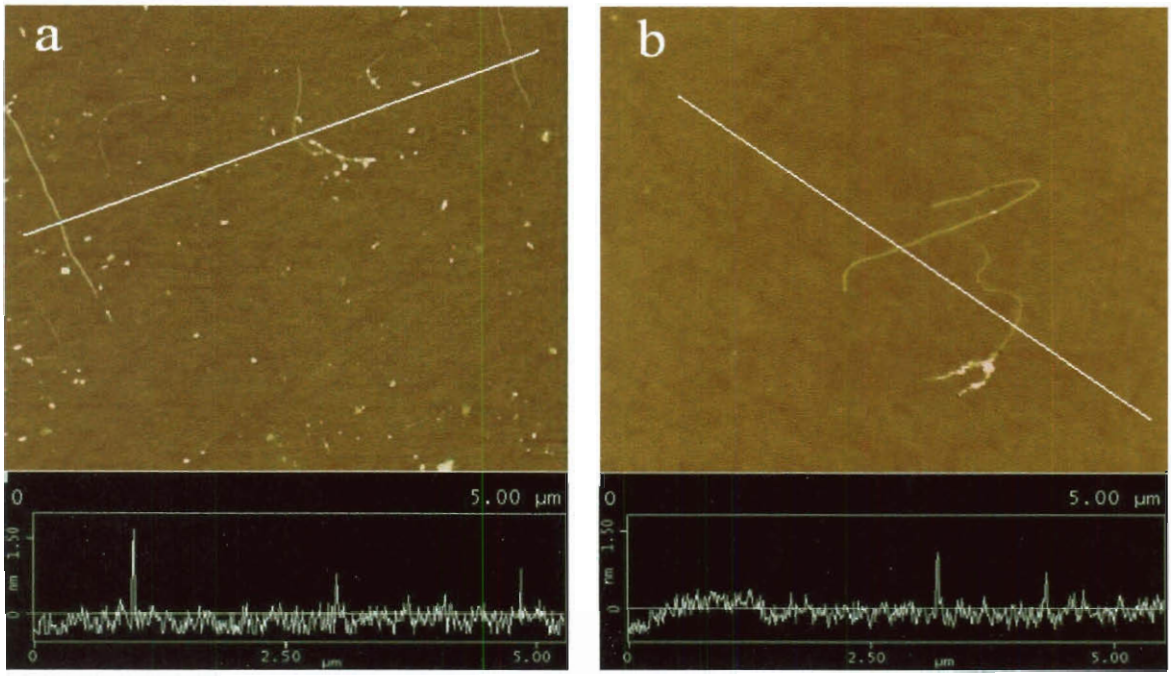

Figure 60. AFM images of shear-dispersed SWCNTs deposited on silicon substrate; height profile cross-sections along the white line are presented at the bottom. Cross-section in frame (a) shows 3 SWCNTs with heights of 1.55 nm, 0.96 nm and 0.81 nm from left to the right. Cross-section in frame (b) shows 2 SWCNTs with heights of 1.26 and 0.96 nm from left to right.

SWCNT length histograms (Figure 61) constructed from AFM measurements confirm that shear-dispersed samples are highly abundant in longer SWCNTs. The mean lengths for SDBS and sodium deoxycholate dispersed samples were 0.76 and 0.79 µm respectively. It was also calculated that in both surfactants 20% of SWCNTs were longer than 1 µm (Figure 61a and b). Those SWCNTs supply nearly 50% of all nanotube carbon atoms in the sample, as deduced from the length dependence of relative nanotube carbon content (Figure 62a and b). This result illustrates significant enrichment of

Microfluidizer-dispersed SWCNT suspensions in individualized SWCNTs over one micrometer long that can be further used in a number of applications. These studies also indicate that shear-assisted dispersion provides an efficient way to suspend individual SWCNTs without damaging and cutting them with ultrasonication.

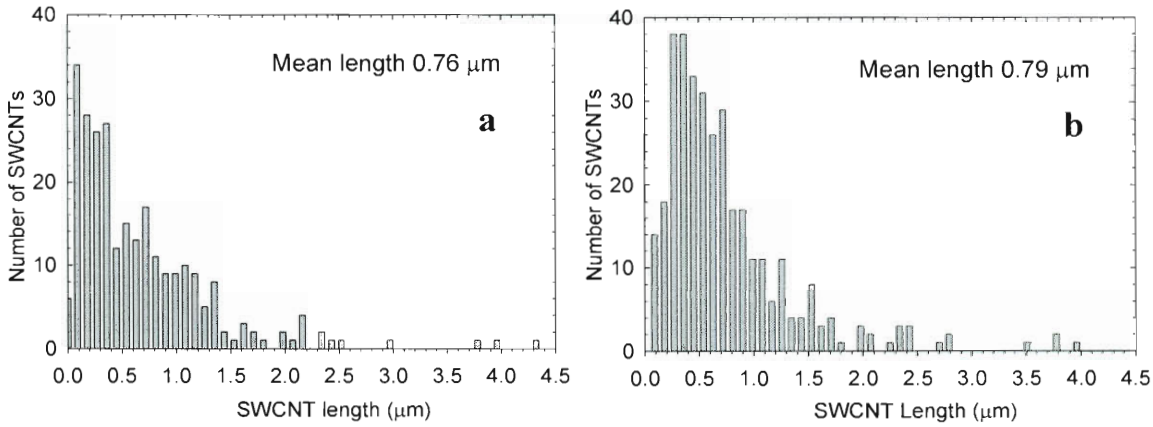

Figure 61. AFM length histograms for SWCNTs shear-dispersed in aqueous SDBS (a) and aqueous sodium deoxycholate (b) in the Microfluidizer interaction chamber at 8000 psi.

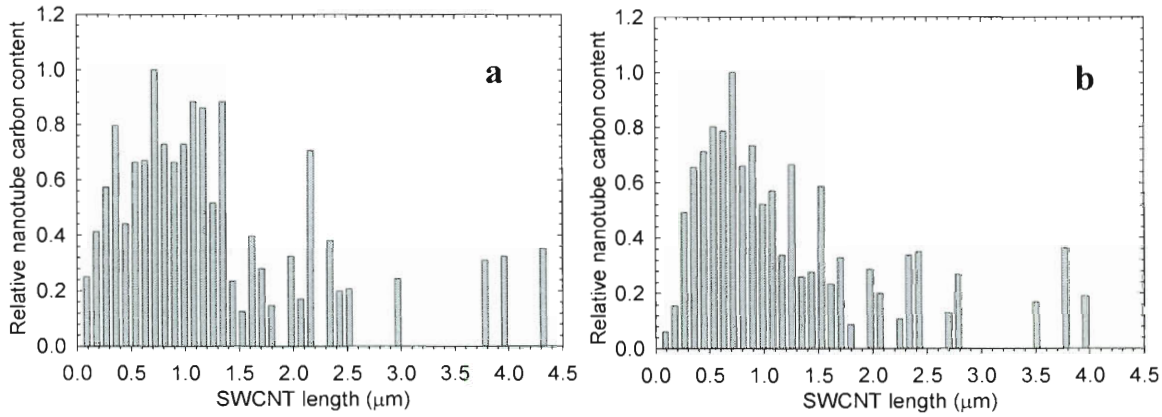

Figure 62. Length dependence of the relative SWCNT carbon content found as a product of the number of SWCNTs, SWCNT length, and the number of carbon atoms per

unit length for the samples shear-dispersed in aqueous SDBS (a) and aqueous sodium deoxycholate (b) in the Microfluidizer interaction chamber at 8000 psi.

5.3.3. Ultrasonication-assisted length fractionation

Length dependence of SWCNT optical properties was further investigated using fractions created by ultrasonication-induced scission. For that purpose, SWCNTs were suspended in 1% aqueous SDBS via shear-assisted dispersion, which prevents sonication-induced shortening in the preparation procedure. After that, the suspension was subjected to up to 420 minutes of ultrasonic bath agitation intended to induce SWCNT scission. At certain time intervals during the ultrasonication, fractions of the main sample were analyzed for SWCNT length distribution and optical properties. AFM and photoluminescence microscopy imaging revealed that as the sonication time increased, the lengths of SWCNTs in the images decreased substantially (Figure 63).

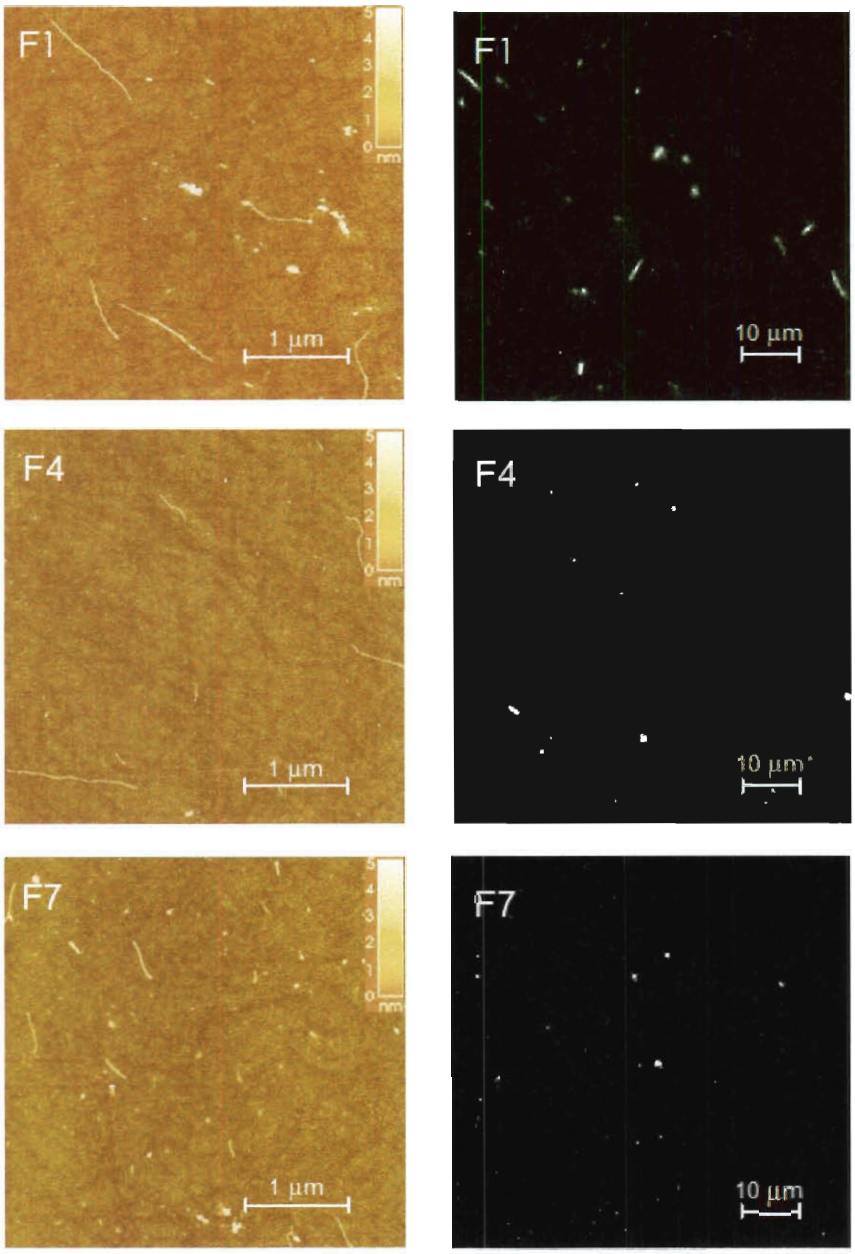

Figure 63. AFM and photoluminescence images of three SWCNT fractions bath ultrasonicated for 0 (F1), 150 (F4) and 420 (F7) minutes. Note: length scales on AFM and photoluminescence images differ by one order of magnitude.

Due to its higher resolution and ability to detect both semiconducting and metallic species, AFM was used to construct the length distributions for a number of SWCNT

fractions (Figure 64). These length distributions, based on the analysis of more than 1000 SWCNTs total, show a significant shape change and a strong inverse dependence of mean SWCNT length on sonication time (Figure 64). That correlation supports the hypothesis of SWCNT scission in the process of ultrasonication and provides a quantitative estimate of how such shortening depends on ultrasonication conditions.

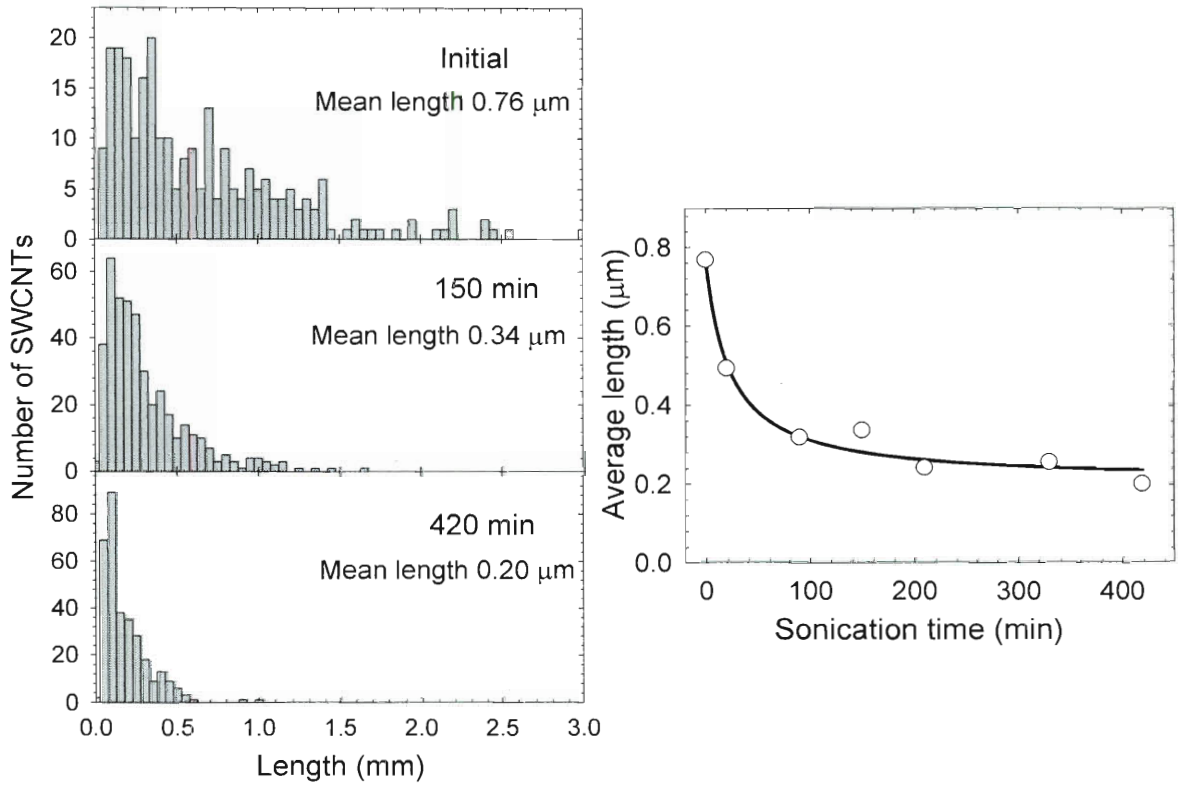

Figure 64. AFM analyses of ultrasonication-induced SWCNT length shortening. Left panel - AFM length histograms of SWCNT samples ultrasonicated for 0, 150 and 420 minutes. Right panel– dependence of average length of SWCNTs in the sample, determined by AFM analysis, on sonication time.

Absorption studies of sonicated fractions (Figure 65a) indicate an increase in the absorption background with sonication time. That may be explained by irreversible changes introduced into the structure of SWCNTs or surfactant by sonication, as suggested in the previous chapter. A change in photoluminescence intensity with sonication was also observed (Figure 65b).

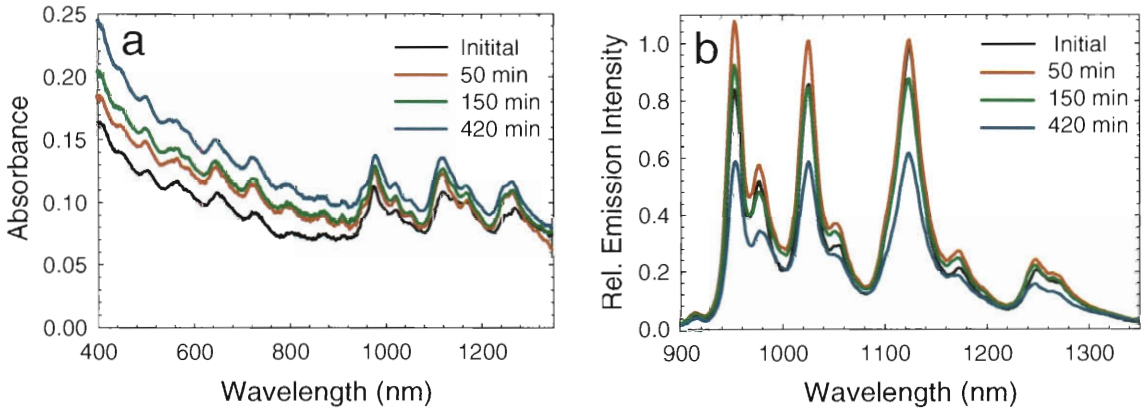

Figure 65. Absorption (a) and photoluminescence (b) spectra of SWCNTs dispersed in 1% aqueous SDBS via shear processing sonicated for 0 (black curve), 50 (red curve), 150 (green curve) and 420 (blue curve) minutes in the bath sonicator.

To visualize these trends we have plotted (Figure 66) absorption and photoluminescence signals integrated between 924 nm and 978 nm (the brightest 954 nm peak feature in the photoluminescence spectrum). A certain baseline obtained from sonication of the pure aqueous surfactant for the same periods of time was subtracted from the 924 nm – 978 nm absorption interval to compensate for sonication-induced background rise.

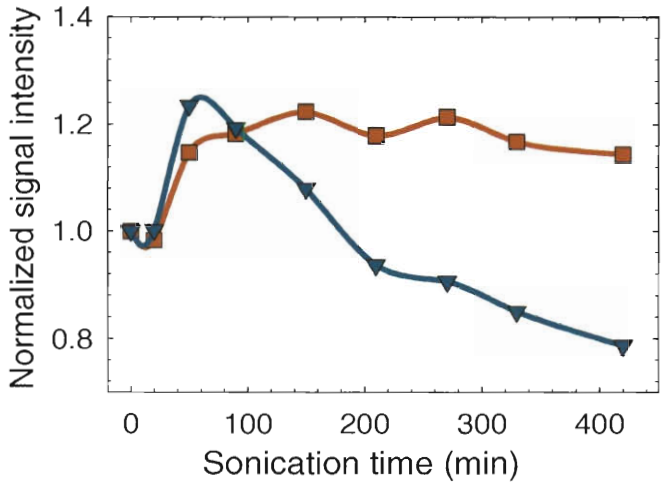

Figure 66. Ultrasonication time dependence of normalized background corrected integral absorbance (red squares) and normalized integral photoluminescence (blue triangles) of 924 nm – 978 nm feature.

As a result, both absorption and, especially, photoluminescence initially increase (Figure 66), likely due to further disaggregation allowing more efficient emission and increasing the number of individual absorbing SWCNTs (in large SWCNT clusters some of them might have been shielded by other absorbing species). However after 50 minutes the photoluminescence exhibited a nearly linear decrease with sonication time. This change can be attributed to SWCNT shortening, showing that more sonicated fractions with shorter SWCNTs exhibit less efficient emission. Absorption, on the other hand, remained constant (Figure 66) and, therefore, did not depend on SWCNT length.

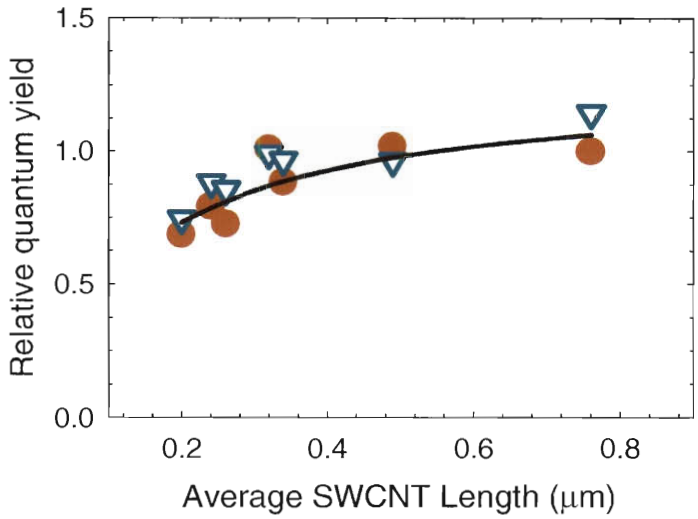

Figure 67. Dependence of experimentally obtained (red circles) and calculated (blue triangles) relative photoluminescence quantum yield on average SWCNT length in seven ultrasonicated fractions. The black line represents a simple hyperbolic fit to the data.

The information in Figure 66 was further used to show the length dependence of SWCNT relative quantum yield (red circles in Figure 67), calculated for each fraction as the ratio of photoluminescence to absorbance. This plot can be further compared to quantum yield of electrophoretically length-separated SWCNT fractions (Figure 62). In contrast to a previous prediction,[43] both figures show a gradual non-exponential increase with SWCNT length to apparent saturation. This trend, confirmed by two different experiments, can be further used as a reference for other measurements or theoretical modeling.

5.3.4. Quantum yield modeling

Since in the process of ultrasonication-induced length fractionation, the concentration of SWCNT material did not change from fraction to fraction, these samples were used for modeling the dependence of quantum yield on SWCNT length. Such a model can be compared to experimental results in Figure 67 in order to estimate excitonic properties such as mean exciton excursion length.

In the model, the quantum yield was estimated from the probability of exciton excursion along the nanotube without reaching SWCNT ends and quenching. As a first step, SWCNT length distributions (Figure 64) were constructed for all 7 sonicated fractions and approximated with log normal fits (Eq 5). Fit parameters listed in Table 3 were further used in the calculation of an average SWCNT photoluminescence quantum yield.

$$\mathbf{L}(x) = \frac{1}{\sqrt{2 \cdot \pi} \cdot \sigma \cdot x} \cdot \exp\left[\frac{-(\ln(x) - \ln(\mu))^2}{2 \cdot \sigma^2}\right] \qquad \text{(Eq 5)}$$

Table 3 – Lognormal fit parameters for nanotube length distributions in sonicated SWCNT suspensions.

Fraction #	Sonication time, min	Dataset size	<L>, μm	σ	μ	$<L_{fit}>$, μm
1	0	264	0.76	1.10	0.516	0.94
2	20	145	0.49	0.889	0.239	0.35
3	90	174	0.32	0.827	0.252	0.35
4	150	430	0.34	0.859	0.237	0.34
5	210	480	0.24	0.687	0.179	0.23
6	330	496	0.26	0.675	0.168	0.21
7	420	322	0.20	0.754	0.132	0.18

An estimate of the average quantum yield was provided by the integral, Q(λ) (Eq. 6) of the product of I(L, λ) and PDF(L), where I(L, λ) is the relative emission intensity of a SWCNT calculated (see Appendix) in accordance with the model of exponential exciton quenching at the SWCNT ends[186] and λ is the exciton excursion range. PDF(L) is a log normal probability density function describing SWCNT lengths in a particular fraction (Eq. 5). The integral was calculated numerically using limits that cover a relevant length range (in this case 0 to 20 μm).

$$Q(\lambda) = \int_0^{20} I(L,\lambda)\cdot PDF(L)\,dx = \int_0^{20}\left(1-2\cdot\frac{\lambda}{L}\cdot\frac{\sinh\left(\frac{L}{2\cdot\lambda}\right)}{\cosh\left(\frac{L}{2\cdot\lambda}\right)}\right)\cdot\left[\frac{1}{\sqrt{2\cdot\pi}\cdot\sigma\cdot L}\cdot\exp\left[\frac{-0.5\cdot(\ln(L)-\ln(L_0))^2}{\sigma^2}\right]\right]\cdot dL \quad \text{(Eq. 6)}$$

Using the value of the mean exciton excursion range parameter λ = 90 nm from previous experimental work[68] it was possible to find the estimated quantum yield for each SWCNT fraction. However, in our experiments that involved extensive sonication treatment λ could be somewhat different. In order to obtain a realistic estimate of the exciton excursion range, we used the integrals computed for every SWCNT fraction to construct the dependence of calculated quantum yield on average SWCNT length. Then, a λ value was found for which this calculated quantum yield (blue triangles in Figure 67) matched experimentally obtained values (red circles in Figure 67). This excursion range of 30 nm appeared to be less than 90 nm reported for highly luminescent SWCNTs.[68] However, since the SWCNTs used in our work have undergone extensive ultrasonication treatment, they are expected to have a greater numbers of defects, which may induce

additional exciton quenching (Chapter 2) and decrease the mean excursion range down to 30 nm. The estimate of mean exciton excursion range found in this work gives an important insight on excitonic behavior in SWCNTs and can be further used to quantify trends in exciton lifetimes.

5.4. Summary

In this chapter we have studied the length dependence of SWCNT optical properties. During that process we also explored a novel SWCNT suspension preparation technique based on shear-assisted microfluidic dispersion. Nanotube suspensions obtained by shear processing appeared to be well dispersed and disaggregated. After one processing cycle, average lengths of SWCNTs in aqueous SDBS and sodium cholate surfactants were found to be 0.76 and 0.79 μm respectively. That indicates a greater abundance of longer individualized SWCNTs in shear-processed samples as compared to suspensions prepared with the aid of tip sonication.

Starting SWCNT samples dispersed by ultrasonication and shear processing were further length-fractionated using electrophoretic separation and ultrasonication-induced SWCNT scission. Optical properties of length-specific fractions obtained by these two methods were compared. It was found that both sets of fractions exhibited qualitatively similar gradual increases in relative photoluminescence quantum yield with average SWCNT length. Absorption spectra of ultrasonicated fractions corrected for sonication-induced surfactant scattering backgrounds showed no significant variations. Modeling of length-dependent quantum yields allowed us to estimate mean exciton excursion length

of 30 nm for SWCNTs processed with excessive ultrasonication. That information may be further used to characterize exciton photophysics.

CHAPTER 6

Graphene oxide photoluminescence

6.1 Introduction

6.1.1 Introduction to graphene

Since its discovery,[16] graphene has became one of the leading topics in modern nanotechnology research. It can be considered as a building block for many carbon structures such as carbon nanotubes or graphite and possesses a number of unique properties. Structurally, graphene is represented by a monolayer of sp^2-hybridized carbon atoms in a honeycomb lattice (Figure 68). Tight binding calculations indicate that the graphene band structure (Figure 69) dictated by its 2-dimentional spatial configuration is characteristic of a gapless semiconductor (or a semi-metal).[187] Its valence and conduction bands touch, but, since the Fermi level passes through the intersection point (Figure 69), ideally all the electrons are situated in the valence band. However, even a small perturbation can promote electrons into the conduction band, turning graphene into a conductor.

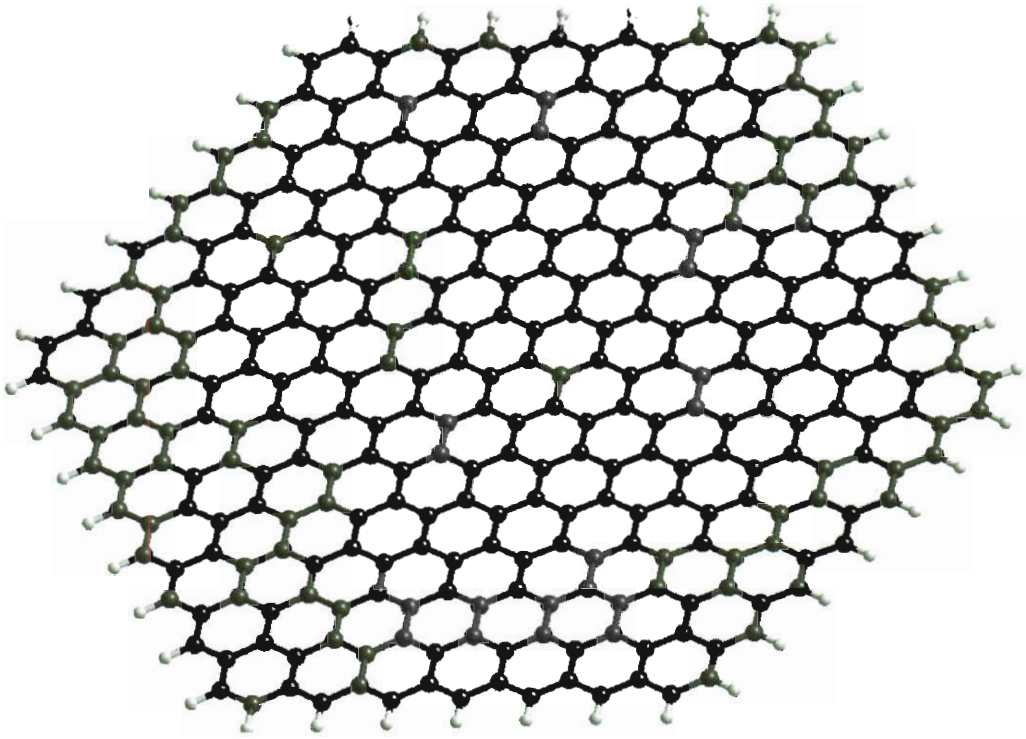

Figure 68 – A single graphene sheet.

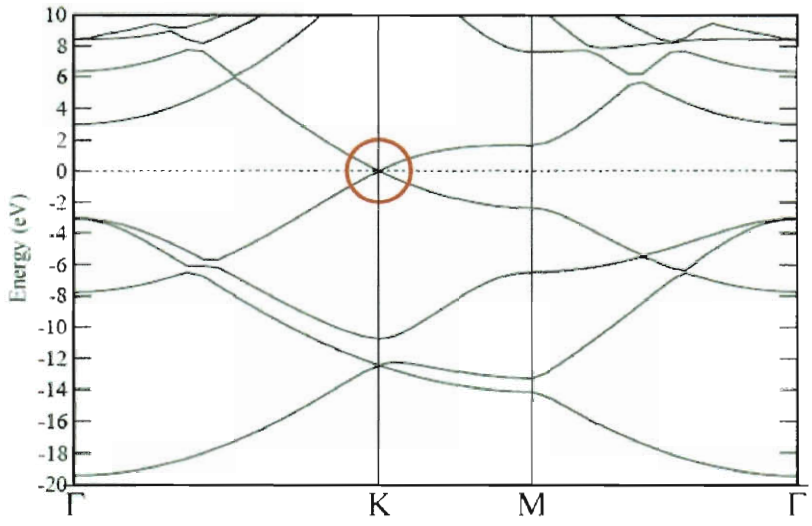

Figure 69 – Electronic band structure of graphene from tight binding calculation.[187]

6.1.2 Preparation and characterization

The most widely used methods to produce graphene are micromechanical exfoliation and epitaxial growth. The micromechanical approach[16] is based on a separation of graphene layers from a solid graphite piece with adhesive tape. Since these layers are only weakly bound to each other, a stronger van-der-Waals interaction between the carbon layer and the tape can detach down to a single graphene sheet. The epitaxial growth method is often based on the high-temperature (>1100 °C) reduction of silicon carbide interface to a multilayered graphene.[188] It is also possible to grow graphene similarly to SWCNTs by chemical vapor deposition (CVD) on a catalytic metal surface.[189] Other graphene synthesis methods include reduction of graphene oxide flakes,[190] pyrolysis of sodium ethanol with further sonication,[191] and growth from solid carbon sources such as polymers or even single molecules.[192]

As-produced graphene can be further structurally characterized using optical, atomic force or Raman microscopy. In the optical microscope on specific substrates (such as 300 nm SiO_2 on Si) single to few layer flakes can be distinguished from multi-layer ones by the change in the interference color from added optical thickness.[16,193] AFM can be used to directly assess the number of layers through height profiles. However the small difference in thickness between single and bilayer graphene can be observed only if the flakes contain folds or wrinkles.[16,193] Raman spectroscopy can be efficiently utilized to characterize graphene structure due to the change in shape, width and position of the 2D Raman band with the number of layers.[194] TEM and electron diffraction analyses can also be employed; however those are laborious and require specific orientation of graphene flakes.[194]

6.1.3 Properties and applications

Graphene is known for its exceptional electronic structure. Due the to linear energy dispersion relation near the Dirac points, where the valence and conduction bands touch (Figure 69), electrons in graphene behave like massless fermions. This peculiarity results in a number of unique properties such as nearly ballistic transport and high carrier mobility,[195,196] which are appealing for applications in nanoelectronics. Graphene has been used in transparent conductive electrodes for light-emitting devices[197,198] and photovoltaic cells,[199] and as an active medium in radio frequency-operated nanoscale field-effect transistors.[200-203] The large surface area and remarkable transport properties of graphene flakes were recently utilized in transistor-based biological sensors.[204]

Optical properties of graphene are also of great interest. However due to the absence of bandgap in unmodified graphene, it has mostly been used as an absorbing[205,206] medium and never as an active emitting element. Due to the importance of band gap effects in optoelectronic devices, several strategies have been used to open band gaps in graphene. One is based on reducing the dimensionality to 1D graphene nanoribbons[207-210] or 0D graphene quantum dots.[211,212] Those structures exhibit band gaps on the order of 0.5 to 2.5 eV due to quantum confinement; however, their optical properties are still being investigated. Another way of opening a band gap is chemical functionalization. Functionalized derivatives such as fluorinated graphene[213] or graphene oxide[214] have shown to acquire a variable band gap depending on the substituent coverage or degree of oxidation/reduction. This allows tailoring the band gap of the derivatized graphene for specific needs.

6.1.4 Graphene oxide

Graphene oxide (GO) is one of the most promising forms of modified graphene. It can be easily obtained by direct dispersion of graphite oxide (discovered in 1859 [215]) in basic aqueous solutions, where oxidized layers separate.[216] The general structure of graphene oxide is similar to pristine graphene, however, due to functionalization, a number of carbons in GO flakes reside in sp^3-hybridized form with attached oxygen-containing groups.

Its optical properties make GO appealing for different applications in optoelectronics.[217] It was recently shown that dispersed GO exhibits pronounced absorption and photoluminescence in the visible and near-IR.[214,218,219] Photoluminescence was attributed to localization of sp^2 domains by derivatized sp^3 sites creating small confined π-system regions. Such a scenario was also suggested by several theoretical studies.[220-222] Another experimental report[223] advocated the idea that GO photoluminescence occurs due to "CO"-related electronic states at the derivatization sites. This chapter describes a study of the pH-dependence of GO photoluminescence and the origins of its quasi-molecular emission in basic environments. Our findings can be used for modulating the GO emission in optoelectronic devices and chemical sensors.

6.2 Experimental

Two batches of graphene oxide obtained from different sources were used in our experiments. A first batch named expandable GO (EGO) was produced from Expandable Graphite (Intumescent Flake Graphite, from Asbury Carbons) by thermal exfoliation at

700°C for 1 min followed by modified Hummer's method.[224,225] The majority of experimental studies were conducted with the second batch of graphene oxide named natural GO (NGO) that was obtained by oxidizing natural graphite powder (SP-1 graphite, from Bay Carbon Corporation) according to modified Hummers method. Both batches of GO produced in Prof. Ajayan's laboratory at Rice University were then dispersed in water at concentrations of ~0.1 mg/mL by 30 min bath sonication and 10 min tip sonication at 5 W. As a result a clear suspension was formed with no visible signs of aggregation. This suspension was then divided into 10 mL portions that were spiked with aliquots of H_2SO_4 or dilute KOH to individually modify their pH in the range of 0.9 to 12.7. After the pH adjustment, each sample was additionally tip sonicated for 5 min at 5 W to reduce possible aggregation effects from rapid pH change.

The resulting suspensions of different pH were then studied optically. Their absorption spectra were recorded using a Cary 4000 UV-Visible spectrophotometer in the wavelength range of 200 to 900 nm. Photoluminescence excitation and emission spectra of each suspension were recorded in the visible using a J-Y Spex Fluorolog spectrofluorometer (Figure 14) at 3 nm detection step size and 6 s integration with correction for detector response and excitation power. A 440 nm lamp excitation wavelength was used together with a 455 nm long-pass emission filter that eliminated scattered excitation light. A blank water spectrum was also subtracted to account for water Raman. FTIR spectra were measured using a Nicolet FTIR Microscope in the ATR mode with an MCT/A detector. The solid samples of highly basic and highly acidic GO used for FTIR measurements were prepared by sedimentation of GO from suspensions

with either high or low pH by 20 minutes of centrifugation at 13,000 × g. After that procedure the pellet was collected, dried and used for FTIR studies.

Theoretical modeling of graphene sheet containing 240 carbon atoms was performed using semi-empirical (PM3) quantum calculations in HyperChem 7 software.

6.3 Results

Photoluminescence spectra of NGO suspensions were studied as a function of pH. At acidic pH we observed a broad emission peak centered around 660 nm (Figure 70a) similar to the one reported previously.[214,218,219,223] During the stepwise increase of pH, up to the value of 7.6, the intensity of this acidic peak monotonically decreased, and near the pH 8, new features around 500 nm started rapidly emerging. At higher pH (Figure 70b) these sharper (FWHM ~ 20 nm) features at ~482 and 510 nm became more prominent and the broad acidic peak became suppressed completely. In order to correctly describe the observed spectra, they were fitted with a number of Gaussian components. As a result, the acidic feature was approximated with five peaks centered at 479, 506, 531, 577, and 683 nm, whereas basic peaks were adjusted down 479 and 506 nm.

The abrupt appearance of sharp basic features at ~pH 8 resembled a spectrophotometric titration. Therefore, to illustrate the dynamics of observed changes, titration curves were constructed with respect to pH for one acidic (683 nm) and two basic peaks (Figure 70c). Those show a sharp inflection point at pH 8 for both basic features and a gradual monotonic decrease of acidic peak intensity with pH. These spectral variations were reversible indicating that no deoxygenation (reduction) has

occurred,[226] and therefore suggesting a simple protonation/deprotonation of oxidized species.

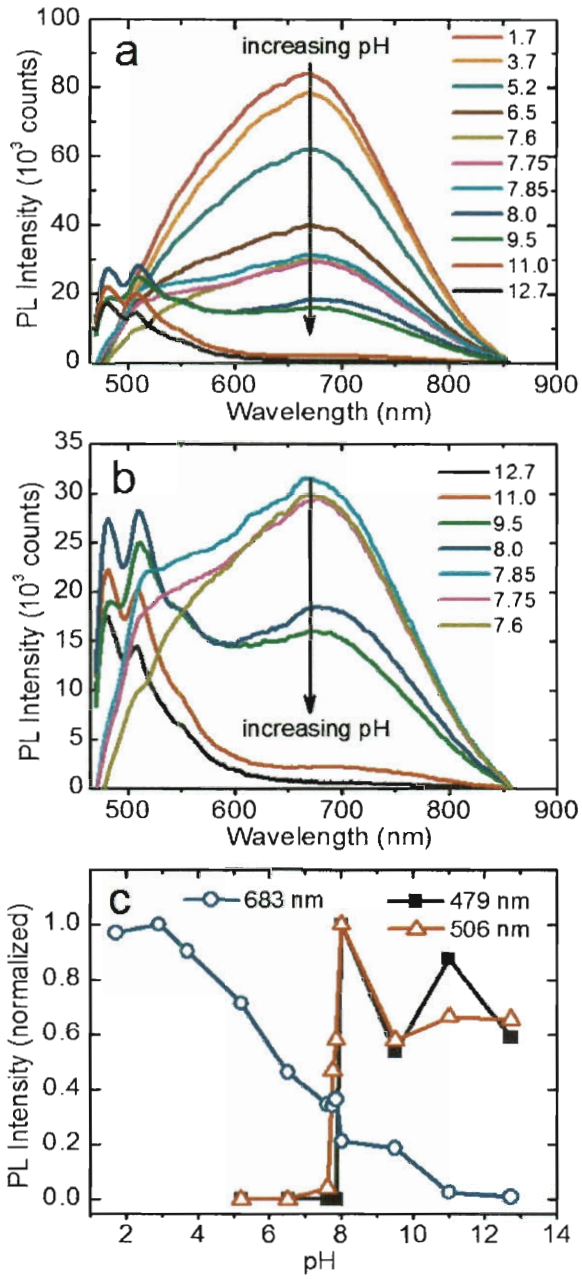

Figure 70. pH-dependent photoluminescence of NGO. a – photoluminescence spectra taken with 440 nm excitation in the pH range of 1.7 to 12.7. b – photoluminescence spectra in the basic pH range from 7.6 to 12.7 plotted on expanded

scale. c – Photoluminescence intensities of basic (479 and 506 nm), and acidic (683 nm) features plotted with respect to pH.

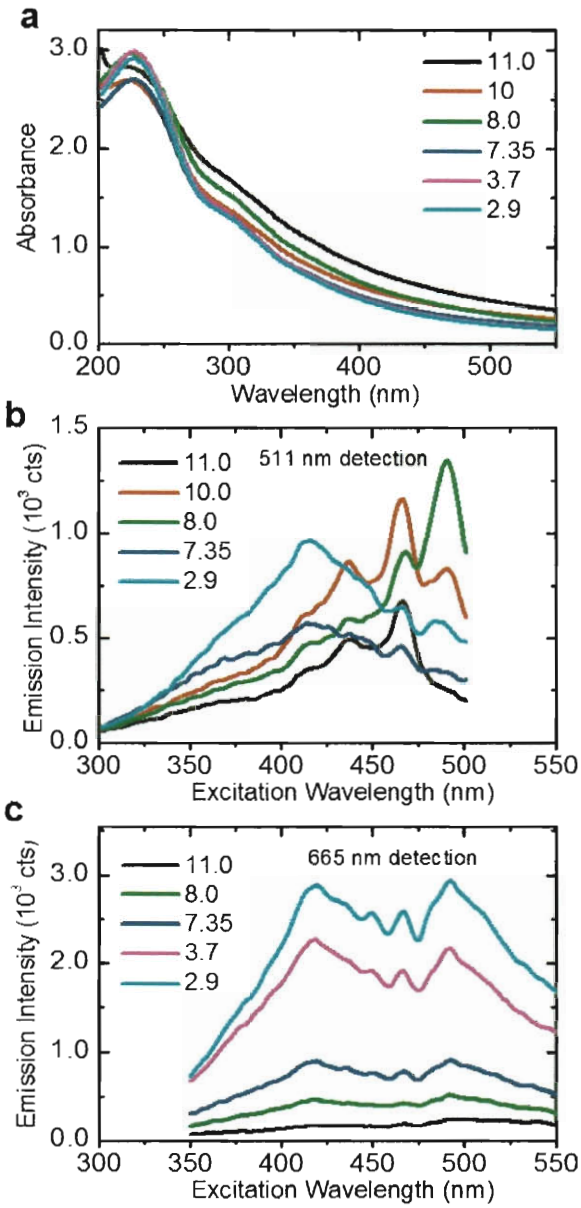

Figure 71. Absorption and excitation spectra of NGO. a – absorbance spectra measured between pH 2.9 and 11. b – excitation spectra for the basic peak at 511 nm. c – excitation spectra for the acidic peak at 665 nm.

Absorption spectra of pH-adjusted suspensions show a strong π-plasmon peak near ~230 nm tailing into the visible part of the spectrum (Figure 71a). The tail was more intense at basic pH. However, no prominent features were observed at the positions of photoluminescence peaks, which signifies that the major absorbing species are not directly responsible for the emission in the visible. In order to further characterize the photoluminescence process, excitation spectra of NGO suspensions were taken at different pH. Unlike absorption, those show pronounced features for both basic (Figure 71b) and acidic (Figure 71c) peak excitation. Even though the spectral shapes in Figures 71b and 71c are quite different, the peak positions appear to be nearly identical, suggesting that the ground state is the same for both acidic and basic species.

EGO has shown similar broad photoluminescence at acidic conditions and molecularly sharp spectrum in the basic regime (Figure 72a). However, only one emission peak was observed at basic pH. Titration curves (Figure 72b) constructed for acidic and basic features indicate that acidic peak intensity has gradually decreased with pH while the basic peak started emerging at ~pH 6. Similarities in the positions of spectral features and their pH dependent behavior in two different forms of GO suggest that the effect originates from oxygen-containing groups.

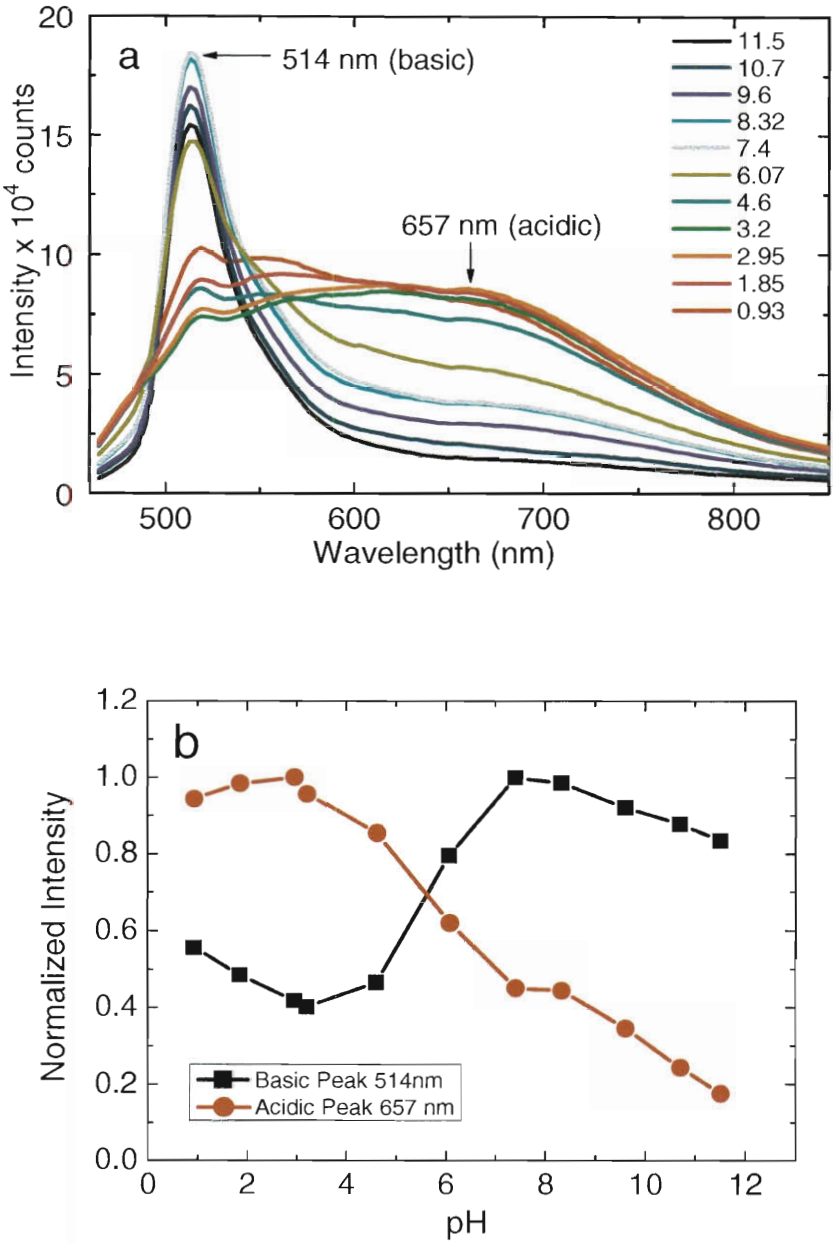

Figure 72. Photoluminescence emission from EGO. a – emission spectra taken with 440 nm excitation in the pH range of 0.93 to 11.5. b – photoluminescence intensities of acidic (657 nm) and basic (514 nm) features as a function of sample pH.

6.4 Data analysis and interpretation

Even though GO is a non-stoichiometric material that assumes different structural forms, sharp photoluminescence in the basic regime observed in both NGO and EGO strongly resembles the emission from polycyclic aromatic molecules.[227,228] For example, the excitation and emission spectra of EGO at the basic pH plotted in the same graph (Figure 73a), look like closely spaced mirror images of each other. This is usually a characteristic of molecular excitation/emission spectra that are Stokes-shifted from the original transition frequency located in the middle between those peaks.[229] However in the case of NGO, the pH dependence of excitation and emission reveals somewhat more complex structure. We note that in Figure 72 b the excitation spectrum of the 511 nm feature at pH 8 has a peak at 491 nm, which appears to be at a greater wavelength than the emission peak of 479 nm (Figure 70b) observed with 440 nm excitation at pH 11. The occurrence of strong emission peaks at a shorter wavelength than the excitation of other spectral features indicates the presence of more than one fluorophore. This is illustrated in Figure 73b as a pair of mirror image spectra at pH 8 and 11 that appear to have different origins (A and B). Furthermore, we note that even though the origin A is observed in both NGO and EGO, the fluorophore with the origin B is only present in NGO. This also suggests the existence of multiple fluorophores in NGO.

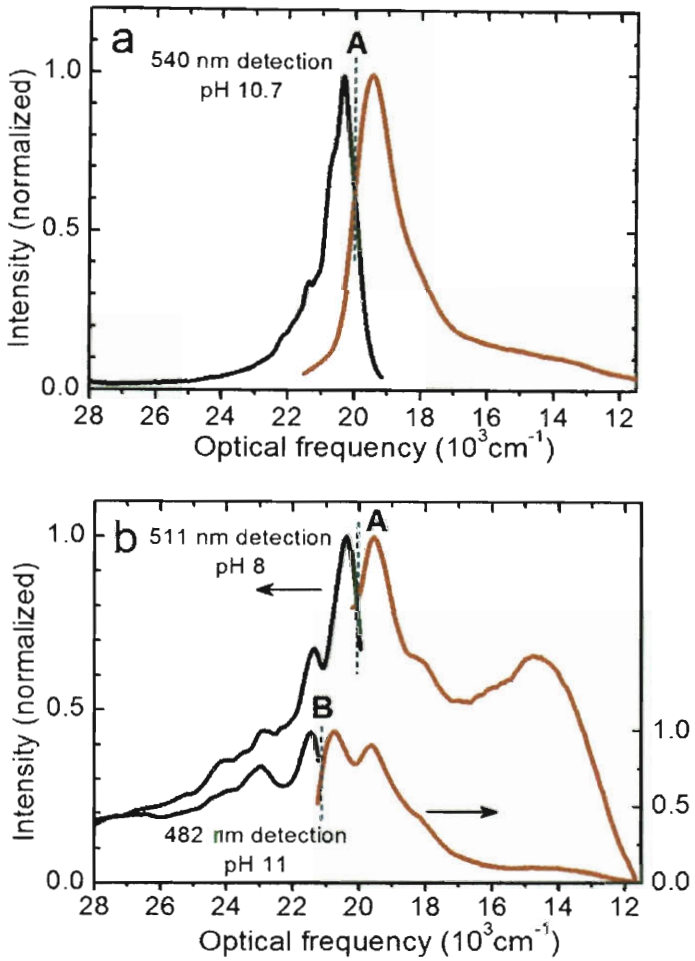

Figure 73. Combined excitation and emission spectra of graphene oxide. a – normalized excitation and emission spectra of EGO at pH 10.7 (with origin A). Photoluminescence was excited at 440 nm and the excitation spectra taken with 540 nm detection. b – normalized excitation and emission spectra of NGO at pH 8 (with origin A and scale on the left axis) and pH 11 (with origin B and scale on the right axis). Photoluminescence was excited at 440 nm and the emission spectra were collected with detection at 511 nm for trace A and 482 nm for B.

In order to deduce the origin of quasi-molecular emission in the basic regime, we have studied the pH-dependent behavior of oxygen-containing functional groups.

Vibrational absorption spectra of NGO in acidic and basic conditions (Figure 74a and b) obtained by ATR-FTIR measurements point to a number of bands corresponding to several possible addends including COOH, COO^-, C-OH, C-H, and C=O (see Fig. 74 caption for the vibrational frequencies).[230] However only a few of them exhibit protonation/deprotonation in the pH range of 6-8, where the largest variations of GO photoluminescence were observed.

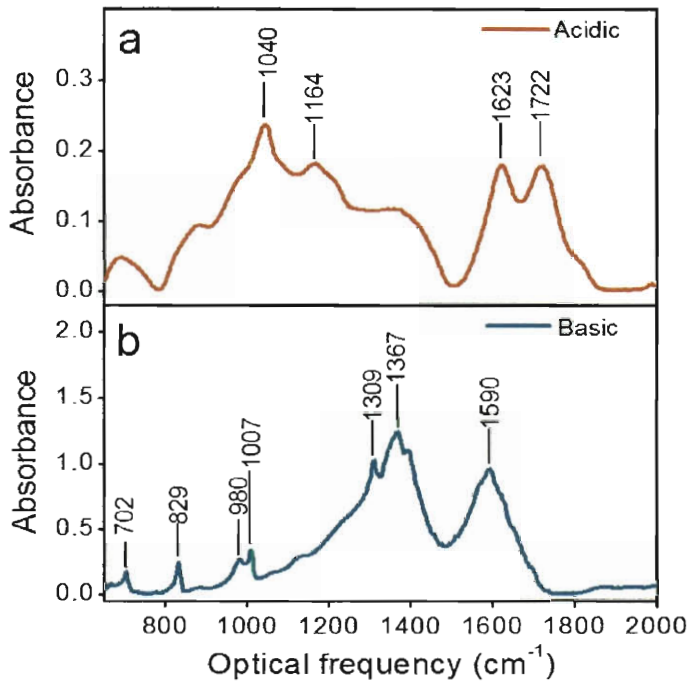

Figure 74. Vibrational absorption spectra of graphene oxide. ATR-FTIR spectra of solid GO samples isolated from **a.** acidic and **b.** basic aqueous suspensions. Major bands and proposed assignments in **a.**: 1040 cm^{-1} (C-O stretch) , 1164 cm^{-1} (C-OH stretch), 1623 cm^{-1} (adsorbed water & skeletal vibrations of unoxidized graphitic domains), 1722 cm^{-1} (C=O stretch); in **b.**: 829 cm^{-1} (C-H out-of-plane wag), 980 cm^{-1} (possibly epoxide stretch), 1007cm^{-1} (C-H in-plane bend), 1309 cm^{-1} (C-O stretch), 1367

cm^{-1} (COO^- symmetric stretch), 1590 cm^{-1} (COO^- antisymmetric stretch or a carbon ring mode).

Among the possible addends, the closest candidate for our experimental conditions is the COOH group in polyaromatic carboxylic acids, whose pKa is increased due to the neighboring π-system. In addition, we note that several aromatic carboxylic acids such as pyrene-3-carboxylic acid (3-PCA),[230] pyrene-1-carboxylic acid (1-PCA)[231] and anthracic acids (9-AC, 1-AC, and 2-AC)[232,233] have shown structured mirror-image excitation/emission spectra at basic pH and broad red-shifted photoluminescence at acidic conditions, similarly to GO. The pKa of those acids in the ground state is still too low to be in the range of 6-8. However, in the excited state it is increased by approximately 1.5 to 5 units (3.8 vs. 5.2 for 3-PCA,[230] 4.0 vs. 8.7 for 1-PCA,[231,234] 3.0 vs. 6.5 for 9-AC[232,233]). In addition, a large red shift observed in GO between the excitation (Figure 71c) and emission (Figure 70a) at acidic conditions suggests possible protonation in the excited state.[235,236] In such a scenario, both basic and acidic forms of GO would start with COO^- species in the ground state, which is consistent with the previous observation in section 6.2 that the ground state configuration of GO is the same for both acidic and basic environments. In the excited state when pH drops below 8, COO^- groups would be protonated, which may explain the sudden intensity loss of the basic spectral features in that pH region.

6.5 Theoretical modeling

The observed emission characteristics suggest that GO photoluminescence arises from quasi-molecular, pH-sensitive fluorophores. Such fluorophores resemble polyaromatic carboxylic acids, which in GO may be represented by small regions of graphitic carbon coupled to COOH groups. To investigate this possibility we have performed semi-empirical (PM3) quantum calculations on graphene sheet fragments containing 241 carbon atoms and one COO^- group at the edge (Figure 75a).

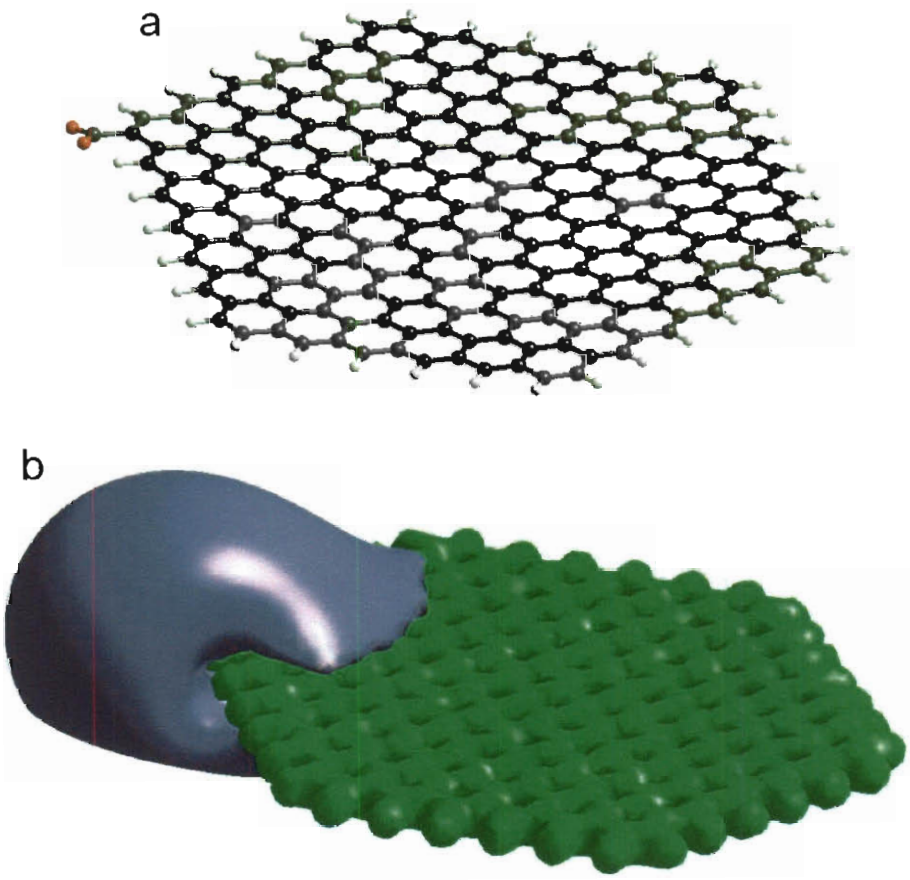

Figure 75. Molecular modeling images. a – modeled graphene fragment containing 241 atoms with COO^- addend group at the edge. b – semi-empirical quantum

chemical calculation of electrostatic potential on the fragment performed using the PM3 method. The purple isosurface, enclosing the COO^- group, represents the region in which the negative potential value exceeds 0.06 e/a_0.

This structure is intended to model local functionalization sites in basic conditions where the structured sharp emission from GO was observed. The results of the modeling indicate that addends create a surrounding region of negative electrostatic potential (Figure 75b), which we interpret as a range of strong electronic coupling between the graphene fragment and the functional group. This region is not sharply defined, as it depends on the choice of electrostatic potential. However it seems largely confined to a section containing approximately 34 carbon atoms (13 hexagonal rings). We note that if compared to emission from polyaromatic carboxylic acids, the experimentally observed sharp transitions in GO basic spectra would correspond to a molecule containing approximately 50 π-electrons,[237] which is in reasonable agreement with the size of the region carved out in Figure 75b by the negative electrostatic potential. Based on the modeled GO fragment, we preformed a crude calculation of allowed optical transitions that showed a number of singlet features between 450 and 550 nm and fewer transitions between 650 and 750 nm (Figure 76). This is reasonably consistent with our experimental observations of GO emission. In order to provide a more detailed description of the electronic transitions arising from graphitic regions coupled with oxygen-containing addends, more refined quantum mechanical calculations may be required.

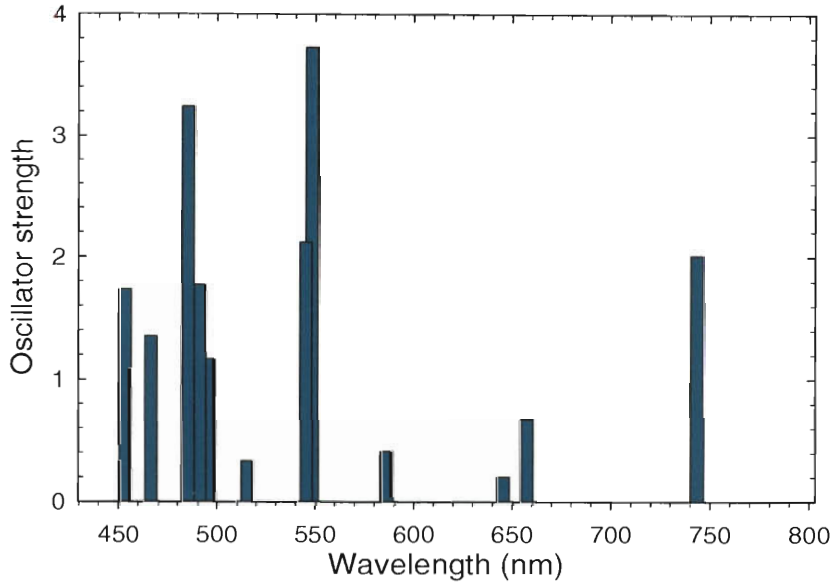

Figure 76 – Calculation of oscillator strength of singlet optical transitions for graphene oxide fragment in Figure 74a.

6.6 Summary

In a series of experiments strong visible photoluminescence was observed from aqueous dispersions of graphene oxide. The shape, position and intensity of emission features depends strongly on pH, with narrow structured spectra near 500 nm in basic conditions and a broad red-shifted peak at ~ 660 nm in the acidic regime. These reversible spectral changes are characteristic of quasi-molecular emission from fluorophores that undergo excited-state protonation in acidic environments. IR vibrational spectroscopy together with analyses of excited state equilibrium constants suggest that these fluorophores are similar to polyaromatic carboxylic acids.

Semi-empirical quantum modeling of a graphene fragment with a carboxyl group

addend indicates a relatively distinct interaction region surrounding the functional group and enclosing approximately 34 carbon atoms. Based on our experimental and computational results we propose that even though GO is a highly disordered material with ill-defined chemical structure, the interaction regions with oxygen containing addends may form quasi-molecular fluorophores resembling polycyclic aromatic compounds.

The pH-dependent photoluminescence of graphene oxide may be applied in optoelectronic systems involving GO as an active medium or in microscopic pH sensors. More refined functionalization processes may further improve the homogeneity of addend-defined fluorophores in GO for future applications and fundamental studies.

APPENDIX

From ref. 186 we can infer that the time-independent form of the diffusion equation for the density of excitons on a SWCNT is:

$$D\cdot\left(\frac{d^2}{dx^2}N(x)\right)-\frac{N(x)}{\tau}+\sigma=0 \qquad \rightarrow \qquad \frac{d^2}{dx^2}N(x)-\frac{N(x)}{D\cdot\tau}=-\frac{\sigma}{D}$$

We solve this equation by variation of parameters method. First find the solution of the corresponding homogeneous equation:

$$\frac{d^2}{dx^2}N(x)-\frac{N(x)}{D\cdot\tau}=0$$

Those solutions take form

$$N(x)=A\cdot\exp\left(-\frac{x}{\sqrt{D\cdot\tau}}\right)+B\cdot\exp\left(\frac{x}{\sqrt{D\cdot\tau}}\right)$$

Then we represent A and B as functions of x (A(x) and B(x)) and solve the system of equations:

$$\left(\frac{d}{dx}A(x)\right)\cdot\exp\left(-\frac{x}{\sqrt{D\cdot\tau}}\right)+\frac{d}{dx}B(x)\cdot\exp\left(\frac{x}{\sqrt{D\cdot\tau}}\right)=0$$

$$\left(\frac{d}{dx}A(x)\right)\cdot\exp\left(-\frac{x}{\sqrt{D\cdot\tau}}\right)\cdot\left(-\frac{1}{\sqrt{D\cdot\tau}}\right)+\frac{d}{dx}B(x)\cdot\exp\left(\frac{x}{\sqrt{D\cdot\tau}}\right)\cdot\left(\frac{1}{\sqrt{D\cdot\tau}}\right)=-\frac{\sigma}{D}$$

$$\left(\frac{d}{dx}A(x)\right)\cdot\exp\left(-\frac{x}{\sqrt{D\cdot\tau}}\right)+\frac{d}{dx}B(x)\cdot\exp\left(\frac{x}{\sqrt{D\cdot\tau}}\right)=0$$

$$\left(\frac{d}{dx}A(x)\right)\cdot\exp\left(-\frac{x}{\sqrt{D\cdot\tau}}\right)\cdot\left(-\frac{1}{\sqrt{D\cdot\tau}}\right)+\frac{d}{dx}B(x)\cdot\exp\left(\frac{x}{\sqrt{D\cdot\tau}}\right)\cdot\left(\frac{1}{\sqrt{D\cdot\tau}}\right)=-\frac{\sigma}{D}$$

$$\left(\frac{d}{dx}A(x)\right)\cdot\exp\left(-\frac{x}{\sqrt{D\cdot\tau}}\right)+\frac{d}{dx}B(x)\cdot\exp\left(\frac{x}{\sqrt{D\cdot\tau}}\right)=0$$

$$\left(\frac{d}{dx}A(x)\right)\cdot\exp\left(-\frac{x}{\sqrt{D\cdot\tau}}\right)-\frac{d}{dx}B(x)\cdot\exp\left(\frac{x}{\sqrt{D\cdot\tau}}\right)=\frac{\sigma\cdot\sqrt{\tau}}{\sqrt{D}}$$

Let

$$\left(\frac{d}{dx}A(x)\right)\cdot\exp\left(-\frac{x}{\sqrt{D\cdot\tau}}\right)=x$$

$$\left(\frac{d}{dx}B(x)\right)\cdot\exp\left(\frac{x}{\sqrt{D\cdot\tau}}\right)=y$$

After this substitution, the system transforms into

$$x+y=0$$

$$x-y=\frac{\sigma\cdot\sqrt{\tau}}{\sqrt{D}}$$

$$x=\frac{\sigma\cdot\sqrt{\tau}}{2\sqrt{D}},\qquad y=-\frac{\sigma\cdot\sqrt{\tau}}{2\sqrt{D}}$$

Then

$$\frac{d}{dx}A(x)=\exp\left(\frac{x}{\sqrt{D\cdot\tau}}\right)\frac{\sigma\cdot\sqrt{\tau}}{2\sqrt{D}}$$

$$\frac{d}{dx}B(x)=-\exp\left(-\frac{x}{\sqrt{D\cdot\tau}}\right)\frac{\sigma\cdot\sqrt{\tau}}{2\sqrt{D}},$$

$$A(x)=\frac{\sigma\cdot\tau}{2}\cdot\exp\left(\frac{x}{\sqrt{D\cdot\tau}}\right)+C1$$

$$B(x)=\frac{\sigma\cdot\tau}{2}\cdot\exp\left(-\frac{x}{\sqrt{D\cdot\tau}}\right)+C2$$

As a result

$$N(x) = \frac{\sigma\cdot\tau}{2} + C1\cdot\exp\left(-\frac{x}{\sqrt{D\cdot\tau}}\right) + \frac{\sigma\cdot\tau}{2} + C2\cdot\exp\left(\frac{x}{\sqrt{D\cdot\tau}}\right) =$$

$$= \sigma\cdot\tau + C1\cdot\exp\left(-\frac{x}{\sqrt{D\cdot\tau}}\right) + C2\cdot\exp\left(\frac{x}{\sqrt{D\cdot\tau}}\right)$$

Then we introduce boundary conditions to solve for C1 and C2:

$$N(0) = 0 \qquad \sigma\cdot\tau + C1 + C2 = 0 \quad \rightarrow \quad C1 = -\sigma\cdot\tau - C2$$

$$N(L) = 0 \qquad \sigma\cdot\tau + C1\cdot\exp\left(-\frac{L}{\sqrt{D\cdot\tau}}\right) + C2\cdot\exp\left(\frac{L}{\sqrt{D\cdot\tau}}\right) = 0$$

After we substitute C1 into the second equation:

$$\sigma\cdot\tau + -\sigma\cdot\tau\exp\left(-\frac{L}{\sqrt{D\cdot\tau}}\right) - C2\cdot\exp\left(-\frac{L}{\sqrt{D\cdot\tau}}\right) + C2\cdot\exp\left(\frac{L}{\sqrt{D\cdot\tau}}\right) = 0$$

$$C2 = \sigma\cdot\tau\cdot\frac{1-\exp\left(-\frac{L}{\sqrt{D\cdot\tau}}\right)}{\left(\exp\left(-\frac{L}{\sqrt{D\cdot\tau}}\right) - \exp\left(\frac{L}{\sqrt{D\cdot\tau}}\right)\right)} \quad \rightarrow \quad C1 = -\sigma\cdot\tau - \sigma\cdot\tau\cdot\frac{1-\exp\left(-\frac{L}{\sqrt{D\cdot\tau}}\right)}{\left(\exp\left(-\frac{L}{\sqrt{D\cdot\tau}}\right) - \exp\left(\frac{L}{\sqrt{D\cdot\tau}}\right)\right)}$$

Constants C1 and C2 are then used in the equation for N(x)

$$N(x) = \sigma\cdot\tau + -\sigma\cdot\tau\cdot\exp\left(-\frac{x}{\sqrt{D\cdot\tau}}\right) - \sigma\cdot\tau\cdot\frac{1-\exp\left(-\frac{L}{\sqrt{D\cdot\tau}}\right)}{\left(\exp\left(-\frac{L}{\sqrt{D\cdot\tau}}\right) - \exp\left(\frac{L}{\sqrt{D\cdot\tau}}\right)\right)}\cdot\exp\left(-\frac{x}{\sqrt{D\cdot\tau}}\right) +$$

$$+ \sigma\cdot\tau\cdot\frac{1-\exp\left(-\frac{L}{\sqrt{D\cdot\tau}}\right)}{\left(\exp\left(-\frac{L}{\sqrt{D\cdot\tau}}\right) - \exp\left(\frac{L}{\sqrt{D\cdot\tau}}\right)\right)}\cdot\exp\left(\frac{x}{\sqrt{D\cdot\tau}}\right) =$$

$$= \sigma\cdot\tau\cdot\left[1-\exp\left(-\frac{x}{\sqrt{D\cdot\tau}}\right)-\frac{\left(1-\exp\left(-\frac{L}{\sqrt{D\cdot\tau}}\right)\right)}{\left(\exp\left(-\frac{L}{\sqrt{D\cdot\tau}}\right)-\exp\left(-\frac{L}{\sqrt{D\cdot\tau}}\right)\right)}\cdot\left(\exp\left(\frac{x}{\sqrt{D\cdot\tau}}\right)+\exp\left(-\frac{x}{\sqrt{D\cdot\tau}}\right)\right)\right]$$

When solved for N(x), we can find relative emission intensity, I(L) as the total exciton density on the SWCNT,

$$\int_0^L N(x)\,dx = \frac{\sigma\cdot\tau\cdot\left(L\cdot\exp\left(\frac{L}{\sqrt{D\cdot\tau}}\right)-2\sqrt{D\cdot\tau}\cdot\exp\left(\frac{L}{\sqrt{D\cdot\tau}}\right)+2\sqrt{D\cdot\tau}+L\right)}{\left(\exp\left(\frac{L}{\sqrt{D\cdot\tau}}\right)+1\right)}$$

normalized by the maximum total exciton density $\frac{\tau\cdot\sigma}{L}$:

$$I(L) = \frac{\left(\exp\left(\frac{L}{\sqrt{D\cdot\tau}}\right)-2\cdot\frac{\sqrt{D\cdot\tau}}{L}\cdot\exp\left(\frac{L}{\sqrt{D\cdot\tau}}\right)+2\cdot\frac{\sqrt{D\cdot\tau}}{L}+1\right)}{\left(\exp\left(\frac{L}{\sqrt{D\cdot\tau}}\right)+1\right)} =$$

$$= 1-\frac{\left(2\cdot\frac{\sqrt{D\cdot\tau}}{L}\cdot\exp\left(\frac{L}{\sqrt{D\cdot\tau}}\right)-2\cdot\frac{\sqrt{D\cdot\tau}}{L}\right)}{\left(\exp\left(\frac{L}{\sqrt{D\cdot\tau}}\right)+1\right)}$$

If we introduce $\lambda = \sqrt{D\cdot\tau}$ as the mean exciton excursion range:

$$I(L) = 1-\frac{\left(2\cdot\frac{\lambda}{L}\cdot\exp\left(\frac{L}{\lambda}\right)-2\cdot\frac{\lambda}{L}\right)}{\left(\exp\left(\frac{L}{\lambda}\right)+1\right)} = 1-2\cdot\frac{\lambda}{L}\cdot\frac{\exp\left(\frac{L}{\lambda}\right)-1}{\exp\left(\frac{L}{\lambda}\right)+1} = \boxed{1-2\cdot\frac{\lambda}{L}\cdot\frac{\sinh\left(\frac{L}{2\cdot\lambda}\right)}{\cosh\left(\frac{L}{2\cdot\lambda}\right)}}$$

REFERENCES

1. Brousseau, L. C. Label-Free "Digital Detection" of Single-Molecule DNA Hybridization With a Single Electron Transistor. *J. Am. Chem. Soc.* **2006,** *128*, 11346-11347.

2. Lee, C. J.; Lee, T. J.; Lyu, S. C.; Zhang, Y.; Ruh, H.; Lee, H. J. Field Emission From Well-Aligned Zinc Oxide Nanowires Grown at Low Temperature. *Appl. Phys. Lett.* **2002,** *81*, 3648-3650.

3. Wang, Q. H.; Yan, M.; Chang, R. P. H. Flat Panel Display Prototype Using Gated Carbon Nanotube Field Emitters. *Appl. Phys. Lett.* **2001,** *78*, 1294-1296.

4. Lee, N. S.; Chung, D. S.; Han, I. T.; Kang, J. H.; Choi, Y. S.; Kim, H. Y.; Park, S. H.; Jin, Y. W.; Yi, W. K.; Yun, M. J. et al. Application of Carbon Nanotubes to Field Emission Displays. *Diamond and Related Materials* **2001,** *10*, 265-270.

5. Yang, S. Y.; Ma, C. C. M.; Teng, C. C.; Huang, Y. W.; Liao, S. H.; Huang, Y. L.; Tien, H. W.; Lee, T. M.; Chiou, K. C. Effect of Functionalized Carbon Nanotubes on the Thermal Conductivity of Epoxy Composites. *Carbon* **2010,** *48*, 592-603.

6. Ajayan, P. M.; Schadler, L. S.; Giannaris, C.; Rubio, A. Single-Walled Carbon Nanotube-Polymer Composites: Strength and Weakness. *Adv. Mater.* **2000,** *12*, 750-753.

7. Calvert, P. Nanotube Composites - A Recipe for Strength. *Nature* **1999,** *399*, 210-211.

8. Zhu, J.; Kim, J. D.; Peng, H. Q.; Margrave, J. L.; Khabashesku, V. N.; Barrera, E. V. Improving the Dispersion and Integration of Single-Walled Carbon Nanotubes in Epoxy Composites Through Functionalization. *Nano Lett.* **2003,** *3*, 1107-1113.

9. Zhu, J.; Peng, H. Q.; Rodriguez-Macias, F.; Margrave, J. L.; Khabashesku, V. N.; Imam, A. M.; Lozano, K.; Barrera, E. V. Reinforcing Epoxy Polymer Composites Through Covalent Integration of Functionalized Nanotubes. *Advanced Functional Materials* **2004,** *14*, 643-648.

10. Kroto, H. W.; Heath, J. R.; O'Brien, S. C.; Curl, R. F.; Smalley, R. E. C_{60}: Buckminsterfullerene. *Nature* **1985,** *318*, 162-3.

11. Rao, C. N. R.; Deepak, F. L.; Gundiah, G.; Govindaraj, A. Inorganic Nanowires. *Progress in Solid State Chemistry* **2003,** *31*, 5-147.

12. Wu, Y.; Xiang, J.; Yang, C.; Lu, W.; Lieber, C. M. Single-Crystal Metallic Nanowires and Metal/Semiconductor Nanowire Heterostructures. *Nature* **2004,** *430*, 61-65.

13. Kim, F.; Song, J. H.; Yang, P. D. Photochemical Synthesis of Gold Nanorods. *J. Am. Chem. Soc.* **2002,** *124*, 14316-14317.

14. Averitt, R. D.; Sarkar, D.; Halas, N. J. Plasmon Resonance Shifts of Au-Coated Au2S Nanoshells: Insight into Multicomponent Nanoparticle Growth. *Phys. Rev. Lett.* **1997,** *78*, 4217-4220.

15. Iijima, S. Helical Microtubules of Graphitic Carbon. *Nature* **1991,** *354*, 56-58.

16. Novoselov, K. S.; Geim, A. K.; Morozov, S. V.; Jiang, D.; Zhang, Y.; Dubonos, S. V.; Grigorieva, I. V.; Firsov, A. A. Electric Field Effect in Atomically Thin Carbon Films. *Science* **2004,** *306*, 666-669.

17. Wildoer, J. W. G.; Venema, L. C.; Rinzler, A. G.; Smalley, R. E.; Dekker, C. Electronic Structure of Atomically Resolved Carbon Nanotubes. *Nature* **1998,** *391*, 59-62.

18. Saito, R.; Dresselhaus, G.; Dresselhaus, M. S. *Physical Properties of Carbon Nanotubes;* Imperial College Press: London, 1998.

19. Saito, R.; Fujita, M.; Dresselhaus, G.; Dresselhaus, M. S. Electronic Structure of Chiral Graphene Tubules. *Appl. Phys. Lett.* **1992,** *60*, 2204-2206.

20. Bachilo, S. M.; Strano, M. S.; Kittrell, C.; Hauge, R. H.; Smalley, R. E.; Weisman, R. B. Structure-Assigned Optical Spectra of Single-Walled Carbon Nanotubes. *Science* **2002,** *298*, 2361-2366.

21. Iijima, S.; Ichihashi, T. Single-Shell Carbon Nanotubes of 1-Nm Diameter (Vol 363, Pg 603, 1993). *Nature* **1993,** *364*, 737.

22. Dai, H. J.; Rinzler, A. G.; Nikolaev, P.; Thess, A.; Colbert, D. T.; Smalley, R. E. Single-Wall Nanotubes Produced by Metal-Catalyzed Disproportionation of Carbon Monoxide. *Chem. Phys. Lett.* **1996,** *260*, 471-475.

23. Nikolaev, P.; Bronikowski, M. J.; Bradley, R. K.; Rohmund, F.; Colbert, D. T.; Smith, K. A.; Smalley, R. E. Gas-Phase Catalytic Growth of Single-Walled Carbon Nanotubes From Carbon Monoxide. *Chem. Phys. Lett.* **1999,** *313*, 91-97.

24. Kitiyanan, B.; Alvarez, W. E.; Harwell, J. H.; Resasco, D. E. Controlled Production of Single-Wall Carbon Nanotubes by Catalytic Decomposition of CO on Bimetallic CoMo Catalysts. *Chem. Phys. Lett.* **2000,** *317*, 497-503.

25. Alvarez, W. E.; Pompeo, F.; Herrera, J. E.; Balzano, L.; Resasco, D. E. Characterization of Single-Walled Carbon Nanotubes (SWNTs) Produced by CO Disproportionation on Co-Mo Catalysts. *Chem. Mater.* **2002,** *14*, 1853-1858.

26. Resasco, D. E.; Alvarez, W. E.; Pompeo, F.; Balzano, L.; Herrera, J. E.; Kitiyanan, B.; Borgna, A. A Scalable Process for Production of Single-Walled

Carbon Nanotubes (SWNTs) by Catalytic Disproportionation of CO on a Solid Catalyst. *Journal of Nanoparticle Research* **2002,** *4*, 131-136.

27. Zheng, M.; Jagota, A.; Semke, E. D.; Diner, B. A.; McClean, R. S.; Lustig, S. R.; Richardson, R. E.; Tassi, N. G. DNA-Assisted Dispersion and Separation of Carbon Nanotubes. *Nature Mater.* **2003,** *2*, 338-342.

28. Zheng, M.; Jagota, A.; Strano, M. S.; Santos, A. P.; Barone, P. W.; Chou, S. G.; Diner, B. A.; Dresselhaus, M. S.; McIean, R. S.; Onoa, G. B. et al. Structure-Based Carbon Nanotube Sorting by Sequence-Dependent DNA Assembly. *Science* **2003,** *302*, 1545-1548.

29. Zheng, M.; Semke, E. D. Enrichment of Single Chirality Carbon Nanotubes. *J. Am. Chem. Soc.* **2007,** *129*, 6084-6085.

30. Chen, Z. H.; Du, X.; Du, M. H.; Rancken, C. D.; Cheng, H. P.; Rinzler, A. G. Bulk Separative Enrichment in Metallic or Semiconducting Single-Walled Carbon Nanotubes. *Nano Lett.* **2003,** *3*, 1245-1249.

31. Krupke, R.; Hennrich, F.; Kappes, M. M.; Lohneysen, H. V. Surface Conductance Induced Dielectrophoresis of Semiconducting Single-Walled Carbon Nanotubes. *Nano Lett.* **2004,** *4*, 1395-1399.

32. Hersam, M. C. Progress Towards Monodisperse Single-Walled Carbon Nanotubes. *Nature Nanotech.* **2008,** *3*, 387-394.

33. Arnold, M. S.; Stupp, S. I.; Hersam, M. C. Enrichment of Single-Walled Carbon Nanotubes by Diameter in Density Gradients. *Nano Lett.* **2005,** *5*, 713-718.

34. Arnold, M. S.; Green, A. A.; Hulvat, J. F.; Stupp, S. I.; Hersam, M. C. Sorting Carbon Nanotubes by Electronic Structure Using Density Differentiation. *Nature Nanotech.* **2006,** *1*, 60-65.

35. Green, A. A.; Hersam, M. C. Colored Semitransparent Conductive Coatings Consisting of Monodisperse Metallic Single-Walled Carbon Nanotubes. *Nano Lett.* **2008,** *8*, 1417-1422.

36. Tu, X. M.; Zheng, M. A DNA-Based Approach to the Carbon Nanotube Sorting Problem. *Nano Research* **2008,** *1*, 185-194.

37. Tu, X.; Manohar, A.; Jagota, A.; Zheng, M. DNA Sequence Motifs for Structure-Specific Recognition and Separation of Carbon Nanotubes. *Nature* **2009,** *460*, 250-253.

38. Ziegler, K. J.; Schmidt, D. J.; Rauwald, U.; Shah, K. N.; Flor, E. L.; Hauge, R. H.; Smalley, R. E. Length-Dependent Extraction of Single-Walled Carbon Nanotubes. *Nano Lett.* **2005,** *5*, 2355-2359.

39. Fagan, J. A.; Becker, M. L.; Chun, J.; Hobbie, E. K. Length Fractionation of Carbon Nanotubes Using Centrifugation. *Adv. Mater.* **2008,** *20*, 1609-1613.

40. Arnold, K.; Hennrich, F.; Krupke, R.; Lebedkin, S.; Kappes, M. M. Length Separation Studies of Single Walled Carbon Nanotube Dispersions. *Phys. Status Solidi B* **2006,** *243*, 3073-3076.

41. Asada, Y.; Sugai, T.; Kitaura, R.; Shinohara, H. Chromatographic Length Separation and Photoluminescence Study on DNA-Wrapped Single-Wall and Double-Wall Carbon Nanotubes. *Journal of Nanomaterials* **2009**.

42. Yang, Y. L.; Xie, L. M.; Chen, Z.; Liu, M. H.; Zhu, T.; Liu, Z. F. Purification and Length Separation of Single-Walled Carbon Nanotubes Using Chromatographic Method. *Synth. Met.* **2005,** *155*, 455-460.

43. Heller, D. A.; Mayrhofer, R. M.; Baik, S.; Grinkova, Y. V.; Usrey, M. L.; Strano, M. S. Concomitant Length and Diameter Separation of Single-Walled Carbon Nanotubes. *J. Am. Chem. Soc.* **2004,** *126*, 14567-14573.

44. Doorn, S. K.; Fields, R. E.; Hu, H.; Hamon, M. A.; Haddon, R. C.; Selegue, J. P.; Majidi, V. High Resolution Capillary Electrophoresis of Carbon Nanotubes. *J. Am. Chem. Soc.* **2002,** *124*, 3169-3174.

45. Vetcher, A. A.; Srinivasan, S.; Vetcher, I. A.; Abramov, S. M.; Kozlov, M.; Baughman, R. H.; Levene, S. D. Fractionation of SWNT/Nucleic Acid Complexes by Agarose Gel Electrophoresis. *Nanotechnology* **2006,** *17*, 4263-4269.

46. Collier, C. P. Carbon Nanotube Tips for Scanning Probe Microscopy, In *Carbon Nanotubes*, O'Connell, M. J., Ed.; CRC Press: Boca Raton, 2006; pp 295-313.

47. Chen, Y. C.; Raravikar, N. R.; Schadler, L. S.; Ajayan, P. M.; Zhao, Y. P.; Lu, T. M.; Wang, G. C.; Zhang, X. C. Ultrafast Optical Switching Properties of Single-Wall Carbon Nanotube Polymer Composites at 1.55 Mu m. *Appl. Phys. Lett.* **2002,** *81*, 975-977.

48. Bianco, A.; Kostarelos, K.; Prato, M. Applications of Carbon Nanotubes in Drug Delivery. *Curr. Opin. Chem. Biol.* **2005,** *9*, 674-679.

49. Liu, Z.; Chen, K.; Davis, C.; Sherlock, S.; Cao, Q. Z.; Chen, X. Y.; Dai, H. J. Drug Delivery With Carbon Nanotubes for in Vivo Cancer Treatment. *Cancer Research* **2008,** *68*, 6652-6660.

50. Kam, N. W. S.; O'Connell, M. J.; Wisdom, J. A.; Dai, H. Carbon Nanotubes As Multifunctional Biological Transporters and Near-Infrared Agents for Selective Cancer Cell Destruction. *Proc. Natl. Acad. Sci.* **2005,** *102*, 11600-11605.

51. Gannon, C. J.; Cherukuri, P.; Yakobson, B. I.; Cognet, L.; Kanzius, J. S.; Kittrell,

C.; Weisman, R. B.; Pasquali, M.; Schmidt, H. K.; Smalley, R. E. et al. Carbon Nanotube-Enhanced Thermal Destruction of Cancer Cells in a Noninvasive Radiofrequency Field. *Cancer* **2007,** *110*, 2654-2665.

52. Lim, S. C.; Lee, K.; Lee, I. H.; Lee, Y. H. Field Emission and Application of Carbon Nanotubes. *Nano* **2007,** *2*, 69-89.

53. Yao, Z.; Kane, C. L.; Dekker, C. High-Field Electrical Transport in Single-Wall Carbon Nanotubes. *Phys. Rev. Lett.* **2000,** *84*, 2941-2944.

54. Martel, R.; Schmidt, T.; Shea, H. R.; Hertel, T.; Avouris, P. Single- and Multi-Wall Carbon Nanotube Field-Effect Transistors. *Appl. Phys. Lett.* **1998,** *73*, 2447-2449.

55. Tans, S. J.; Verschueren, A. R. M.; Dekker, C. Room-Temperature Transistor Based on a Single Carbon Nanotube. *Nature* **1998,** *393*, 49-52.

56. Avouris, P.; Radosavljevic, M.; Wind, S. J. Carbon Nanotube Electronics and Optoelectronics, In *Applied Physics of Carbon Nanotubes*, Rotkin, S. V.; Subramoney, S., Eds.; Springer: Berlin, 2005; pp 227-251.

57. Cherukuri, P.; Gannon, C. J.; Leeuw, T. K.; Schmidt, H. K.; Smalley, R. E.; Curley, S. A.; Weisman, R. B. Mammalian Pharmacokinetics of Carbon Nanotubes Using Intrinsic Near-Infrared Fluorescence. *Proc. Natl. Acad. Sci. U. S. A.* **2006,** *103*, 18882-18886.

58. Heller, D. A.; Jeng, E. S.; Yeung, T.-K.; Martinez, B. M.; Moll, A. E.; Gastala, J. B.; Strano, M. S. Optical Detection of DNA Conformational Polymorphism on Single-Walled Carbon Nanotubes. *Science* **2006,** *311*, 508-511.

59. Ziegler, K. J.; Rauwald, U.; Gu, Z. N.; Liang, F.; Billups, W. E.; Hauge, R. H.; Smalley, R. E. Statistically Accurate Length Measurements of Single-Walled Carbon Nanotubes. *J. Nanosci. Nanotechnol.* **2007,** *7*, 2917-2921.

60. Dresselhaus, M. S.; Dresselhaus, G.; Jorio, A.; Souza Filho, A. G.; Saito, R. Raman Spectroscopy on Isolated Single Wall Carbon Nanotubes. *Carbon* **2002,** *40*, 2043-2061.

61. Kataura, H.; Kumazawa, Y.; Maniwa, Y.; Umezu, I.; Suzuki, S.; Ohtsuka, Y.; Achiba, Y. Optical Properties of Single-Wall Carbon Nanotubes. *Synth. Met.* **1999,** *103*, 2555-2558.

62. Chen, Z. H.; Du, X.; Du, M. H.; Rancken, C. D.; Cheng, H. P.; Rinzler, A. G. Bulk Separative Enrichment in Metallic or Semiconducting Single-Walled Carbon Nanotubes. *Nano Lett.* **2003,** *3*, 1245-1249.

63. Itkis, M. E.; Perea, D. E.; Niyogi, S.; Rickard, S. M.; Hamon, M. A.; Zhao, B.; Haddon, R. C. Purity Evaluation of As-Prepared Single-Walled Carbon Nanotube

Soot by Use of Solution-Phase Near-IR Spectroscopy. *Nano Lett.* **2003,** *3*, 309-314.

64. O'Connell, M.; Bachilo, S. M.; Huffman, C. B.; Moore, V.; Strano, M. S.; Haroz, E.; Rialon, K.; Boul, P. J.; Noon, W. H.; Kittrell, C. et al. Band-Gap Fluorescence From Individual Single-Walled Carbon Nanotubes. *Science* **2002,** *297*, 593-596.

65. Wang, F.; Dukovic, G.; Brus, L. E.; Heinz, T. F. The Optical Resonances in Carbon Nanotubes Arise From Excitons. *Science* **2005,** *5723*, 838-841.

66. Ichida, M.; Mizuno, S.; Tani, K.; Saito, Y.; Nakamura, A. Exciton Effects of Optical Transitions in Single-Wall Carbon Nanotubes. *J. Phys. Soc. Jpn.* **1999,** *68*, 3131-3133.

67. Perebeinos, V.; Tersoff, J.; Avouris, P. Effect of Exciton-Phonon Coupling in the Calculated Optical Absorption of Carbon Nanotubes. *Phys. Rev. Lett.* **2005,** *94*.

68. Cognet, L.; Tsyboulski, D.; Rocha, J.-D. R.; Doyle, C. D.; Tour, J. M.; Weisman, R. B. Stepwise Quenching of Exciton Fluorescence in Carbon Nanotubes by Single-Molecule Reactions. *Science* **2007,** *316*, 1465-1468.

69. Siitonen, A. J.; Tsyboulski, D. A.; Bachilo, S. M.; Weisman, R. B. Dependence of Exciton Mobility on Structure in Single-Walled Carbon Nanotubes. *J. Phys. Chem. Lett.* **2010,** *1*, 2189-2192.

70. Hagen, A.; Steiner, M.; Raschke, M. B.; Lienau, C.; Hertel, T.; Qian, H.; Meixner, A. J.; Hartschuh, A. Exponential Decay Lifetimes of Excitons in Individual Single-Walled Carbon Nanotubes. *Phys. Rev. Lett.* **2005,** *95*, 197401-1-197401/4.

71. Berciaud, S.; Cognet, L.; Lounis, B. Luminescence Decay and the Absorption Cross Section of Individual Single-Walled Carbon Nanotubes. *Phys. Rev. Lett.* **2008,** *101*, 077402-1-077402-4.

72. Duque, J. G.; Pasquali, M.; Cognet, L.; Lounis, B. Environmental and Synthesis-Dependent Luminescence Properties of Individual Single-Walled Carbon Nanotubes. *ACS Nano* **2009,** *3*, 2153-2156.

73. Satishkumar, B. C.; Brown, L. O.; Gao, Y.; Wang, C. C.; Wang, H. L.; Doorn, S. K. Reversible Fluorescence Quenching in Carbon Nanotubes for Biomolecular Sensing. *Nature Nanotech.* **2007,** *2*, 560-564.

74. Arnold, M. S.; Sharping, J. E.; Stupp, S. I.; Kumar, P.; Hersam, M. C. Band Gap Photobleaching in Isolated Single-Walled Carbon Nanotubes. *Nano Lett.* **2003,** *3*, 1549-1554.

75. Ma, Y.-Z.; Valkunas, L.; Dexheimer, S. L.; Bachilo, S. M.; Fleming, G. R. Femtosecond Spectroscopy of Optical Excitations in Single-Walled Carbon

Nanotubes: Evidence for Exciton-Exciton Annihilation. *Phys. Rev. Lett.* **2005,** *94*, 157402-1-157402-4.

76. Srivastava, A.; Kono, J. Diffusion-Limited Exciton-Exciton Annihilation in Single-Walled Carbon Nanotubes: A Time-Dependent Analysis. *Phys. Rev. B* **2009,** *79*.

77. Bachilo, S. M.; Balzano, L.; Herrera, J. E.; Pompeo, F.; Resasco, D. E.; Weisman, R. B. Narrow (n,m)-Distribution of Single-Walled Carbon Nanotubes Grown Using a Solid Supported Catalyst. *J. Am. Chem. Soc.* **2003,** *125*, 11186-11187.

78. Lefebvre, J.; Fraser, J. M.; Homma, Y.; Finnie, P. Photoluminescence From Single-Walled Carbon Nanotubes: a Comparison Between Suspended and Micelle-Encapsulated Nanotubes. *Appl. Phys. A* **2004,** *78*, 1107-1110.

79. Naumov, A. V.; Kuznetsov, O. A.; Harutyunyan, A. R.; Green, A. A.; Hersam, M. C.; Resasco, D. E.; Nikolaev, P. N.; Weisman, R. B. Quantifying the Semiconducting Fraction in Single-Walled Carbon Nanotube Samples Through Comparative Atomic Force and Photoluminescence Microscopies. *Nano Lett.* **2009,** *9*, 3203-3208.

80. Strano, M. S.; Huffman, C. B.; Moore, V. C.; O'Connell, M. J.; Haroz, E. H.; Hubbard, J.; Miller, M.; Rialon, K.; Kittrell, C.; Ramesh, S. et al. Reversible, Band-Gap-Selective Protonation of Single-Walled Carbon Nanotubes in Solution. *J. Phys. Chem. B* **2003,** *107*, 6979-6985.

81. Barone, P. W.; Baik, S.; Heller, D. A.; Strano, M. S. Near-Infrared Optical Sensors Based on Single-Walled Carbon Nanotubes. *Nature Mater.* **2005,** *4*, 86-92.

82. Naumov, A. V.; Bachilo, S. M.; Tsyboulski, D. A.; Weisman, R. B. Electric Field Quenching of Carbon Nanotube Photoluminescence. *Nano Lett.* **2008,** *8*, 1527-1531.

83. Dresselhaus, M. S.; Dresselhaus, G.; Avouris, Ph. *Carbon Nanotubes: Synthesis, Structure, Properties, and Applications;* Springer-Verlag: New York, Vol. 80, 2001.

84. Hafner, J. H.; Cheung, C. L.; Oosterkamp, T. H.; Lieber, C. M. High-Yield Assembly of Individual Single-Walled Carbon Nanotube Tips for Scanning Probe Microscopies. *J. Phys. Chem. B* **2001,** *105*, 743-746.

85. Yakobson, B. I.; Campbell, M. P.; Brabec, C. J.; Bernholc, J. High Strain Rate Fracture and C-Chain Unraveling in Carbon Nanotubes. *Computational Materials Science* **1997,** *8*, 341-348.

86. Koswatta, S. O.; Hasan, S.; Lundstrom, M. S.; Anantram, M. P.; Nikonov, D. E. Ballisticity of Nanotube Field-Effect Transistors: Role of Phonon Energy and

Gate Bias. *Appl. Phys. Lett.* **2006,** *89*.

87. Chen, B. H.; Wei, J. H.; Lo, P. Y.; Wang, H. H.; Lai, M. J.; Tsai, M. J.; Chao, T. S.; Lin, H. C.; Huang, T. Y. A Carbon Nanotube Field Effect Transistor With Tunable Conduction-Type by Electrostatic Effects. *Sol. St. Elec.* **2004,** *50*, 1341-1348.

88. Misewich, J. A.; Avouris, Ph.; Martel, R.; Tsang, J. C.; Heinze, S.; Tersoff, J. Electrically Induced Optical Emission From a Carbon Nanotube FET. *Science* **2003,** *300*, 783-786.

89. Freitag, M.; Perebeinos, V.; Chen, J.; Stein, A.; Tsang, J. C.; Misewich, J. A.; Martel, R.; Avouris, P. Hot Carrier Electroluminescence From a Single Carbon Nanotube. *Nano Lett.* **2004,** *4*, 1063-1066.

90. Freitag, M.; Steiner, M.; Naumov, A.; Small, J. P.; Bol, A. A.; Perebeinos, V.; Avouris, P. Carbon Nanotube Photo- and Electroluminescence in Longitudinal Electric Fields. *ACS Nano* **2009,** *3*, 3744-3748.

91. Steiner, M.; Freitag, M.; Perebeinos, V.; Naumov, A.; Small, J. P.; Bol, A. A.; Avouris, P. Gate-Variable Light Absorption and Emission in a Semiconducting Carbon Nanotube. *Nano Lett.* **2009,** *9*, 3477-3481.

92. O'Keeffe, J.; Wei, C. Y.; Cho, K. J. Bandstructure Modulation for Carbon Nanotubes in a Uniform Electric Field. *Appl. Phys. Lett.* **2002,** *80*, 676-678.

93. Pacheco, M.; Barticevic, Z.; Rocha, C. G.; Latge, A. Electric Field Effects on the Energy Spectrum of Carbon Nanotubes. *Journal of Physics-Condensed Matter* **2005,** *17*, 5839-5847.

94. Rocha, C. G.; Pacheco, M.; Barticevic, Z.; Latge, A. Electric and Magnetic Field Effects on Electronic Structure of Straight and Toroidal Carbon Nanotubes. *Brazilian Journal of Physics* **2004,** *34*, 644-646.

95. Novikov, D. S.; Levitov, L. S. Energy Anomaly and Polarizability of Carbon Nanotubes. *Phys. Rev. Lett.* **2006,** *96*.

96. Chen, R. B.; Lee, C. H.; Chang, C. P.; Lue, C. S.; Lin, M. F. Electronic and Optical Properties of Finite Carbon Nanotubes in a Static Electric Field. *Physica E-Low-Dimensional Systems & Nanostructures* **2006,** *34*, 670-673.

97. Perebeinos, V.; Avouris, P. Exciton Ionization, Franz-Keldysh, and Stark Effects in Carbon Nanotubes. *Nano Lett.* **2007,** *7*, 609-613.

98. Tsyboulski, D. A.; Bachilo, S. M.; Weisman, R. B. Versatile Visualization of Individual Single-Walled Carbon Nanotubes With Near-Infrared Fluorescence Microscopy. *Nano Lett.* **2005,** *5*, 975-979.

99. Mohite, A. D.; Gopinath, P.; Shah, H. M.; Alphenaar, B. W. Exciton Dissociation and Stark Effect in the Carbon Nanotube Photocurrent Spectrum. *Nano Lett.* **2008,** *8*, 142-146.

100. Mohite, A.; Lin, J. T.; Sumanasekera, G.; Alphenaar, B. W. Field-Enhanced Photocurrent Spectroscopy of Excitonic States in Single-Wall Carbon Nanotubes. *Nano Lett.* **2006,** *6*, 1369-1373.

101. Weisman, R. B.; Bachilo, S. M. Dependence of Optical Transition Energies on Structure for Single-Walled Carbon Nanotubes in Aqueous Suspension: An Empirical Kataura Plot. *Nano Lett.* **2003,** *3*, 1235-1238.

102. Dukovic, G.; Wang, F.; Song, D. H.; Sfeir, M. Y.; Heinz, T. F.; Brus, L. E. Structural Dependence of Excitonic Optical Transitions and Band-Gap Energies in Carbon Nanotubes. *Nano Lett.* **2005,** *5*, 2314-2318.

103. Pedersen, T. G. Exciton Effects in Carbon Nanotubes. *Carbon* **2004,** *42*, 1007-1010.

104. Wu, Z. C.; Chen, Z. H.; Du, X.; Logan, J. M.; Sippel, J.; Nikolou, M.; Kamaras, K.; Reynolds, J. R.; Tanner, D. B.; Hebard, A. F. et al. Transparent, Conductive Carbon Nanotube Films. *Science* **2004,** *305*, 1273-1276.

105. Yu, X.; Rajamani, R.; Stelson, K. A.; Cui, T. Carbon Nanotube Based Transparent Conductive Thin Films. *J. Nanosci. Nanotechnol.* **2006,** *6*, 1939-1944.

106. Harutyunyan, A. R.; Chen, G. G.; Paronyan, T. M.; Pigos, E. M.; Kuznetsov, O. A.; Hewaparakrama, K.; Kim, S. M.; Zakharov, D.; Stach, E. A.; Sumanasekera, G. U. Preferential Growth of Single-Walled Carbon Nanotubes With Metallic Conductivity. *Science* **2009,** *326*, 116-120.

107. Chen, Z. H.; Du, X.; Du, M. H.; Rancken, C. D.; Cheng, H. P.; Rinzler, A. G. Bulk Separative Enrichment in Metallic or Semiconducting Single-Walled Carbon Nanotubes. *Nano Lett.* **2003,** *3*, 1245-1249.

108. Qin, L.-C.; Iijima, S.; Kataura, H.; Maniwa, Y.; Suzuki, S.; Achiba, Y. Helicity and Packing of Single-Walled Carbon Nanotubes Studied by Electron Nanodiffraction. *Chem. Phys. Lett.* **1997,** *268*, 101-106.

109. Gao, M.; Zuo, J. M.; Twesten, R. D.; Petrov, I. Structure Determination of Individual Single-Wall Carbon Nanotubes by Nanoarea Electron Diffraction. *Appl. Phys. Lett.* **2003,** *82*, 2703-2705.

110. Vijayaraghavan, A.; Blatt, S.; Marquardt, C.; Dehm, S.; Wahi, R.; Hennrich, F.; Krupke, R. Imaging Electronic Structure of Carbon Nanotubes by Voltage-Contrast Scanning Electron Microscopy. *Nano Research* **2009,** *1*, 321-332.

111. Kim, W. J.; Lee, C. Y.; O'Brien, K. P.; Plombon, J. J.; Blackwell, J. M.; Strano, M. S. Connecting Single Molecule Electrical Measurements to Ensemble Spectroscopic Properties for Quantification of Single-Walled Carbon Nanotube Separation. *J. Am. Chem. Soc.* **2009,** *131*, 3128-3129.

112. Li, Y. M.; Mann, D.; Rolandi, M.; Kim, W.; Ural, A.; Hung, S.; Javey, A.; Cao, J.; Wang, D. W.; Yenilmez, E. et al. Preferential Growth of Semiconducting Single-Walled Carbon Nanotubes by a Plasma Enhanced CVD Method. *Nano Lett.* **2004,** *4*, 317-321.

113. Weisman, R. B.; Bachilo, S. M. Dependence of Optical Transition Energies on Structure for Single-Walled Carbon Nanotubes in Aqueous Suspension: an Empirical Kataura Plot. *Nano Lett.* **2003,** *3*, 1235-1238.

114. Jorio, A.; Saito, R.; Hafner, J. H.; Lieber, C. M.; Hunter, M.; McClure, T.; Dresselhaus, G.; Dresselhaus, M. S. Structural (*n,m*) Determination of Isolated Single-Wall Carbon Nanotubes by Resonant Raman Scattering. *Phys. Rev. Lett.* **2001,** *86*, 1118-1121.

115. Rao, A. M.; Richter, E.; Bandow, S.; Chase, B.; Eklund, P. C.; Williams, K. A.; Fang, S.; Subbaswamy, K. R.; Menon, M.; Thess, A. et al. Diameter-Selective Raman Scattering From Vibrational Modes in Carbon Nanotubes. *Science* **1997,** *275*, 187-191.

116. Strano, M. S.; Dyke, C. A.; Usrey, M. L.; Barone, P. W.; Allen, M. J.; Shan, H. W.; Kittrell, C.; Hauge, R. H.; Tour, J. M.; Smalley, R. E. Electronic Structure Control of Single-Walled Carbon Nanotube Functionalization. *Science* **2003,** *301*, 1519-1522.

117. Krupke, R.; Hennrich, F.; von Lohneysen, H.; Kappes, M. M. Separation of Metallic From Semiconducting Single-Walled Carbon Nanotubes. *Science* **2003,** *301*, 344-347.

118. Chen, Z. H.; Du, X.; Du, M. H.; Rancken, C. D.; Cheng, H. P.; Rinzler, A. G. Bulk Separative Enrichment in Metallic or Semiconducting Single-Walled Carbon Nanotubes. *Nano Lett.* **2003,** *3*, 1245-1249.

119. Miyata, Y.; Yanagi, K.; Maniwa, Y.; Kataura, H. Optical Evaluation of the Metal-to-Semiconductor Ratio of Single-Wall Carbon Nanotubes. *J. Phys. Chem. C* **2008,** *112*, 13187-13191.

120. Blackburn, J. L.; Barnes, T. M.; Beard, M. C.; Kim, Y. H.; Tenent, R. C.; McDonald, T. J.; To, B.; Coutts, T. J.; Heben, M. J. Ransparent Conductive Single-Walled Carbon Nanotube Networks With Precisely Tunable Ratios of Semiconducting and Metallic Nanotubes. *ACS Nano* **2008,** *2*, 1266-1274.

121. Moore, V. C.; Strano, M. S.; Haroz, E. H.; Hauge, R. H.; Smalley, R. E. Individually Suspended Single-Walled Carbon Nanotubes in Various Surfactants.

Nano Lett. **2003,** *3*, 1379-1382.

122. Gomez-Gualdron, D. A.; Balbuena, P. B. The Role of Cap Chirality in the Mechanism of Growth of Single-Wall Carbon Nanotubes. *Nanotechnology* **2008,** *19*.

123. Lolli, G.; Zhang, L. A.; Balzano, L.; Sakulchaicharoen, N.; Tan, Y. Q.; Resasco, D. E. Tailoring (n,m) Structure of Single-Walled Carbon Nanotubes by Modifying Reaction Conditions and the Nature of the Support of CoMo Catalysts. *J. Phys. Chem. B* **2006,** *110*, 2108-2115.

124. Krupke, R.; Hennrich, F.; von Lohneysen, H.; Kappes, M. M. Separation of Metallic From Semiconducting Single-Walled Carbon Nanotubes. *Science* **2003,** *301*, 344-347.

125. Arepalli, S.; Holmes, W. A.; Nikolaev, P.; Hadjiev, V. G.; Scott, C. D. A Parametric Study of Single-Wall Carbon Nanotube Growth by Laser Ablation. *J. Nanosci. Nanotechnol.* **2004,** *4*, 762-773.

126. Arepalli, S.; Scott, C. D. *Chem. Phys. Lett.* **1999,** *302*, 193.

127. Arepalli, S.; Nikolaev, P.; Holmes, W. A.; Scott, C. D. *Appl. Phys. A* **2000,** *70*, 125.

128. Arepalli, S. *J. Nanosci. Nanotechnol.* **2004,** *4*, 317.

129. Nikolaev, P.; Holmes, W. A.; Sosa, E.; Boul, P.; Arepalli, S.; Yowell, L. *J. Nanosci. Nanotechnol.* **2009,** *in press*.

130. Kong, J.; Franklin, N. R.; Zhou, C. W.; Chapline, M. G.; Peng, S.; Cho, K. J.; Dai, H. J. Nanotube Molecular Wires As Chemical Sensors. *Science* **2000,** *287*, 622-625.

131. Kong, J.; Chapline, M. G.; Dai, H. J. Functionalized Carbon Nanotubes for Molecular Hydrogen Sensors. *Adv. Mater.* **2001,** *13*, 1384-1386.

132. Bhirde, A. A.; Patel, V.; Gavard, J.; Zhang, G. F.; Sousa, A. A.; Masedunskas, A.; Leapman, R. D.; Weigert, R.; Gutkind, J. S.; Rusling, J. F. Targeted Killing of Cancer Cells in Vivo and in Vitro With EGF-Directed Carbon Nanotube-Based Drug Delivery. *ACS Nano* **2009,** *3*, 307-316.

133. Bartholomeusz, G.; Cherukuri, P.; Kingston, J.; Cognet, L.; Lemos, R.; Leeuw, T. K.; Gumbiner-Russo, L.; Weisman, R. B.; Powis, G. In Vivo Therapeutic Silencing of Hypoxia-Inducible Factor 1 Alpha (HIF-1α) Using Single-Walled Carbon Nanotubes Noncovalently Coated With SiRNA. *Nano Research* **2009,** *2*, 279-291.

134. Pang, L. S. K.; Saxby, J. D.; Chatfield, S. P. Thermogravimetric Analysis of

Carbon Nanotubes and Nanoparticles. *J. Phys. Chem.* **1993,** *97*, 6941-6942.

135. Shi, Z. J.; Lian, Y. F.; Liao, F. H.; Zhou, X. H.; Gu, Z. N.; Zhang, Y. G.; Iijima, S. Purification of Single-Wall Carbon Nanotubes. *Solid State Communications* **1999,** *112*, 35-37.

136. Landi, B. J.; Cress, C. D.; Evans, C. M.; Raffaelle, R. P. Thermal Oxidation Profiling of Single-Walled Carbon Nanotubes. *Chem. Mater.* **2005,** *17*, 6819-6834.

137. Weisman, R. B. Fluorimetric Characterization of Single-Walled Carbon Nanotubes. *Analytical and Bioanalytical Chemistry* **2010,** *396*, 1015-1023.

138. Itkis, M. E.; Perea, D. E.; Niyogi, S.; Rickard, S. M.; Hamon, M. A.; Zhao, B.; Haddon, R. C. Purity Evaluation of As-Prepared Single-Walled Carbon Nanotube Soot by Use of Solution-Phase Near-IR Spectroscopy. *Nano Lett.* **2003,** *3*, 309-314.

139. Landi, B. J.; Ruf, H. J.; Evans, C. M.; Cress, C. D.; Raffaelle, R. P. Purity Assessment of Single-Wall Carbon Nanotubes, Using Optical Absorption Spectroscopy. *J. Phys. Chem. B* **2005,** *109*, 9952-9965.

140. Yongqiang, T.; Resasco, D. E. Dispersion of Single-Walled Carbon Nanotubes of Narrow Diameter Distribution. *J. Phys. Chem. B* **2005,** *109*, 14454-14460.

141. Strano, M. S.; Doorn, S. K.; Haroz, E.; Kittrell, C.; Hauge, R. H.; Smalley, R. E. Assignment of (n,m) Raman and Optical Features of Metallic Single-Walled Carbon Nanotubes. *Nano Lett.* **2003,** *3*, 1091-1096.

142. Murakami, Y.; Einarsson, E.; Edamura, T.; Maruyama, S. Polarization Dependence of the Optical Absorption of Single-Walled Carbon Nanotubes. *Phys. Rev. Lett.* **2005,** *94*, 087402-1-087402/4.

143. Tan, Y.; Resasco, D. E. Dispersion of Single-Walled Carbon Nanotubes of Narrow Diameter Distribution. *J. Phys. Chem. B* **2005,** *109*, 14454-14460.

144. Luo, Z.; Pfefferle, L. D.; Haller, G. L.; Papadimitrakopoulos, F. (n,m) Abundance Evaluation of Single-Walled Carbon Nanotubes by Fluorescence and Absorption Spectroscopy. *J. Am. Chem. Soc.* **2006,** *128*, 15511-15516.

145. Nair, N.; Usrey, M. L.; Kim, W.; Braatz, R. D.; Strano, M. S. Estimation of the (n,m) Concentration Distribution of Single-Walled Carbon Nanotubes From Photoabsorption Spectra. *Anal. Chem.* **2006,** *78*, 7689-7696.

146. Lu, W.; Xiong, Y.; Hassanien, A.; Zhao, W.; Zheng, M.; Chen, L. A Scanning Probe Microscopy Based Assay for Single-Walled Carbon Nanotube Metallicity. *Nano Lett.* **2009,** *9*, 1668-1672.

147. Naumov, A. V.; Kuznetsov, O. A.; Harutyunyan, A. R.; Green, A. A.; Hersam, M. C.; Resasco, D. E.; Nikolaev, P. N.; Weisman, R. B. Quantifying the Semiconducting Fraction in Single-Walled Carbon Nanotube Samples Through Comparative Atomic Force and Photoluminescence Microscopies. *Nano Lett.* **2009,** *9*, 3203-3208.

148. Blackburn, J. L.; Barnes, T. M.; Beard, M. C.; Kim, Y. H.; Tenent, R. C.; McDonald, T. J.; To, B.; Coutts, T. J.; Heben, M. J. Transparent Conductive Single-Walled Carbon Nanotube Networks With Precisely Tunable Ratios of Semiconducting and Metallic Nanotubes. *ACS Nano* **2008,** *2*, 1266-1274.

149. Ghosh, S.; Bachilo, S. M.; Weisman, R. B. Advanced Sorting of Single-Walled Carbon Nanotubes by Nonlinear Density-Gradient Ultracentrifugation. *Nature Nanotech.* **2010,** *5*, 443-450.

150. Arnold, M. S.; Green, A. A.; Hulvat, J. F.; Stupp, S. I.; Hersam, M. C. Sorting Carbon Nanotubes by Electronic Structure Using Density Differentiation. *Nature Nanotech.* **2006,** *1*, 60-65.

151. Arnold, M. S.; Green, A. A.; Hulvat, J. F.; Stupp, S. I.; Hersam, M. C. Sorting Carbon Nanotubes by Electronic Structure Using Density Differentiation. *Nature Nanotech.* **2006,** *1*, 60-65.

152. Banerjee, S.; Wong, S. S. Rational Sidewall Functionalization and Purification of Single-Walled Carbon Nanotubes by Solution-Phase Ozonolysis. *J. Phys. Chem. B* **2002,** *106*, 12144-12151.

153. Dyke, C. A.; Tour, J. M. Solvent-Free Functionalization of Carbon Nanotubes. *J. Am. Chem. Soc.* **2003,** *125*, 1156-1157.

154. Itkis, M. E.; Perea, D. E.; Niyogi, S.; Rickard, S. M.; Hamon, M. A.; Zhao, B.; Haddon, R. C. Purity Evaluation of As-Prepared Single-Walled Carbon Nanotube Soot by Use of Solution-Phase Near-IR Spectroscopy. *Nano Lett.* **2003,** *3*, 309-314.

155. Day, K. L.; Huffman, D. R. Measured Extinction Efficiency of Graphite Smoke in Region 1200 - 6000 A. *Nature Phys. Sci.* **1973,** *243*, 50-51.

156. Huang, X.; Mclean, R. S.; Zheng, M. High-Resolution Length Sorting and Purification of DNA-Wrapped Carbon Nanotubes by Size-Exclusion Chromatography. *Anal. Chem.* **2005,** *77*, 6225-6228.

157. Landi, B. J.; Ruf, H. J.; Evans, C. M.; Cress, C. D.; Raffaelle, R. P. Purity Assessment of Single-Wall Carbon Nanotubes, Using Optical Absorption Spectroscopy. *J. Phys. Chem. B* **2005,** *109*, 9952-9965.

158. Heller, D. A.; Barone, P. W.; Strano, M. S. Sonication-Induced Changes in Chiral Distribution: A Complication in the Use of Single-Walled Carbon Nanotube

Fluorescence for Determining Species Distribution. *Carbon* **2005,** *43*, 651-653.

159. Hennrich, F.; Krupke, R.; Arnold, K.; Stutz, J. A. R.; Lebedkin, S.; Koch, T.; Schimmel, T.; Kappes, M. M. The Mechanism of Cavitation-Induced Scission of Single-Walled Carbon Nanotubes. *J. Phys. Chem. B* **2007,** *111*, 1932-1937.

160. Nish, A.; Hwang, J. Y.; Doig, J.; Nicholas, R. J. Highly Selective Dispersion of Singlewalled Carbon Nanotubes Using Aromatic Polymers. *Nature Nanotech.* **2007,** *2*, 640-646.

161. Pichler, Th.; Knupfer, M.; Golden, M. S.; Fink, J.; Rinzler, A.; Smalley, R. E. Localized and Delocalized Electronic States in Single-Wall Carbon Nanotubes. *Phys. Rev. Lett.* **1998,** *80*, 4729-4732.

162. Ando, T. Theory of Electronic States and Transport in Carbon Nanotubes. *J. Phys. Soc. Jpn.* **2005,** *74*, 777-817.

163. Damnjanovic, M.; Milosevic, I.; Vukovic, T.; Sredanovic, R. Full Symmetry, Optical Activity, and Potentials of Single-Wall and Multiwall Nanotubes. *Phys. Rev. B* **1999,** *60*, 2728-2739.

164. Arnold, M. S.; Stupp, S. I.; Hersam, M. C. Enrichment of Single-Walled Carbon Nanotubes by Diameter in Density Gradients. *Nano Lett.* **2005,** *5*, 713-718.

165. Arnold, M. S.; Green, A. A.; Hulvat, J. F.; Stupp, S. I.; Hersam, M. C. Sorting Carbon Nanotubes by Electronic Structure Using Density Differentiation. *Nature Nanotech.* **2006,** *1*, 60-65.

166. Yanagi, K.; Miyata, Y.; Kataura, H. Optical and Conductive Characteristics of Metallic Single-Wall Carbon Nanotubes With Three Basic Colors; Cyan, Magenta, and Yellow. *Applied Physics Express* **2008,** *1*.

167. Dalton, A. B.; Collins, S.; Munoz, E.; Razal, J. M.; Ebron, V. H.; Ferraris, J. P.; Coleman, J. N.; Kim, B. G.; Baughman, R. H. Super-Tough Carbon-Nanotube Fibres - These Extraordinary Composite Fibres Can Be Woven into Electronic Textiles. *Nature* **2003,** *423*, 703.

168. Zhu, H. W.; Xu, C. L.; Wu, D. H.; Wei, B. Q.; Vajtai, R.; Ajayan, P. M. Direct Synthesis of Long Single-Walled Carbon Nanotube Strands. *Science* **2002,** *296*, 884-886.

169. Li, Y. L.; Kinloch, I. A.; Windle, A. H. Direct Spinning of Carbon Nanotube Fibers From Chemical Vapor Deposition Synthesis. *Science* **2004,** *304*, 276-278.

170. Zhou, W.; Vavro, J.; Guthy, C.; Winey, K. I.; Fischer, J. E.; Ericson, L. M.; Ramesh, S.; Saini, R.; Davis, V. A.; Kittrell, C. et al. Single Wall Carbon Nanotube Fibers Extruded From Super-Acid Suspensions: Preferred Orientation, Electrical, and Thermal Transport. *Journal of Applied Physics* **2004,** *95*, 649-655.

171. Gong, X. Y.; Liu, J.; Baskaran, S.; Voise, R. D.; Young, J. S. Surfactant-Assisted Processing of Carbon Nanotube/Polymer Composites. *Chem. Mater.* **2000,** *12*, 1049-1052.

172. Thostenson, E. T.; Ren, Z.; Chou, T.-W. Advances in the Science and Technology of Carbon Nanotubes and Their Composites: a Review. *Compos. Sci. Technol.* **2001,** *61*, 1899-1912.

173. Kong, J.; Yenilmez, E.; Tombler, T. W.; Kim, W.; Dai, H. J.; Laughlin, R. B.; Liu, L.; Jayanthi, C. S.; Wu, S. Y. Quantum Interference and Ballistic Transmission in Nanotube Electron Waveguides. *Phys. Rev. Lett.* **2001,** *87*, art-106801.

174. Mann, D.; Javey, A.; Kong, J.; Wang, Q.; Dai, H. J. Ballistic Transport in Metallic Nanotubes With Reliable Pd Ohmic Contacts. *Nano Lett.* **2003,** *3*, 1541-1544.

175. White, C. T.; Todorov, T. N. Carbon Nanotubes As Long Ballistic Conductors. *Nature* **1998,** *393*, 240-242.

176. Freitag, M.; Martin, Y.; Misewich, J. A.; Martel, R.; Avouris, Ph. Photoconductivity of Single Carbon Nanotubes. *Nano Lett.* **2003,** *3*, 1067-1071.

177. Chen, J.; Perebeinos, V.; Freitag, M.; Tsang, J.; Fu, Q.; Liu, J.; Avouris, P. Applied Physics: Bright Infrared Emission From Electrically Induced Excitons in Carbon Nanotubes. *Science* **2005,** *310*, 1171-1174.

178. Javey, A.; Guo, J.; Wang, Q.; Lundstrom, M.; Dai, H. J. Ballistic Carbon Nanotube Field-Effect Transistors. *Nature* **2003,** *424*, 654-657.

179. Dai, H. J.; Javey, A.; Pop, E.; Mann, D.; Kim, W.; Lu, Y. R. Electrical Transport Properties and Field Effect Transistors of Carbon Nanotubes. *Nano* **2006,** *1*, 1-13.

180. Fagan, J. A.; Simpson, J. R.; Bauer, B. J.; DePaoliLacerda, S. H.; Becker, M. L.; Chun, J.; Migler, K. B.; Hight Walker, A. R.; Hobbie, E. K. Length-Dependent Optical Effects in Single-Wall Carbon Nanotubes. *J. Am. Chem. Soc.* **2007,** *129*, 10607-10612.

181. Tsyboulski, D. A.; Bachilo, S. M.; Kolomeisky, A. B.; Weisman, R. B. Translational and Rotational Dynamics of Individual Single-Walled Carbon Nanotubes in Aqueous Suspension. *ACS Nano* **2008,** *2*, 1770-1776.

182. Arnold, M. S.; Green, A. A.; Hulvat, J. F.; Stupp, S. I.; Hersam, M. C. Sorting Carbon Nanotubes by Electronic Structure Using Density Differentiation. *Nature Nanotech.* **2006,** *1*, 60-65.

183. Fagan, J. A.; Simpson, J. R.; Bauer, B. J.; DePaoliLacerda, S. H.; Becker, M. L.; Chun, J.; Migler, K. B.; Hight Walker, A. R.; Hobbie, E. K. Length-Dependent

Optical Effects in Single-Wall Carbon Nanotubes. *J. Am. Chem. Soc.* **2007,** *129*, 10607-10612.

184. Panagiotou, T.; Bernard, J.; Mesite V. *Deagglomeration and Dispersion of Carbon Nanotubes Using Microfluidizer® High Shear Fluid Processors* ; 2008; pp. 39-42.

185. Arnold, M. S.; Green, A. A.; Hulvat, J. F.; Stupp, S. I.; Hersam, M. C. Sorting Carbon Nanotubes by Electronic Structure Using Density Differentiation. *Nature Nanotech.* **2006,** *1*, 60-65.

186. Siitonen, A. J.; Tsyboulski, D. A.; Bachilo, S. M.; Weisman, R. B. Surfactant-Dependent Exciton Mobility in Single-Walled Carbon Nanotubes Studied by Single-Molecule Reactions. *Nano Lett.* **2010,** *10*, 1595-1599.

187. Odom, T. W.; Huang, J.-L.; Kim, P.; Lieber, C. M. Structure and Electronic Properties of Carbon Nanotubes. *J. Phys. Chem. B* **2000,** *104*, 2794-2809.

188. Sutter, P. EPITAXIAL GRAPHENE How Silicon Leaves the Scene. *Nature Mater.* **2009,** *8*, 171-172.

189. Li, X. S.; Cai, W. W.; An, J. H.; Kim, S.; Nah, J.; Yang, D. X.; Piner, R.; Velamakanni, A.; Jung, I.; Tutuc, E. et al. Large-Area Synthesis of High-Quality and Uniform Graphene Films on Copper Foils. *Science* **2009,** *324*, 1312-1314.

190. Stankovich, S.; Dikin, D. A.; Piner, R. D.; Kohlhaas, K. A.; Kleinhammes, A.; Jia, Y.; Wu, Y.; Nguyen, S. T.; Ruoff, R. S. Synthesis of Graphene-Based Nanosheets Via Chemical Reduction of Exfoliated Graphite Oxide. *Carbon* **2007,** *45*, 1558-1565.

191. Choucair, M.; Thordarson, P.; Stride, J. A. Gram-Scale Production of Graphene Based on Solvothermal Synthesis and Sonication. *Nature Nanotech.* **2009,** *4*, 30-33.

192. Sun, Z. Z.; Yan, Z.; Yao, J.; Beitler, E.; Zhu, Y.; Tour, J. M. Growth of Graphene From Solid Carbon Sources. *Nature* **2010,** *468*, 549-552.

193. Novoselov, K. S.; Jiang, D.; Schedin, F.; Booth, T. J.; Khotkevich, V. V.; Morozov, S. V.; Geim, A. K. Two-Dimensional Atomic Crystals. *Proceedings of the National Academy of Sciences of the United States of America* **2005,** *102*, 10451-10453.

194. Ferrari, A. C.; Meyer, J. C.; Scardaci, V.; Casiraghi, C.; Lazzeri, M.; Mauri, F.; Piscanec, S.; Jiang, D.; Novoselov, K. S.; Roth, S. et al. Raman Spectrum of Graphene and Graphene Layers. *Phys. Rev. Lett.* **2006,** *97*.

195. Geim, A. K.; Novoselov, K. S. The Rise of Graphene. *Nat. Mater.* **2007,** *6*, 183-191.

196. Du, X.; Skachko, I.; Barker, A.; Andrei, E. Y. Approaching Ballistic Transport in Suspended Graphene. *Nature Nanotech.* **2008,** *3*, 491-495.

197. Wu, J. B.; Agrawal, M.; Becerril, H. A.; Bao, Z. N.; Liu, Z. F.; Chen, Y. S.; Peumans, P. Organic Light-Emitting Diodes on Solution-Processed Graphene Transparent Electrodes. *ACS Nano* **2010,** *4*, 43-48.

198. Matyba, P.; Yamaguchi, H.; Eda, G.; Chhowalla, M.; Edman, L.; Robinson, N. D. Graphene and Mobile Ions: The Key to All-Plastic, Solution-Processed Light-Emitting Devices. *ACS Nano* **2010,** *4*, 637-642.

199. Wang, Y.; Chen, X. H.; Zhong, Y. L.; Zhu, F. R.; Loh, K. P. Large Area, Continuous, Few-Layered Graphene As Anodes in Organic Photovoltaic Devices. *Appl. Phys. Lett.* **2009,** *95*.

200. Lin, Y. M.; Jenkins, K. A.; Valdes-Garcia, A.; Small, J. P.; Farmer, D. B.; Avouris, P. Operation of Graphene Transistors at Gigahertz Frequencies. *Nano Lett.* **2009,** *9*, 422-426.

201. Lin, Y. M.; Dimitrakopoulos, C.; Jenkins, K. A.; Farmer, D. B.; Chiu, H. Y.; Grill, A.; Avouris, P. 100-GHz Transistors From Wafer-Scale Epitaxial Graphene. *Science* **2010,** *327*, 662.

202. Shen, T.; Gu, J. J.; Xu, M.; Wu, Y. Q.; Bolen, M. L.; Capano, M. A.; Engel, L. W.; Ye, P. D. Observation of Quantum-Hall Effect in Gated Epitaxial Graphene Grown on SiC (0001). *Appl. Phys. Lett.* **2009,** *95*.

203. Kim, S.; Nah, J.; Jo, I.; Shahrjerdi, D.; Colombo, L.; Yao, Z.; Tutuc, E.; Banerjee, S. K. Realization of a High Mobility Dual-Gated Graphene Field-Effect Transistor With Al2O3 Dielectric. *Appl. Phys. Lett.* **2009,** *94*.

204. Mohanty, N.; Berry, V. Graphene-Based Single-Bacterium Resolution Biodevice and DNA Transistor: Interfacing Graphene Derivatives With Nanoscale and Microscale Biocomponents. *Nano Lett.* **2008,** *8*, 4469-4476.

205. Eigler, S. A New Parameter Based on Graphene for Characterizing Transparent, Conductive Materials. *Carbon* **2009,** *47*, 2936-2939.

206. Sun, Z. P.; Hasan, T.; Torrisi, F.; Popa, D.; Privitera, G.; Wang, F. Q.; Bonaccorso, F.; Basko, D. M.; Ferrari, A. C. Graphene Mode-Locked Ultrafast Laser. *ACS Nano* **2010,** *4*, 803-810.

207. Chen, Z. H.; Lin, Y. M.; Rooks, M. J.; Avouris, P. Graphene Nano-Ribbon Electronics. *Physica E-Low-Dimensional Systems & Nanostructures* **2007,** *40*, 228-232.

208. Han, M. Y.; Ozyilmaz, B.; Zhang, Y. B.; Kim, P. Energy Band-Gap Engineering of Graphene Nanoribbons. *Phys. Rev. Lett.* **2007,** *98*.

209. Li, X. L.; Wang, X. R.; Zhang, L.; Lee, S. W.; Dai, H. J. Chemically Derived, Ultrasmooth Graphene Nanoribbon Semiconductors. *Science* **2008,** *319*, 1229-1232.

210. Kosynkin, D. V.; Higginbotham, A. L.; Sinitskii, A.; Lomeda, J. R.; Dimiev, A.; Price, B. K.; Tour, J. M. Longitudinal Unzipping of Carbon Nanotubes to Form Graphene Nanoribbons. *Nature* **2009,** *458*, 872-8U5.

211. Schnez, S.; Molitor, F.; Stampfer, C.; Guttinger, J.; Shorubalko, I.; Ihn, T.; Ensslin, K. Observation of Excited States in a Graphene Quantum Dot. *Appl. Phys. Lett.* **2009,** *94*.

212. Mueller, M. L.; Yan, X.; McGuire, J. A.; Li, L. S. Triplet States and Electronic Relaxation in Photoexcited Graphene Quantum Dots. *Nano Lett.* **2010,** *10*, 2679-2682.

213. Robinson, J. T.; Burgess, J. S.; Junkermeier, C. E.; Badescu, S. C.; Reinecke, T. L.; Perkins, F. K.; Zalalutdniov, M. K.; Baldwin, J. W.; Culbertson, J. C.; Sheehan, P. E. et al. Properties of Fluorinated Graphene Films. *Nano Lett.* **2010,** *10*, 3001-3005.

214. Luo, Z. T.; Vora, P. M.; Mele, E. J.; Johnson, A. T. C.; Kikkawa, J. M. Photoluminescence and Band Gap Modulation in Graphene Oxide. *Appl. Phys. Lett.* **2009,** *94*.

215. B.C.Brodie On the Atomic Weight of Graphite. *Proceedings of the Royal Society of London* **1859,** *10*, 249.

216. Dreyer, D. R.; Park, S.; Bielawski, C. W.; Ruoff, R. S. The Chemistry of Graphene Oxide. *Chem. Soc. Rev.* **2010,** *39*, 228-240.

217. Eda, G.; Chhowalla, M. Chemically Derived Graphene Oxide: Towards Large-Area Thin-Film Electronics and Optoelectronics. *Adv. Mater.* **2010,** *22*, 2392-2415.

218. Sun, X. M.; Liu, Z.; Welsher, K.; Robinson, J. T.; Goodwin, A.; Zaric, S.; Dai, H. J. Nano-Graphene Oxide for Cellular Imaging and Drug Delivery. *Nano Research* **2008,** *1*, 203-212.

219. Eda, G.; Lin, Y. Y.; Mattevi, C.; Yamaguchi, H.; Chen, H. A.; Chen, I. S.; Chen, C. W.; Chhowalla, M. Blue Photoluminescence From Chemically Derived Graphene Oxide. *Adv. Mater.* **2010,** *22*, 505.

220. Mathioudakis, C.; Kopidakis, G.; Kelires, P. C.; Patsalas, P.; Gioti, M.; Logothetidis, S. Electronic and Optical Properties of a-C From Tight-Binding Molecular Dynamics Simulations. *Thin Solid Films* **2005,** *482*, 151-155.

221. Chen, C. W.; Robertson, J. Nature of Disorder and Localization in Amorphous

Carbon. *Journal of Non-Crystalline Solids* **1998,** *227*, 602-606.

222. Robertson, J.; Oreilly, E. P. Electronic and Atomic-Structure of Amorphous-Carbon. *Phys. Rev. B* **1987,** *35*, 2946-2957.

223. Gokus, T.; Nair, R. R.; Bonetti, A.; Bohmler, M.; Lombardo, A.; Novoselov, K. S.; Geim, A. K.; Ferrari, A. C.; Hartschuh, A. Making Graphene Luminescent by Oxygen Plasma Treatment. *ACS Nano* **2009,** *3*, 3963-3968.

224. Hummers, W. S.; Offeman, R. E. Preparation of Graphitic Oxide. *J. Am. Chem. Soc.* **1958,** *80*, 1339.

225. Kovtyukhova, N. I.; Ollivier, P. J.; Martin, B. R.; Mallouk, T. E.; Chizhik, S. A.; Buzaneva, E. V.; Gorchinskiy, A. D. Layer-by-Layer Assembly of Ultrathin Composite Films From Micron-Sized Graphite Oxide Sheets and Polycations. *Chem. Mater.* **1999,** *11*, 771-778.

226. Fan, X. B.; Peng, W. C.; Li, Y.; Li, X. Y.; Wang, S. L.; Zhang, G. L.; Zhang, F. B. Deoxygenation of Exfoliated Graphite Oxide Under Alkaline Conditions: A Green Route to Graphene Preparation. *Adv. Mater.* **2008,** *20*, 4490-4493.

227. Werner, T. C.; Hercules, D. M. Fluorescence of 9-Anthroic Acid and Its Esters . Environmental Effects on Excited-State Behavior. *J. Phys. Chem.* **1969,** *73*, 2005-&.

228. Milosavljevic, B. H.; Thomas, J. K. Solvent Effects on the Photophysical Properties of Pyrene-3-Carboxylic Acid. *J. Phys. Chem.* **1988,** *92*, 2997-3001.

229. Harris, D. C.; Bertolucci, M. D. *Symmetry and Spectroscopy: An Introduction to Vibrational and Electronic Spectroscopy;* Dover Publications, Inc.: New York, 1989. pp. v-550.

230. Tammer, M. G. Sokrates: Infrared and Raman Characteristic Group Frequencies: Tables and Charts. *Colloid & Polymer Science* **2004,** *283*, 235.

231. Nucci, N. V.; Zelent, B.; Vanderkooi, J. M. Pyrene-1-Carboxylate in Water and Glycerol Solutions: Origin of the Change of PK Upon Excitation. *Journal of Fluorescence* **2008,** *18*, 41-49.

232. Vanderdo, E.; Porter, G. Acidity Constants of Aromatic Carboxylic Acids in S1 State. *Transactions of the Faraday Society* **1968,** *64*, 3215-&.

233. Vanderdo, E.; Dramaix, R.; Nasielsk, J.; Vogels, C. Photochemistry of Aromatic Compounds .1. Acid-Base Properties of Singlet and Triplet Excited States of Pyrene Derivatives and Aza-Aromatic Compounds. *Transactions of the Faraday Society* **1969,** *65*, 3258-&.

234. Zelent, B.; Vanderkooi, J. M.; Coleman, R. G.; Gryczynski, I.; Gryczynski, Z.

Protonation of Excited State Pyrene-1-Carboxylate by Phosphate and Organic Acids in Aqueous Solution Studied by Fluorescence Spectroscopy. *Biophys. J.* **2006,** *91*, 3864-3871.

235. Stryer, L. Excited-State Proton-Transfer Reactions . A Deuterium Isotope Effect on Fluorescence. *J. Am. Chem. Soc.* **1966,** *88*, 5708-&.

236. Marciniak, B.; Kozubek, H.; Paszyc, S. Estimation of PKa* in the First Excited Singlet State. A Physical Chemistry Experiment That Explores Acid-Base Properties in the Excited State. *Journal of Chemical Education* **1992,** *69*, 247-null.

237. Rieger, R.; Mullen, K. Forever Young: Polycyclic Aromatic Hydrocarbons As Model Cases for Structural and Optical Studies. *Journal of Physical Organic Chemistry* **2010,** *23*, 315-325.